Terahertz Surface Plasmon Resonance Sensor for Material Sensing

by

Sondos Alqarni

A thesis
presented to the University of Waterloo
in fulfillment of the
thesis requirement for the degree of
Master of Applied Science
in
Electrical and Computer Engineering - Nanotechnology

Waterloo, Ontario, Canada, 2014

Author's Declaration

I hereby declare that I am the sole author of this thesis. This is a true copy of the thesis, including any required final revisions, as accepted by my examiners.

I understand that my thesis may be made electronically available to the public.

Abstract

Terahertz wave (THz) is comprised of electromagnetic waves carrying frequencies from 0.1 to 30 THz. Terahertz radiation has the ability to interact with a wide range of materials, such as plastic and paper, and to provide low-energy probing of the system's electronic nature, including inter/intra-molecular motions and Debye relaxation - these are not accessible by other wavelengths. Further appealing feature for THz ray is the nonionizing nature and the distinctive optical response of various materials are important for analyzing diverse applications such as material quality control, pharmaceutical, industrial production lines, and biological. Upon that THz waves have been utilized for imaging and spectroscopy, especially Terahertz Time-Domain Spectroscopy (THz-TDS) associated to its ability in measuring the change in the electric field with high sensitivity in time-domain.

Surface plasmon-polaritons (SPPs) at metal-dielectric interfaces have been proven for several decades as a reliable technique for surface analysis and investigation of thin films due to the two dimensional nature of SPPs and the strong electromagnetic field at the interface. Extraordinary transmission of light through subwavelength hole arrays has attracted many areas of applications including optical data storage, near field microscopy, optical displays, and thin film sensing. The enhancement in the tunneled transmission light stemming from the coupling with SPP by the surface configurations has been explored through the waveguide theory and the grating theory of the frequency-selective characteristic of SPP resonances.

At THz frequencies, the extraordinary transmission through thin metallic hole arrays has been demonstrated through the excitation of SPP on the metal–dielectric interface confining the incident THz pulse around the holes, hence precluding THz pulse from easily passing and attenuating into the conductor. Implementing THz SPP in thin film sensing has great potential for industrial applications because the two dimensional nature of SPPs and the strong electromagnetic field at the interface

with the THz natural reaction with the material provides reliable measurements of thin film spectroscopy including optical and dielectric constants, film thickness, and inhomogeneities at interfaces with high precision. This motivates the investigation of the characteristics such as purity of thin organic film including PMMA and those used in organic light emitting diode (OLED) through THz SPR devices.

Two SPR devices contain **either** 2D periodic circular or square hole array in 500 nm Al on an 5 mm-thick intrinsic silicon, **or** a single subwavelength aperture surrounded by concentric periodic grooves of a set period in a metal plate (which is known as a Bull's eye structure), and was fabricated by following the micro-fabrications process encompassed from UV photolithography and wet and dry etching to transfer the pattern into the Al film. The SPR device consisting of 2D periodic circular or square hole array with and without thin Poly(methyl methacrylate) (PMMA) film on it is placed at the focus of the THz beam in transmission THz-TDS, where the spectrum is obtained from the Fourier-transformed sample and reference THz pulses. The transmission is obtained from the ratio between the sample spectrum and reference spectrum, whereas the phase change is the phase difference between the two spectra. To avoid overlap with water absorption lines, the optimal SPR device design has a period of 320 μm and square holes of 150 μm side length. We successfully confirmed the theoretical SPR frequencies for metal-silicon mode and demonstrate a shift to 0.9211 THz due to 2 μm of PMMA layer on the surface.

Acknowledgements

 I would first and foremost like to express my gratitude to my supervisor, Professor Bo Cui. Without his advice, guidance, patient, and support, I would not have achieved what I have achieved in my master studies at university of waterloo. What I learnt from him is far beyond research.

I collaborated with Daniel Hailu to accomplish the work addressed in this thesis, so I would like to express my deep gratitude to him for all the help I received from him. He was cooperative with sharing his ideas and clarifying some of terahertz plasmon concepts since I am new to this field.

In addition, I would like to thank Richard Barber, Nina Heinig, Dr. Ting Tsui, Celal Con, Jian Zhang, Ripon Kumar, and Jhengyuan Chen, who helped me to start my master work through training me in G2N lab, training me using SEM, and being there for me whenever I needed help.

I would like to offer my special thanks to my family, especially my parents for always believing in me, for their continuous love and their supports in my decisions.

Finally my deepest gratitude is to my husband Ahmed, who I am lucky to be married to. Without his encouragement and support, I would not be able to complete my master degree.

To My Husband

Table of Contents

List of Figures

List of Tables

CHAPTER 1

INTRODUCTION

Terahertz (THz) radiation, also known as submillimeter radiation, T-ray, or far infrared (FIR) radiation, is situated between the microwave and the infrared regions in the electromagnetic spectrum [1, 2]. Sources of THz radiation surround us, including cosmic background radiation as well as blackbody radiation from room temperature objects [1, 2]. The frequencies in this region cover between 100 GHz to 10 THz with wavelengths "in vacuum" from 3mm to 30 um [see Figure 1] [1-5]. The THz region has been referred to as the THz gap [see Figure 1] of which little research has been exploited owing to the lack of powerful sources that emit a coherent THz wave, detectors to collect the THz signal, and necessary hardware [2, 26].   THz band has been dividing the microwave and the infrared regions into solid-state electronics and optical photonics for a long period of time [1, 4].
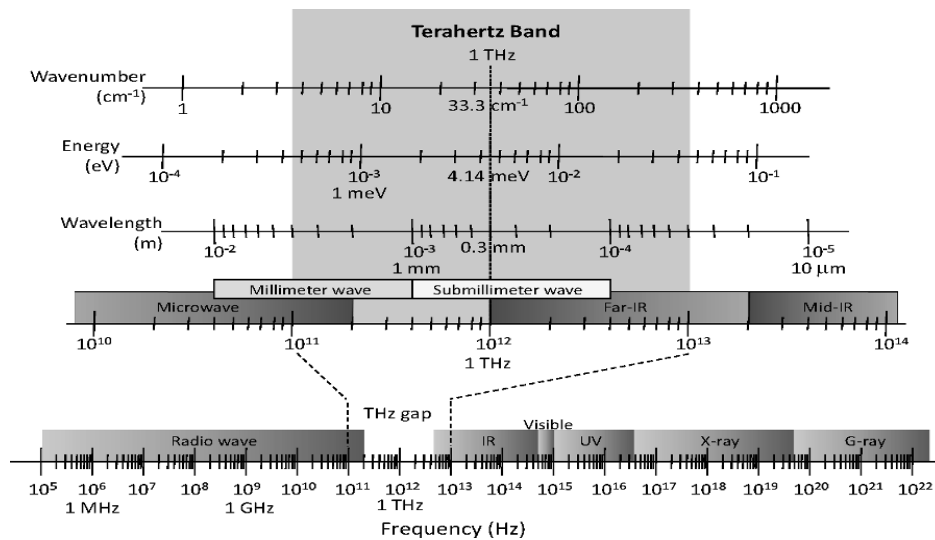
Figure 1.1. Illustration of the THz region and the THz gap [1].

1
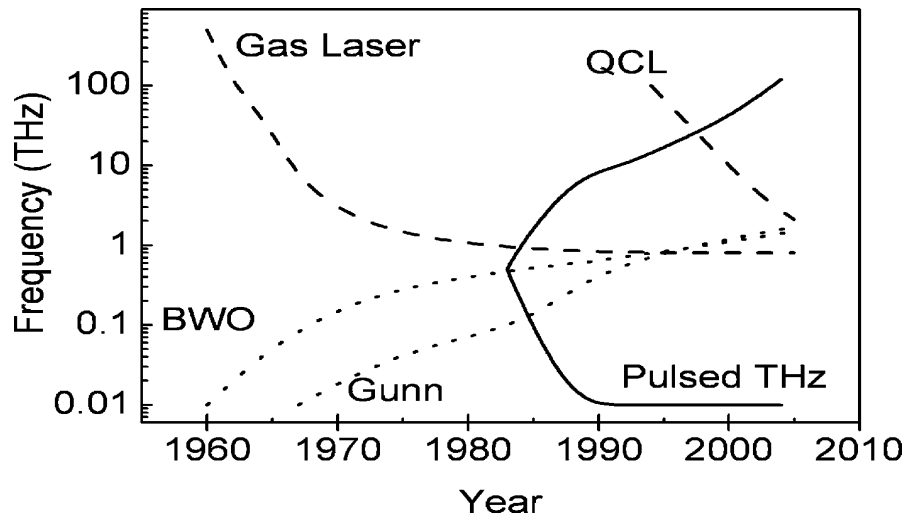
Figure 1.2. The use techniques to bridge the THz gap [2].

However, due to the unique characteristics of THz radiation, the THz gap has evolved into an intensive research area [1, 2, 3, 4]. Figure 2 shows the techniques used to bridge this THz gap. The development of the laser in the 1960s initiated the investigation in THz band since the high power laser sources provide coherent THz waves [4, 6]. In 1964, Gebbie et al. completed the first report on THz; however, the first successful emission and sensing of THz waves occurred in 1980 [1, 4, 6]. Finding suitable sources and detectors for THz waves and having the ability to control and manipulate THz waves were the aims of early research [1, 2]. Electronic devices in the microwave region cannot provide output with frequencies above GHz [26]. Radiation carried THz frequencies could not be obtained from interband diode lasers, used to generate infrared rays, due to the lack of semiconducters with short-lifetime carriers [26].Therefore, approximations applied to optical photonic waves and electromagnetic waves including principles, tools, as well as the mechanisms of generation and detection, which cannot be used to explore the THz band [see Table 1] [2, 4]. Although THz waves can be described by Maxwell's equations, new principles, materials, and tools are needed that include pure principles of microwaves, or pure principles of infrared by introducing new materials and tools [2]. Alternatively, combining techniques from the state-of-art of both microwaves and infrared are being demonstrated such as through photomixing [2]. At present, numerous sources

2

generate T-rays either in short-pulse mode or continuous wave (CW) mode with output power ranging from nanowatt to 10 W [25].

	Electromagnetics	Optics
Name of waves	Electromagnetic waves	Optical waves
Principle	Maxwell equations	Schrodinger equations
Emission	Classical movement	Quantum transition
Measurement	Electric field	Intensity
Tools	Circuit, antenna, waveguide	Lens, mirror, fiber
Approximation	Uniform field	Uniform medium

Table 1.1. The use of approximations in the infrared region and the microwave region [1].

THz radiation has unique and desirable features [see Figure 3 and 4], which have attracted the researchers to explore the THz region [1-4, 8, 9]. (1) Many optically opaque materials, which have low-interaction energy and carry a high dielectric constant and a low-quality factor, can be directly detected by T-rays [2, 3, 4, 27]. Such a capability can enable the detection and distinguishing of plastic explosives in cloth, case, and plastic, or provide images of objects below or between such materials [2, 3, 4, 27]. (2) Materials have distinct signatures to the far-infrared region due to their unique molecular vibrations and rotational energy levels between weakly bound molecular entities with hydrogen bonds and weak interaction (van der Waals forces); these signatures allow T-rays to directly characterize or sense their chemical compositions [see Figure 3] [2, 3, 4, 9, 28]. For example, a label free method for genetic analysis can be employed by using THz waves due to the ability of THz waves to detect the binding state of DNA and RNA [2, 3, 9, 21, 28]. (3) Low photon energy allows imaging, characterizing, or sensing of the sample of interest without causing damage, unlike the case in X-ray [2, 9]. This permits the characterized sample to be used in industry, for instance, to provide quality control of food products, or in

medicine to maintain quality [2, 3, 9]. (4) In contrast to microwaves, the deep penetration ability due to the long THz waves, which reduces the effect of Mie scattering, helps in understanding many of the physical and chemical concepts including lattice vibrations in solids, change in crystal polymorphs, movement of large portions of molecules as well as transformation in the solid phase of a material [2, 3, 9, 23, 28]. In addition, this feature is used in imaging the inner structure of many dielectric materials such as wood, paper, and cloth with high resolution due to the long THz wavelength [2, 3, 9]. (5) Chemical and physical systems undergoing change display spectral signatures in the THz regime; thus, THz waves can quantify, image, as well as provide information about the type of the materials used in the sample [2, 9, 24]. In contrast, microwave and X-ray imaging provide only a density image [2, 3, 9, 24].
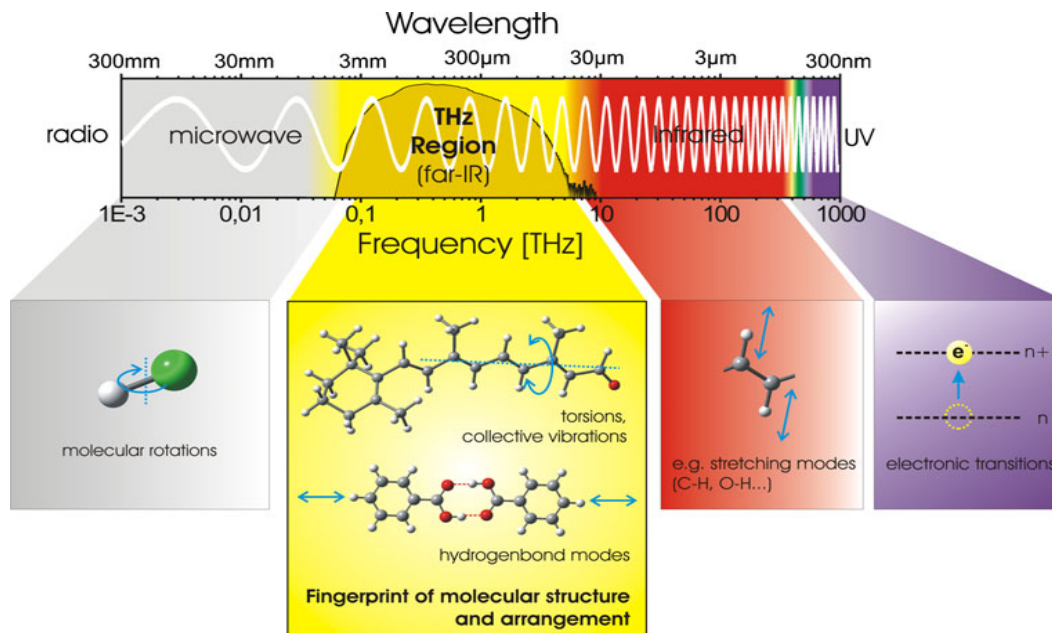
Figure 1.3. The unique fingerprint for many materials from 0.1 to 5 THz as shown in the dark-yellow region [3].

Development of the coherent terahertz time domain spectroscopy (THz-TDS) fosters the science of THz [1, 2, 4, 11]. As shown in Figure 3, THz-TDS has been successfully utilized in sensing, characterizing, and imaging materials in various fields including explosives, medicines, and bio-molecules, since many of the rotational and vibrational peaks of molecules are located between 0.3 and 5 THz [1-15]. THz-TDS will be explored in detail in Chapter 2.

Sensing thin film or a little amount of material by electromagnetic wave in general as well as in the THz regime in the EM spectrum in particular imposes great difficulties for researchers in this area due to short interaction time, resulting in an unmeasurable change in the THz spectrum measured through free-sampling THz-TDS [20-23]. However, the current ability of sensing or characterizing such a sample, which is essential for a large number of applications such as biological, toxic, and chemical weapons, is still far from being satisfactory owing to limitations of the technologies [20-23]. Providing new and efficient sensing models is the predominant motivation of this thesis's work.
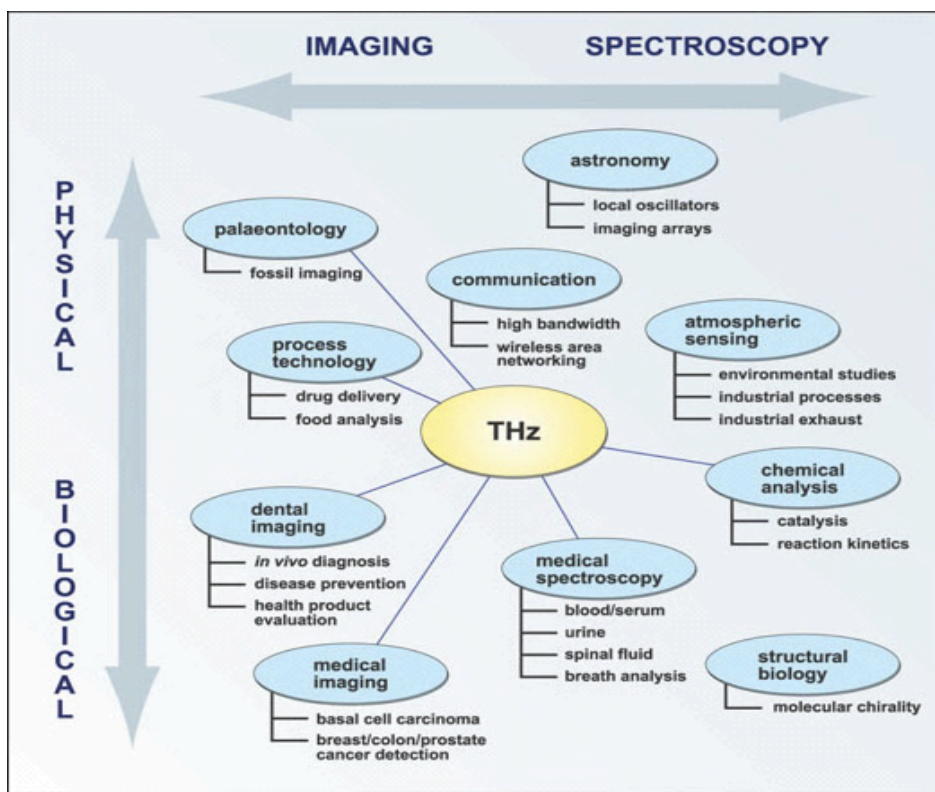
Figure 1.4, A map of applications in THz band [4].

In conclusion, the work of this thesis focuses in sensing and characterizing a sample with a sub-wavelength thickness by conventional free-sampling THz-TDS for quality control issues in organic light emitting diodes (OLED) production. We achieved that by using the extraordinary transmission of THz waves through sub-

wavelength holes in metal resulting in THz-SPPs, which increase the signal-to-noise ratio [6-19].

CHAPTER 2

TERAHERTZ TIME-DOMAIN SPECTROSCOPY

2.1. Introduction:

We present in this chapter an overview of THz sources and detectors. Characterization of the thin film PMMA is achieved by conventional free-space terahertz time-domain spectroscopy (THz-TDS). Therefore, THz-TDS will be discussed in detail.

2.2. Overview of THz Sources and Detectors:

Early research aimed to find sources and detectors for THz waves and develop the ability to control and manipulate THz waves [1,2]. Many different THz sources and detectors have been developed and utilized to obtain coherent and efficient THz signals [4,5]. In 1989, the dipolar antenna structure in THz-TDS was introduced, causing a surge of growth in the THz field [19,20]. Many sample applications began including characterizing material in which the intrinsic complex optical properties of a sample [19,20] could be measured without carrying out a Kramers-Kronig analysis [32]. Numerous sources and receivers generate and detect T-rays, respectively, either in short-pulse mode (broadband) or continuous wave (CW) mode with output power ranging from nanowatt to 10 W [4,25] [see Figures 1 and 2].

2.2.1 Overview of THz Sources:

The development path in THz sources is derived from optical technology, and electronic technology [53]. Optical technology provides THz sources that cover the entire THz frequencies including DFG, BWO, and QCL, as well as optically induced sources. Whereas T-rays with low frequency < 1 THz emits from electronic THz

sources [53]; to date, a linear accelerator was introduced to generate THz pulses (4-25 THz) with ultra-short pulse in order of 1ps carrying high power [54].

Various techniques have been developed to emit CW-THz radiation including photomixing, difference frequency generation (DFG), quantum cascade lasers (QCL), free-electron lasers, far-infrared gas lasers, P-type germanium lasers, frequency multiplication of microwaves, as well as backward wave oscillators (BWO) [4, 5, 18, 22, 31, 39, 58]. Applications depend on the power of those sources [18, 58]. For example, BWO is an electron vacuum tube from which the interaction between electrons and electromagnetic waves generate CW-THz radiation [4]. The highest power CW-THz radiation in order of mW (with frequencies ranging from 0.03 to 1.45 THz) is obtained from the BWO spectroscopic, which is used to determine the dielectric characteristics of materials [20]. Despite the high power THz signal provided from the BWO, the use of BWO spectroscopic is uncommon since it is expensive, operates at high vacuum, needs a high magnetic field, and has a big size [4, 22, 31]. QCL is based on introducing inter-subband or inter-miniband transitions in layered semiconductor heterostructures such as GaAs to generate T-rays [22, 33, 58]. QCL offers high power CW-THz signal up to 100mW, but still has many limitations [4, 22].
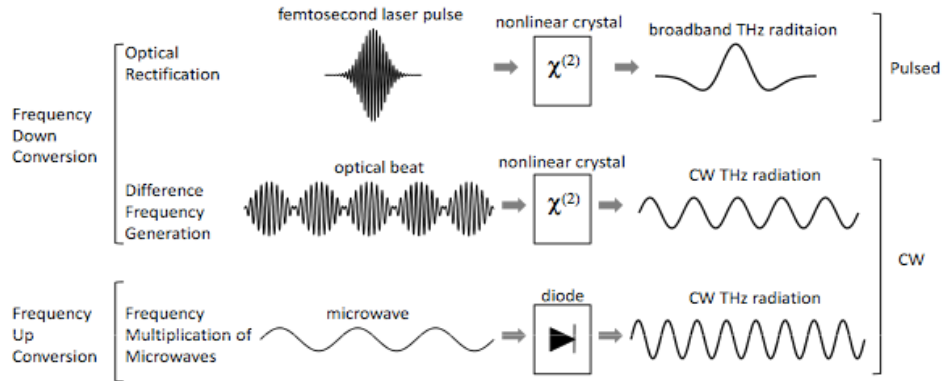
Figure 2.1. Nonlinear medium sources (optical rectification, difference frequency generation, and frequency multiplication of microwaves) generated T-ray [1].

For instance, the long wavelength of the THz-signal implies difficulty in confining the laser mode in a small volume [4]. In addition, a low operation temperature of 180K in vacuum is essential to obtain CW-THz [4]. In 2008, Jonathan et al. demonstrated an increase in output power by coating thin strips of highly doped GaAs along the ridge

waveguide edges; however, this caused a reduction in the operation temperature to 168K [21]. Despite the compact high power output, which can be achieved with many of the CW-THz sources, the generation of CW-THz radiation remains difficult due to the reasons explained above, as well as other issues [22].
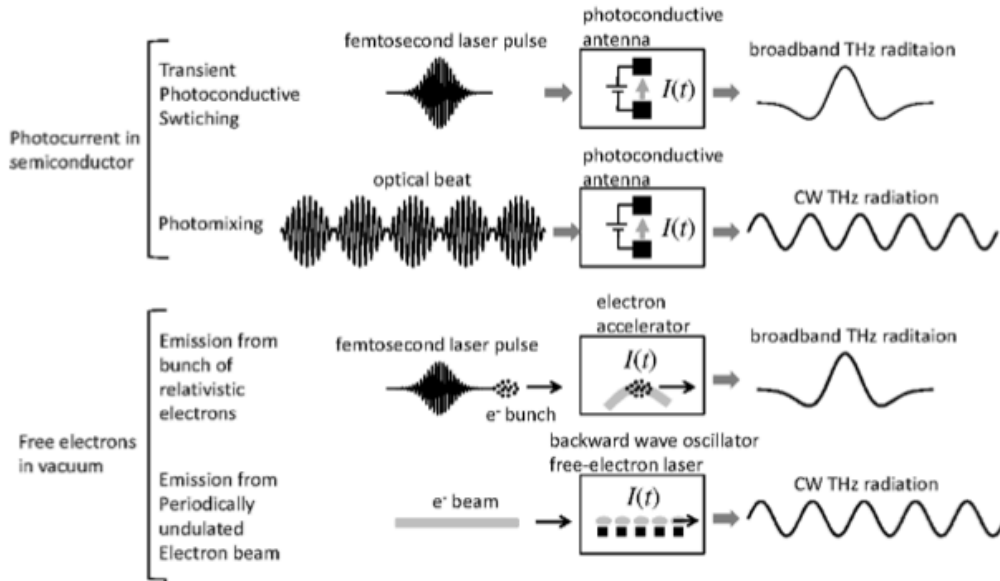
Figure 2.2. THz radiation emitted from accelerating transient currents in photoconductive antenna, backward wave oscillator electron accelerator, and free-electron laser [1].

The photomixing technique is widely used to generate CW-THz radiation, since it is not bulky and does not require the use of an expensive femtosecond laser [18, 23, 29]. Two laser diodes with close frequencies are used in the photomixing method to illuminate a photoconductive antenna, which emits CW-THz radiation [4, 22]. The use of large area emitters (LAE) leads to an increase in the illumination area resulting in THz radiation with mW power while avoiding the thermal-failure limit [22, 24, 25]. Use of the p-i-n photodiode instead of the PC antenna substrate provides carriers with high mobility as well as outputs with wavelengths of 1.55um in the optical communication wavelength [24, 26]. More recently, THz photo-mixers based on double -graphene structures and the excitation of plasma resonances are predicted to provide a sharp plasma peak in the THz band with power higher than the output power, which can be achieved by the p-i-n photodiode due to the superior characterizations of the graphene [26, 29].

Broadband THz radiation is a very short THz pulse [22, 24, 30]. Techniques utilized to generate THz pulses include femtosecond lasers with optical pulses to irradiate PC antennas, semiconductor surfaces, or quantum structures [22, 24, 30]. The average THz power from optically pumped short-pulse THz sources is very low in order of tens of nW and tens of μW, compared with the power of radiation from optical sources, which uses femtosecond lasers to generate radiation [1]. The THz emission move this paragraph to Section 2.2.1 as it is about THz source? mechanism is based on creating an electrical dipole from electron oscillations in the THz source when irradiated with femtosecond pulses, thus leading to the emission of THz waves [1, 2, 4, 30]. These optically induced sources are the main technique to emit broadband THz radiation, yet THz sources such as DFG, BWO, and QCL are utilized to provide THz pulses with high power for some applications, including medical imaging as well as high-data-rate communications [53, 30].

2.2.2. Overview of THz Detectors:

Heat detectors including bolometers, Golay cells, and pyroelectric devices are used to detect CW-THz radiation [4, 50]. Although thermal receivers are sensitive to a broad spectral range, they have many disadvantages including ambient effect and slow response; these disadvantages complicate the detection of THz [4]. Due to design, bolometers provide better performance than Golay cells and pyroelectric devices [4]. In addition, CW-THz radiation can be detected by heterodyne receivers [4]. The detection mechanism is based on a beating signal with the reference signal carrying a certain frequency in a nonlinear device [4]. Heterodyne receivers are more favorable due to their ability to measure the incident radiation with high resolution [4].

Two major mechanisms are used to detect THz pulses: photoconductive detection and electro-optic sampling [2, 4]. They are both gated, with an optical pulse used to turn the receiver on or off, and coherent, which means the ability in measuring the THz amplitude and the phase [50]. The photoconductive antenna was the first detection method, discovered to detect coherent THz radiation [50, 55].

In free-space THz-TDS system, photoconduction antenna (PC) and electro-optical rectification (EOR) are utilized to generate ultra-short THz pulses as well as PC

antenna and electro-optic sampling to detect those pulses [1-4, 31]. THz-TDS will be discussed in detail in this chapter. The measurement on the SPR and Bull's Eyes device are conducted by using THz-TDS in the Waterloo lab.

2.3.Terahertz Time-Domain Spectroscopy (THz-TDS):

The concept of time-domain spectroscopy goes back to the solid-state electronics which is used to determine the properties of a circuit or device [44]. THz-TDS is a spectroscopic technique in which an ultra-short pulse of THz radiation is used to probe the material under investigation by offering information about the materials' properties [2, 3, 4, 36]. Although these measurements are made in time-domain, THz-TDS does not give time-resolved dynamical characterization unless thick samples are used for the characterization with more than one picosecond [12, 61]. The amplitude and phase spectra of THz pulses are measured in time-domain [Figure 5] [2-4]. This contains data about the absorption coefficient and the reflective index of materials in a broad bandwidth [2, 3, 36, 41] with no need to carry out a Kramers-Kronig analysis [32]. Either the transmitted pulse, such as many solid-state systems, or the reflected pulse, including probing water or alcohol, can be measured depending on the use of the sample and its characteristics [2, 3, 38].
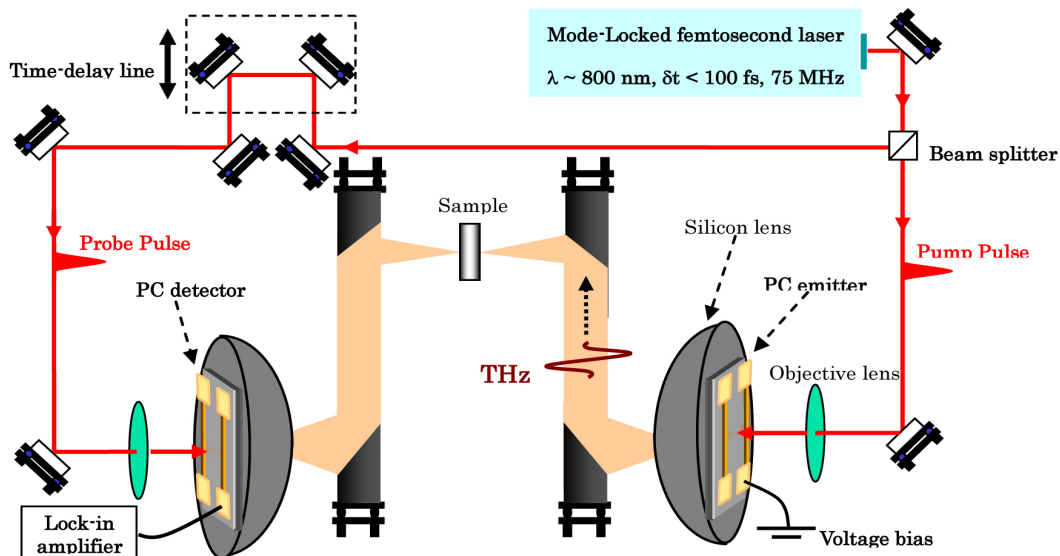
Figure 2.3. Experimental setup for THz-TDS, PC antenna for THz generation and detection [5].

Figures 3 and 4 provide an overview of the experimental setup of the transmission mode of the conventional free-space THz-TDS system [2, 3, 28, 38]. An ultrafast femtosecond laser system generates a short pulse with frequency in the infrared regime [1-6, 28, 38]. The ultrashort pulse is split by a beam splitter into two parts - the probe beam and the pump beam - which arrive at a detector in synchronism[1-6, 28, 30, 38]. Most of the pulse intensity goes to the pump beam by traveling in an optical delay line that makes it possible to record the variation in time on the shape of the THz pulse [1-6, 28, 30, 38, 41]. The probe beam illuminates either a photoconductive antenna forming transient currents or optical rectification, thus beating two optical frequency (NIR or IR) laser beams, to generate THz pulse [see Figures 3 and 4] [1-6, 28, 38, 41]. An unbiased photoconductive detector antenna or an electro-optic sampling regarding the used generation source of the THz pulse detects the THz pulse in the THz-TDS system [1-6, 28, 30, 38]. The parameters of the output THz radiation are affected by the nonlinear medium, pulse duration and pulse energy for the pump laser [31].
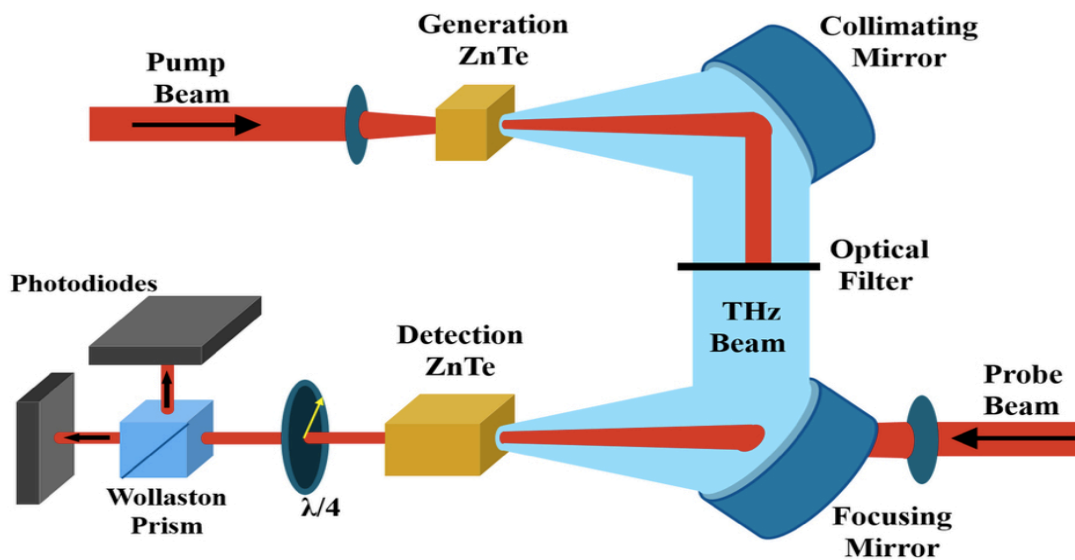
Figure 2.4. Experimental setup for THz-TDS, nonlinear medium and electro-optic sampling for THz generation and detection [6].

The development of coherent THz time-domain spectroscopy fosters the THz science for a variety of applications, such as security, biology and medicine, medical imaging, material spectroscopy and sensing, and monitoring and spectroscopy in

the pharmaceutical industry [1-4, 52]. This broad application is due to its outstanding properties enabling access to the THz region of electromagnetic spectrum between 100 GHz and 10 THz [1, 3, 4, 36, 52]:

1- THz-TDS has an ultra-wide bandwidth that enables the characterization of the electronic, vibrational, and compositional properties of solids, liquids, and gases as well as flames and flows [1].

2- THz-TDS has the ability to provide information about the frequency response (frequency domain) by applying Fourier transformation [1, 40-44]. This ability is due to the use of a coherent detector [1, 40, 44]. That cannot be achieved in the optical detectors because of the use of an incoherent detector [44].

3- A high signal-to-noise ratio can be achieved due to the use of the same materials in THz generator and detector [36]. Such a feature reduces the time consumption so that time required to obtain measurements is equal to the number of the measured values multiplied by the time between two travelling pulses [41]. In other words, fast scan for imaging and spectroscopy applications is obtained by using THz-TDS [36].
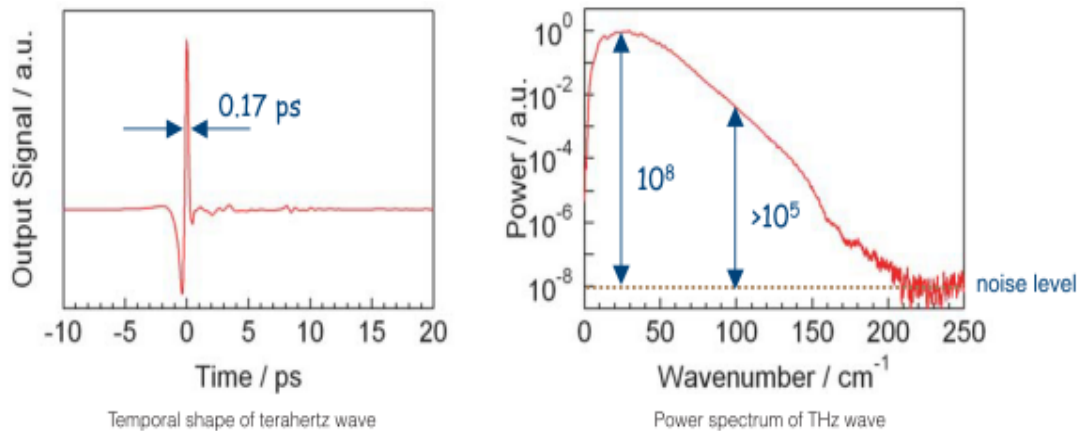
Figure 2.5. (Left) THz signal, (Right) the corresponding Fourier-transformation with an 8 order of magnitude signal-to-noise ratio [5].

The main drawback of THz-TDS is the use of expensive Ti: sapphire femtosecond lasers, but this issue is not relevant if fiber lasers [8, 9, 31, 46] or diode lasers [23] are used in THz-TDS. For example, Pacebutas et al. successfully demonstrated that the Yb:KGW fiber oscillators laser with low-temperature growth $GaBi_{0.08}As_{0.92}$ results in

THz-TDS system's characteristics to be comparable with the best large-aperture GaAs THz emitters excited by Ti:sapphire laser pulses [8].

The signal-to-noise ratio in THz-TDS is poor when sensing samples with very small volumes [61]. Other methods using THz-TDS with waveguides including porous fibers, parallel-plate waveguides, and metal wires are utilized to achieve a high THz field that increases the signal-to-noise ratio [1, 41, 61]. This along with other techniques which are based on improving basic signal loss mechanisms such as Fresnel losses, and water vapor absorption are still not sufficient enough when sensing a sample with a sub-wavelength thickness [61]. Chapter 3 presents a literature review on the limitations imposed through sensing a thin film, and discusses details of how we successfully improved the signal-to-noise ratio.

Convectional free-space THz-TDS will be explored in detail in this section starting with generation of the ultra-short NIR pulses from the femtosecond laser; generation of the THz pulses either by the PC antenna or by the optical rectification; and detection either by the PC antenna or by the electro-optic sampling techniques in the THz-TDS.

2.3.1. Femtosecond Laser:
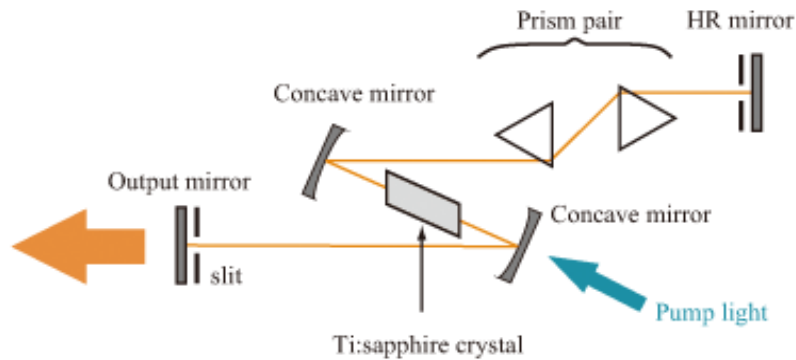
Figure 2.6. The Kerr lens mode-locking [7].

A femtosecond laser is a laser emitting pulses with a femtosecond duration used to drive THz emitters carrying a frequency in the optical region [39]. Many types of femtosecond lasers have been used in the THz-TDS system, including bulk laser,

fiber laser, dye laser, and free electron laser since femtosecond lasers provide electromagnetic waves oscillating in a femtosecond range that, in general, is the essential condition to generate radiation in THz band [4, 42].

The first work that generated and detected THz radiation took place in 1988 by using a colliding-pulse passively mode-locked (CPM) ring dye laser emitting a 120fs optical pulse with PC antenna on RD-SOS [27]. Electrical pulses carrying frequencies from 100 GHz to 2 THz were demonstrated when illuminating the antenna by the dye femtosecond laser [27]. Following the development of a Ti: sapphire laser, dye lasers, which had been used in generating the ultrashort pulse due to the small pulse duration of approximately 10 fs, are not anymore utilized in generating THz radiation because of the difficulties in handling femtosecond dye lasers [2, 4].

Currently, most THz-TDS systems are based on mode-locked Ti: sapphire lasers emitting at wavelength 800 nm due to their outstanding features including the short carrier lifetime in order of 3.2 ms, high thermal conductivity allowing high optical pumping power, as well as the broad gain spectrum ranging from 650 to 1100nm [4, 8, 18, 41]. The titanium-sapphire laser (Ti: sapphire) is a Ti- doped aluminum oxide pumped by a coherent wave laser (such as a Nd:YAG or Nd:YVO4 laser) with a wavelength of approximately 520nm resulting in an emission near 800 nm [18, 31, 41]. Figure 6 shows the Kerr lens mode-locking to generate ultrashort pulse with a wavelength of 800nm [4, 56, 57]. The Kerr lens mode-locking provides THz pulses with 10nJ energy, 10 to 100 fs duration, as well as a repetition rate in order of 8- MHz [4]. Using ultrashort amplifiers to produce pulses near the initial pulse's duration can increase the intensity of THz peak, which is needed in some applications [18].

Fiber lasers, such as YP-fiber laser and Er-fiber laser, have promising features due to the high efficiency, low cost, ability to provide a compact and portable THz system, and power stability [4, 9]. The main limitation in using fiber lasers to drive the EOR for THz generation is the poor phase matching due to the use wavelengths of the fiber lasers [1]. Research has been carried out to enhance the phase-match condition for the use wavelengths [1]. Improvement in velocity mismatching was reported by using a GaP as an EOR source and a Yb-doped fiber laser: the GaP crystal enhanced the output power of THz signals [9, 45]. More recently, laser YP-fiber

laser or Yb:KGW laser has been used to activate photoconductive antenna fabricated from low-temperature-grown GaBiAs epitaxial layers [6, 9]. The GaBiAs PC antenna generates THz pulses with power as high as the power of current THz sources without suffering from the TO limitations when using the EOR technique [9].

2.3.2. Photoconductive Antenna and THz Generation:
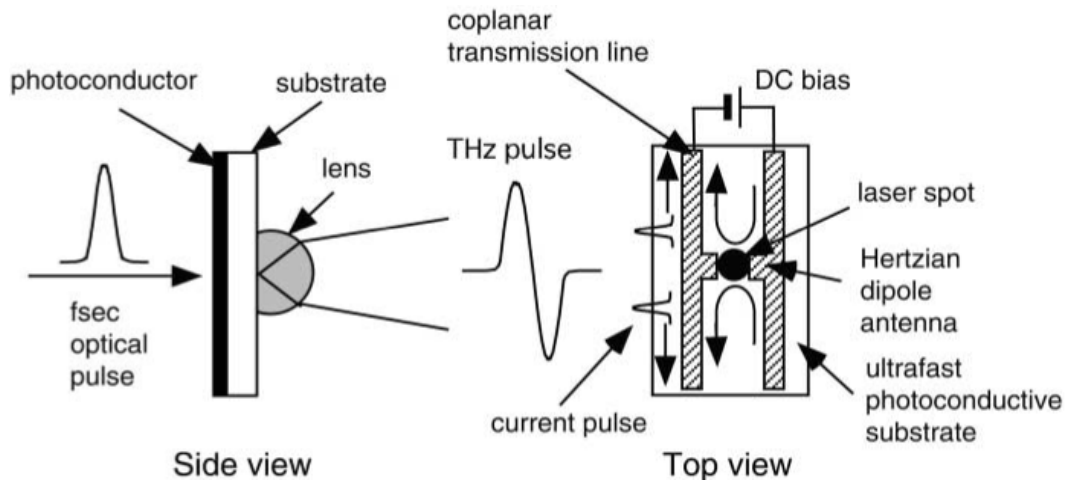
Figure 2.7.(Left) the side view of the PC antenna THz generator, (Right) the top view of the PC antenna THz receiver. The top view is shown since in the PC antenna detector the probe pulse and the THz pulse must be focused in the black spot between two electrodes [8].

The Photoconductive Antenna (PC) is a Hertzain dipole comprised of closely spaced metallic electrodes, and micron-sized dipoles to generate or detect T-ray which are deposited on a semiconducting substrate [4, 19, 57]. In general, an electrical conductivity is observed when the PC antenna is irradiated with EM waves that carry energy exceeding the band gap of the PC antenna in order to switch the material from a semiconductor or an insulator material to a conductor material[18].

In the case of THz generation and detection, the switching (also known as Auston Switch) from insulation to conductivity in the PC antenna has to occur within subpicosecond [2, 4, 27, 31, 57]. This switching action depends on the ultrashort pulse duration emitted from the laser [27, 19]. Also, the intrinsic speed of the carriers - electrons and holes of the PC material - should be very short in the range of subpicosecond [4, 27, 59]. Low-temperature grown gallium arsenide (LT-GaAs), radiation-damaged silicon-on-sapphire (RD-SOS), chromium-doped gallium

arsenide (Cr-GaAs), indium phosphide (InP), and amorphous silicon are examples of the materials used for the semiconductor substrate of the antenna to generate or detect THz pulse [4]. However, the LT-GaAs and the RD-SOS are currently utilized since their carriers' lifetimes are in the range of subpicosecond: 0.2 ps and 0.6 ps respectively [1-4]. The carriers' lifetimes in both the RD–SOS and the LT-GaAs can be optimized by the increase of the ion implantation in the RD–SOS fabrication, in which increases the O+ defects, and by the increase of the thermal annealing after the low temperature growth by the molecular beam epitaxial to the GaAs [4]. These sources emit THz pulses with a wide bandwidth from 0.1GHz to 4THz and an average power in order of 10 nW to several microwatt [31]. However, high power THz radiation in order of 100 μW have been reported by using a large aperture PC antenna [2, 50, 51].

Figure 7 shows the generating mechanism. Electron-hole pairs generated from irradiating the PC antenna by the ultrashort pulse move under the influence of the applied field [2, 3, 19, 50, 59]. The orientation of this biased electric field is in the opposite direction of microscopic charges caused from the physical space between the electron-hole pairs [2]. Those accelerated carriers are coupled to the RF antenna, which is the active transmitter consisting of two small electrodes deposited on the semiconductor substrate lithographically, through a stripline resulting in the emission of coherent THz radiation [Figure 7] [27, 31, 39, 59]. The coupling of the current with the RF antenna and the emission of the THz radiation are enhanced by using substrate lenses - Si lenses - and are described by the Fourier transformation [19, 39].

The Hertzain dipole antenna (this phenomenon is analyzed in detail in Refs 4) is used to describe the PC emitter, since the size of the source ($w_0 \sim 10\mu m$) is smaller than the wavelength of the THz field. A THz far-field radiation can be expressed as follows [4, 36]:

$$E_{THz}(t) = \frac{\mu_0 w_0 \sin\theta}{4\pi r} \frac{\partial}{\partial t_r}[I_{PC}(t_r)]\hat{\theta} \propto \frac{\partial I_{PC}(t)}{\partial t} \quad (1)$$

Where E_{THz} is the THz electric field, r is the distance from the source, and I_{PC} is the photocurrent in the PC gap of the antenna, which is time-dependent. The THz electric field is directly affected by the carrier's lifetime in the PC gap of the antenna

[4, 19].

The transportation of the transient in the PC gap of the antenna can be explained using the Drude-Lorentz model [4, 18]. The surface depletion field results in THz radiation completely polarized by transverse-magnetic (TM) [18]. With the presence of electrons oscillating about their equilibrium positions with very small amplitude, the dominant charge carriers in the LT-GaAs crystal induces transverse electric (TE) [4, 18]. This generates THz pulse with high power due to the high electrons' mobility [4, 18]. The photocurrent in the PC gap of the antenna is proportional to the electron mobility and to the DC bias field [4]:

$$I_{PC}(t_r) = \frac{\sqrt{\pi}}{2}\mu_e E_{DC} I_{opt}[\exp\left(\frac{\tau_p^2}{4\tau_c^2} - \frac{t}{\tau_c}\right).erfc\left(\frac{\tau_p}{2\tau_c} - \frac{t}{\tau_c}\right) - \exp\left(\frac{\tau_p^2}{4\tau_{cs}^2} - \frac{t}{\tau_{cs}}\right).erfc\left(\frac{\tau_p}{2\tau_{cs}} - \frac{t}{\tau_p}\right)$$

(2)

Where E_{DC} is the DC bias field, I_{opt} is the intensity of the optical pulses, μ_e is the electron mobility, τ_s is the momentum relaxation time, τ_c is the carrier lifetime, and τ_p is the optical pulse duration [4]. Therefore, the intensity and the bandwidth of the output THz radiation depend on the physical parameters of the semiconductor and the intensity and duration of the laser's ultrashort pulses [31].

The dipole antenna has various structures including stripline, dipole, bow-tie, and resonant antenna which affect the amplitude and the phase of THz pulses [47, 48]. Bandwidth of the antenna of arbitrary length and recombination time of photo-carries determine the limit of the output THz pulses [39, 47]. The planner antennas are most favorable in THz regime since it maintains the coherence of THz pulses [48].
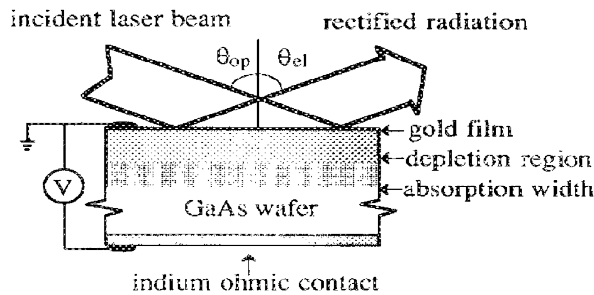
Figure 2.8. The planner antenna [9].

18

A large-aperture antenna and a planner antenna are also utilized in the THz-TDS system to generate THz radiation with high power [50]. The separated area between the two electrodes in the large-aperture antenna is wide enough to allow non-focused illumination technique to be used, unlike the traditional PC antenna that requires focus-excited radiation to reduce the limited potential for the material [2, 12, 50]. Figure 8 shows the planar antenna. A MBE p-i-n diode is utilized in THz wireless communication since the planar antenna is a high power source providing a significantly wide bandwidth[11, 12, 56]. Due to its structure, the planar antenna tolerates high bias field, providing THz pulses with high power [12-13, 16-17]. A magnetic filed with the PC antenna improves the emitted THz power by over an order of magnitude [12, 50, 56].

2.3.3. Photoconductive (PC) Antenna and THz Detection:

An unbiased photoconductive detector antenna is used to detect the broadband THz radiation [2, 3, 57]. PC antenna is an optical sampling technique [18]. Commonly, the material used for the PC antenna detector is the same material used in the PC antenna emitter [2, 3, 36, 59].

Figure 7 shows the detection mechanism. The PC detector is first gated in synchronism with the excitation of the PC THz generator by the femtosecond laser [2, 19, 28, 59], and then the THz pulse generates the electric field by focusing the THz pulse onto the antenna [see Figure 3 and 7] [18]. Therefore, it turns the PC antenna from insulation to conductivity, unlike the case in the biased PC antenna emitter that requires external electric field for creating a photoelectric field [2-5, 55, 59, 60]. The dc THz pulse is then displayed on a PC controlled as a synchronized time-delayed pulse curve [31]. By varying the arrival time of the THz pulse with respect to the probe beam, the amplitude and the phase of the THz pulse can be obtained [41]. The detected signal is proportional to the THz pulse strength, and the number and the lifetime of the carriers [2, 4].

The main advantage in using photoconductive antenna detector is the ability to detect linear or arbitrarily polarized THz pulses with high signal-to-noise ratio, and without complication [52, 60]. However, the lifetime of the carriers and the antenna

structure may imply some limitations [50, 52, 60]. These have been elucidated by Castro-Camus et al. by using a Monte Carlo simulation that provided a new perspective which may optimize the optoelectronic properties of PC antenna [50, 52, 60].

In the PC antenna emitters or receivers, substrate lenses, including collimating and hyper-hemispherical lenses, are used in the back of the PC substrate to collect and reflect the THz pulse to the air preventing the loss of the THz pulse due to propagating through the PC substrate [4, 60]. Currently, the most common materials used in the substrate lenses of PC antenna generators and detectors are high resistivity silicon due to its outstanding features in the THz regime [4].

2.3.4. Optical Rectification for THz Generation:
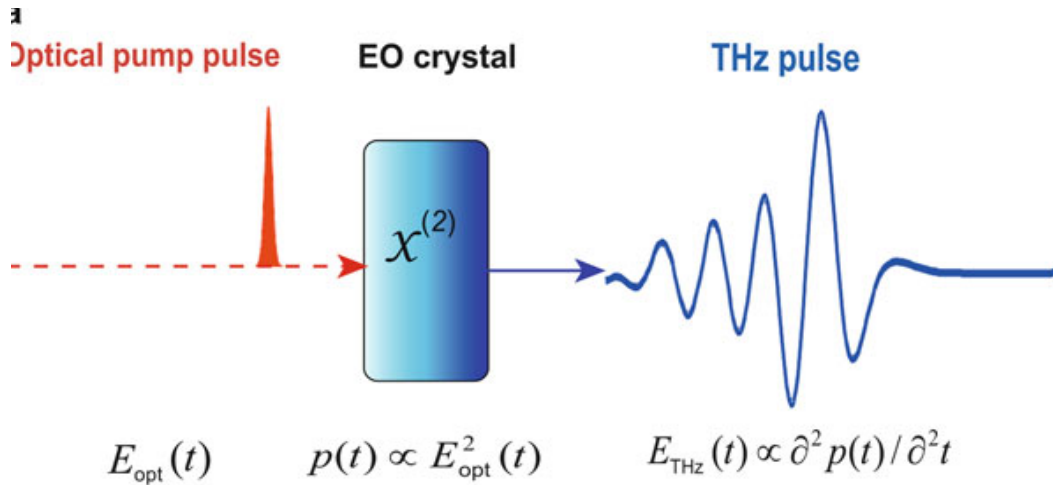
Figure 2.9. Optical rectification [10].

Optical rectification, electron-optical rectification (EOR), or electro- optic (OE) is a nonlinear optical effect in which a femtosecond laser with optical pulses, carrying in its spectrum two frequencies, interacts with a nonlinear medium causing a nonlinear motion to electrons in a crystal, thereby results in a nonlinear mixing of the components to produce a broadband extending up to THz frequency [see Figure 9] [5, 18, 31, 44]. The symmetry of the crystal has to be low in order to induce a second-order nonlinear polarization which causes the nonlinear optical effect [6, 31, 44]. Crystals including Zinc telluride (ZnTe), Gallium arsenide (GaAs), Lithium Tantalate (LiTaO3), Gallium phosphide (GaP), Lithium niobate (LiNbO$_3$), Indium phosphide

20

(InP), and Gallium(II) selenide (GaSe) are used as EO crystal to generate THz radiation[1-4]. Also, electro-optic polymers such as DAPC, DAST, and CFAPC are utilized as THz sources [46, 49, 56]. EO polymers have better phase matching than EO crystals with high EO coefficients [46]. These features may make the use of EO polymers more favorable than EO crystals providing THz system with high SNR[46]. Ultra-broadband THz from 100 THz to over 200 THz has been generated and detected using a 5 fs Ti:sapphire and the DAST crystal [49]. Such high bandwidth frequency is important in telecommunication applications, and may also be used in THz-TDS for characterizing a variety of materials, since, compared with conditional EO crystal, the electro-optic coefficient is much higher [18, 49]. However, due to its hygroscopic character, it is still difficult to utilize experimentally [18].

The ZnTe crystal is the widely used crystal in the THz-TDS technique [1, 4, 18]. Zn has lower electrical charge than Te resulting in different charge distributions, which causes the non-symmetrical structure [7, 4]. The nonlinear optical process in ZnTe are formed by the Ti: sapphire laser since the reflective index of the ZnTe near the wavelength 0.8 μm matches the operational wavelength of Ti: sapphire laser, satisfying the phase-matching condition[1, 4,31]:

$$\frac{dk}{d_\omega}|_\omega \, \Omega = K(\Omega) \quad (3)$$

Where k=ω/c is the wave vector, c=$n_g v_g$ is the speed of light, n_g and v_g are the group velocity and refractive index of medium, and Ω is the THz frequencies range [31]. The above equation is valid, if the $w(n_g)$ of the pulse equals to the THz wave reflective index. Thus phase matching is satisfied when the group velocity of the probe laser pulse equals to the phase velocity of the THz pulse, giving the conversion efficiency of the system [31, 50, 56]:

$$n_g = n(\Omega) \quad (4)$$

Thus, according to Hertzian dipole model, induces a time-dependent polarization, which can be measured at two different frequencies, the sum-frequencies $w_1 + w_3$, which is the energy conservation, and the difference frequencies $w_1 - w_2$, which corresponds to the dc pulse - the THz magnitude [18, 31, 56]:

$$E_{TH}(t, w_1 \pm w_2) \propto \frac{d^2 P(t,w)}{dt^2} = \chi^2 \frac{d^2 I(t,w)}{dt^2} \quad (5)$$

Where $P(t, w)$ is the induced polarization and the $I(t, w)$ is the intensity of the laser pulse [4, 31]. This is valid, if the symmetry of the crystal is highly nonlinear, which determines the magnitude of the induced polarization [4, 6, 56]. Therefore, THz pulse emits only if the sum of the frequencies and the phase matching condition are satisfied between the induced THz radiation and the optical radiations [18].

The main limitation in the OR technique is transverse-optical (TO) phonon resonances [4, 8]. TO phonon resonances cause a strong attenuation to THz waves [4]. The absorption to THz waves differs regarding to the type of the optical reflection's crystal [4].

2.3.5. Electro-Optic Sampling for THz Detecting:

Electro-optic sampling is an optoelectronic technique used to detect the THz pulses emitted from EOR [4, 5, 6, 51]. A linear electro-optic effect or Pockels effect can be utilized to elucidate the electro-optic sampling mechanism [see Figure 10] [4, 6, 10, 56]. In Pockels effect, the electric field of the THz pulse modifies the reflective index of a material; thereby the crystal becomes birefringent [4, 6, 10, 51, 56].
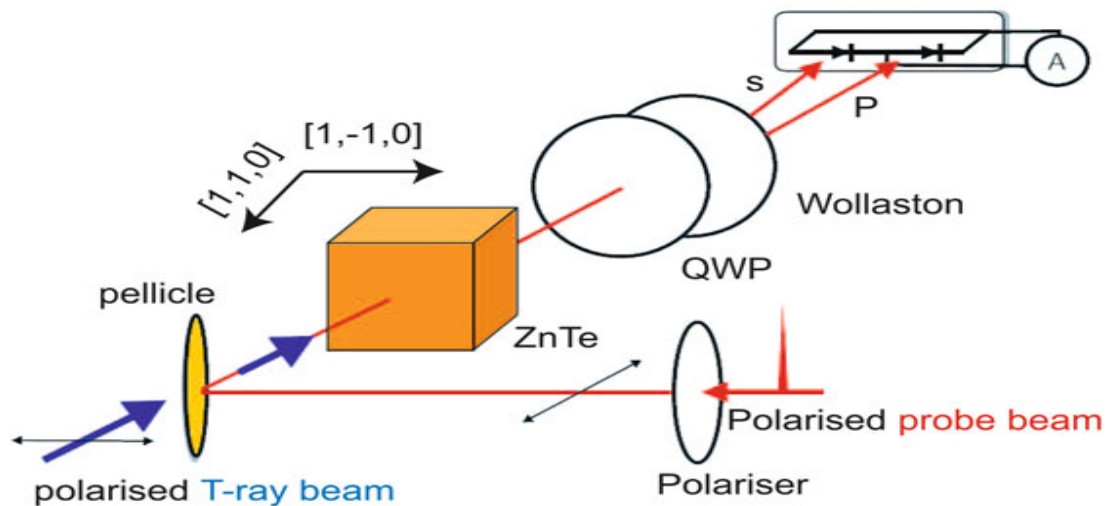
Figure 2.10. Electro-optic sampling [10].

Often the same crystal used to generate the THz pulse by EOR is utilized in the detector, with the same thickness [4, 6, 10, 31]. Figure 4 and 10 exhibit the experimental setup.

After the THz pulse is emitted from the EO crystal, it travels to the EO receiver in synchronicity with the probe beam in which the birefringence induced by the THz electric field is modulated by the time-delayed gating pulse [51]. In other words, a variation in the intensity of the electric field of THz pulses occurred [4, 31, 50]. Thus, electric signals are measured as a function of the time-delay between the arrival time of the THz pulse and the probe-beam by a quarter wave-plate $\left(\frac{\lambda}{4}\right)$, a Wollaston prism, and two balanced photo-detectors [6, 31, 50, 56]. Balance photo-detectors measure the different of frequencies of the THz pulse, which corresponds to the electric field of the pulse displayed in a PC-controlled as a time-delayed pulse curved [6, 31]. The bandwidth of the electrical THz pulse is equivalent to the bandwidth in the THz frequency of the optical pulse emitting from the femtosecond laser [31]. The EO efficiency depends on the duration of the optical pulse and the anti-symmetry of the medium[4, 6, 31, 50].

The main advantage of this technique is the ability to provide a broad bandwidth in order of 50 THz, due to the short duration of the optical fields, without the use of antenna or application of an electric field[18, 31, 56]. Thus electro-optic detection method is more favorable than the PC antenna detection technique [31]. This method is used to detect THz pulses emitting from PC antenna source, which reduces the cost of the system, and gives broadband width [50, 60]. However, the low THz conversion efficiency is a serious drawback of this technique [31].

2.4. Conclusions:

THz-TDS is a powerful spectroscopic tool with great potential in various applications since it is well developed during the past two decades [41]. However, the sensitivity of imaging or characterizing is still not efficient enough for realistic applications [41, 61]. Sensitivity refers to the ability to characterize a little amount of material (a few nanograms or micrograms) or a thin film in order of a few nanometers, along with the ability to provide images with high intrinsically special resolution [41, 61]. Thus the free-space THz-TDS technique, which has been described

in section 3, does not satisfy the requirements of the potential applications, which need high sensitivity [41].

However, in this thesis we will describe a new approach that allows characterization of a sample with a sub-wavelength thickness for quality control issues in organic light emitting diodes (OLED) production using the conventional free-space THz-TDS.

CHAPTER 3

TERAHERTZ CHARECTRIZATION AND THE LIMITATION IN TERAHERTZ SPECTROSCOPY

3.1. Introduction:

Dynamic responses of materials to THz radiation have been explored with the aims of understanding how THz natural's interactions with various materials as well as assisting the development of technologies using THz radiations [18, 82]. Terahertz radiation has the ability to interact with a wide range of materials, such as plastic and paper, and to provide low-energy probing of the system's electronic nature, including inter/intra-molecular motions and Debye relaxation - these are not accessible by other wavelengths [1, 7, 20, 27, 47, 82]. In addition, the non-ionizing nature and the distinctive optical response of a wide range of materials are important for analyzing various applications such as material quality control, pharmaceutical, industrial production lines, and biological [39, 40]. Terahertz waves have been utilized for imaging and spectroscopy, especially Terahertz Time-Domain Spectroscopy (THz-TDS) [45].

Technique	Strengths	Weaknesses
FTIR	✓ High frequency resolution ($\sim 1 cm^{-1}$) ✓ High sensitivity ✓ Broadband (up to 100 THz)	⊛ Cannot interrogate targets under cover ⊛ No coherent detection ⊛ Need cryogenic conditions for high sensitivity ⊛ No real-time data rate
Raman	✓ High frequency resolution ($\sim 1 cm^{-1}$) ✓ Room temperature operation ✓ High sensitivity ✓ High selectivity	⊛ Cannot interrogate targets under cover ⊛ No coherent detection
TDS	✓ Can interrogate targets under cover ✓ Room temperature operation ✓ Coherent detection (amplitude and phase data) ✓ High selectivity ✓ Real-time data rate	⊛ Lower frequency resolution than FTIR ($\sim 10 cm^{-1}$) ⊛ Narrower bandwidth than FTIR (up to 5 THz with standard TDS; up to 20 THz with TDS ABCD system)

Table 3.1. Advantages and disadvantages of Raman spectroscopy, FTIR, and THz-TDS [2].

THz-TDS technique has superior features over other organic spectroscopies or

far-infrared spectroscopies including the very wide bandwidth or high resolution resulting from the ultrashort duration of the THz pulse, and the rapidity of measurements obtained from the high sensitivity of the coherent detection [17, 42, 68]. In comparison to the organic or far-infrared spectroscopies of Raman spectroscopy and Fourier-Transform Infrared Spectroscopy (FTIR), which suffer from experimental difficulties and complexity of theoretical models, THz-TDS is an easy technique to use due to the simplicity in interpreting the THz spectra [see Table 1] [34, 43, 44, 82].

Additionally, THz-TDS provides highly specific signatures of versatile materials which allow for the identifying of or distinguishing between chemical structures such as polymorphism; furthermore, morphology and conformation of the target are obtainable through free-space THz-TDS [26, 40, 42, 44]. Since THz-TDS is both a non-contact and a non-destructive technique, it can even be applied directly in the production site for in-line monitoring [40, 42, 48]. However, with terahertz wavelengths ranging from 100 to 1000 μm, the diffraction limit for this long wavelength light means that it is difficult to measure small volume samples or subwavelength film [39, 53].

Broad bandwidth and time-resolved (more than 1 ps dynamics) features of THz-TDS have been attracting development in thin film sensing, such as for material quality control issues in OLED production [1]. Moreover, the well-established optical techniques including variable angle spectroscopic ellipsometry and phase-contrast microscopy do not have the ability to detect spectroscopic opaque films, due to their invisibility in the visible and near-infrared regions of the spectrum [56].

The importance in sensing sub-wavelength sample thicknesses is amplified for a wide range of cases - in particular, the availability of a small amount of samples such as DNA, explosive, and chemical weapons; or the aim of studying thin sub-wavelength sample properties such as grain size, purity, and strain of material applied in OLED - yet terahertz sensing or characterizing of thin film are still not satisfactory owing to practical and fundamental challenges [1, 30, 43].

The chapter is structured as follows. First, a very brief review is given of the natural interaction between THz radiation with material in which the Drule model has been described. Next, the mechanisms of extracting information from THz spectral including the transmission and the refraction mode have been described for optically thick and thin films. Finally, the efforts which have been made in THz spectroscopy for thin film are summarized.

3.2. THz Interaction with Material:

In general, the electromagnetic wave interacts with the electric charge of the material by various mechanisms including transmission, reflection, refraction, scattering, and diffraction [8, 9]. The type of interaction is determined by the electromagnetic wave properties such as length and strength as well as by the material properties [8, 9]. For example, materials with large unit crystals leave a distinct signature on the THz-ray owing to the long wavelength of the THz wave [8, 9]. These various interactions between the electromagnetic field and the material have been described through different functions including the complex refractive index or the dielectric function [27].

THz wave is comprised of electromagnetic waves carrying frequencies from 0.1 to 30 THz; therefore, THz wave usually interacts with materials as tantamount as the rest of the regions in the electromagnetic spectrum with its discrete signature due to the unique properties of THz radiation [8, 20]. The materials' properties as well as the sample preparation direct the natural interactions of THz ray [8, 19, 20, 58]. For example, interactions with THz wave are controlled by the density of free-carriers in conductors and semiconductors or by intermolecular vibrations corresponding to motions associated with coherent, delocalized movements of large numbers of atoms and molecules known as the phonon lattice modes in crystalline materials [8, 19, 44, 54, 82, 83].

Permittivity or dielectric function $\epsilon = \epsilon_1(\omega) + i\epsilon_2(\omega)$ exemplifies the propagation mechanisms of THz signal into the target or the resistance of the material [27]. In advanced definition, this function endows the ability to describe all of

the relevant characteristics of the interacting materials and THz wave [8, 19]. The refractive and absorption characteristics of THz waves in the material have been described by the real and imaginary parts from the above equation [27, 58].

For solid-sate electrodynamics, extracting the refractive index of a material, describing the refraction phenomena, and determining the target's permittivity and permeability are achieved by using the following equation [8, 19, 27]:

$$n^2 = \tilde{\epsilon}\tilde{\mu} \qquad (1)$$

When $\mu =1$

$$\tilde{n} = \sqrt{\tilde{\epsilon}} \qquad (2)$$

Where μ is permeability of the material describing the target's magnetic response [19, 27]. The permeability of nonmagnetic materials is equal to one [19]. Consideration of nonmagnetic materials over ferromagnetic materials is grounded on THz features that direct the physical interaction with targets [8, 20, 58]. Interaction of THz waves with the magnetic field is weak due to its wavelength, yet THz ray can interact with the magnetic field in metamaterials due to the spatial design [8, 11].

Given THz field traveling through materials, reduction of amplitude and delay of phase have been observed and described as [19]:

$$E_T = E_0 e^{inKl} e^{-\kappa Kl} \qquad (3)$$

Where l and κ are the traveling distance in the material and the extinction coefficient, respectively, and K=$\frac{2\pi n}{\lambda_0}$ [8, 19]. Two general cases of THz wave suffer by propagating into such materials [19]. First, the oscillation period of THz waves is very small compared to the average collision time of carriers resulting in low attenuation of the transmitted THz waves, and consequently real refractive index [19, 58]. Second, most of the propagating THz waves exhibit absorption due to the short collision time of the high carrying density [19].

The interaction between THz radiation with conductors and semiconductors has been determined by investigating the dielectric function [21, 58]. Wave free-carriers on the surface of such materials influence the interaction with THz-waves by causing attenuation to the electric wave [19, 21, 47]. Drude model has been utilized to link the

frequency-dependent dielectric response to the material free-carrier wave due to its simplicity in describing the frequency-dependent conductivity of materials [19, 21, 27, 47]. This model is based in solving the equation of free-carrier motions caused by electromagnetic field as follows [19]:

$$m^* \frac{d^2x}{dt^2} + \frac{m^*}{\tau} \frac{dx}{dt} - qE = 0 \qquad (4)$$

Where m* and τ are the effective mass of the carriers and the average collision time [19]. The complex permittivity has been derived by Cheng et al. through calculating the plasma oscillation frequency (POF) of the material w$_p$ and the angular frequency w to obtain the following formula [19, 21]:

$$\epsilon(\omega) = \epsilon_\infty - \frac{\epsilon_\infty \omega_p^2}{\omega^2 + i\omega\gamma} \qquad (5)$$

$$\omega_p^2 = \frac{e^2 N}{\epsilon_0 m^*} \qquad (6)$$
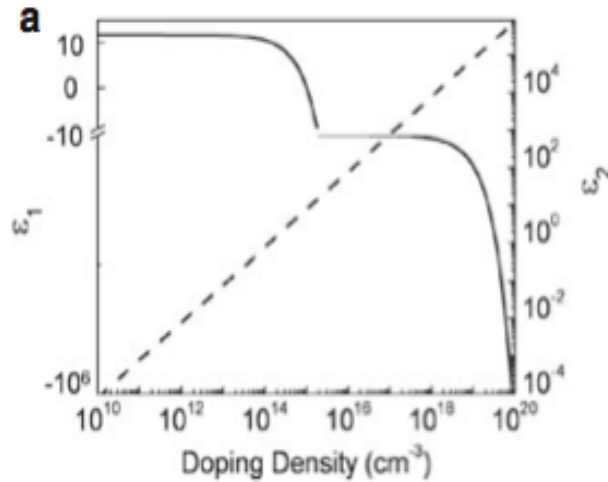
Figure 3.1. THz waves interaction with silicon carrying various doping concentrations, real permittivity ε_1 (solid curve), imaginary permittivity ε_2 (dashed curve) [11].

Where $\gamma = 1/\tau$ is a coherent decay factor of the electrons in the material [19]. Therefore, materials with high free-carriers density N in order of 10[28] m^{-3}, such as metal, have high plasma oscillation frequency in the UV region of the electromagnetic spectrum resulting in a very high resistance on the surface of the metal which prevents THz waves from propagating through the metal [19, 21]. This explains the reason for avoiding the use of a perfect metal such as gold with $\epsilon = -\infty$

and with no skin depth for surface plasmon polarization applications in THz region for long periods of time [21].

Free-carriers density in semiconductors varies based on numerous conditions including the setup of the deposition process and the doping concentration [15, 19, 21]. Intrinsic silicon with free-carriers density of 10^{10} cm^{-3} is a robust demonstration of a high permittivity material to THz waves; it is a transparent material owing to the low frequencies of POF laying in the IR and THz band [19, 21]. Figure 1 shows THz waves interaction with silicon carrying various doping concentrations [19].

The interaction of liquid with THz radiation has been explored by studying the dielectric response of the liquid through applying the Debye relaxation model [32]. Studying the interaction and relaxation of dipoles (which are permanent in polar liquids or induced in non-polar liquids) with THz radiation provides information about the biological function or the type of chemical reaction [32].

Material	Excitation
Semiconductor	Free carrier, phonon, plasmon, LO phonon-plasmon coupled mode, cyclotron resonance, magnetoplasma
Ferroelectrics	Soft mode
Superconductor	Energy gap, quasi-particle excitation, Josephson plasma, 2D plasmon polariton
Photonic crystal	Photonic band gap
Liquid	Relaxation mode
Gas	Rotational level
Polymer	Exciton, polaron, bipolaron hopping
Biomolecules	Collective excitation, biological function

Table 3.2. THz waves react with various materials [3].

Many materials have been investigated in the literature using THz-TDS for various purpose including metamaterials, birefringent materials, and polymers [26, 11, 32, 83]. Different elements in versatile materials respond to THz waves in various ways, as explained by using several different models which will not be elucidated in this work. Table 2 outlines some of these reactions related to specific materials investigated by THz ray.

In THz-TDS technique, Fresnel's laws have been utilized to extract the complex refractive index and the complex reflection coefficient from the transmission or the reflected THz spectra in order to identify or detect the investigated material [8]. The intrinsic complex optical properties are obtainable through the free-space THz-TDS if the volume or the thickness of the sample is sufficient enough to be sensed; hence, the modulation can be performed easily [1].

3.3. Characterization in THz-TDS:
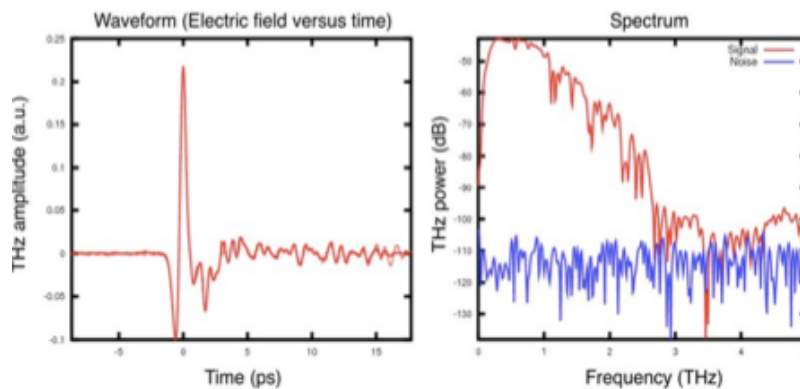
Figure 3.2. THz waveform (on the right), THz waveform after computing the Fourier transforms [12].

Extracting information about materials in THz-TDS from the THz spectrums is known as the inverse electromagnetic problem since no direct investigation of material properties is conducted; instead, the impact of these parameters on the electric field of T-ray is studied [2, 14, 88]. The recorded spectrum of THz electric field signals is time-dependent [2, 8, 26, 88]. The amount of information relies on the bandwidth of the THz waveform that often varies from 0.1 THz to 100 THz depending on the type of THz generator [12]. Furthermore, in THz-TDS technique, experimental set-up of the system is crucial since it determines the system's sensitivity and dynamic range [7]. Versatile methods are used to extract materials' properties from the electric signals in THz-TDS, such as preliminary scanning for a reference signal followed by taking the ratio between the electric signal of the sample and reference, or by investigating material features upon a signal spectrum [7, 10, 32, 52].

31

Amplitude and phase of the THz pulse after interacting with the sample are obtainable for extracting materials' properties by comparing the time-resolved electric field of terahertz pulses before and after propagating through the sample with different temporal delays [see Figure 2] [3, 14, 44, 69]. Alternatively, a technique of dual thickness is used for recording THz spectrums for the sample of interest that has been prepared with two different thicknesses: one as a reference and the other as a target [12, 50]. Optical properties of the target are then obtained by comparing the two THz waveforms, yet the Fresnel loss from the surface of the sample is not considered in the calculation of the reflective index if the same sample with various thicknesses is used [12].
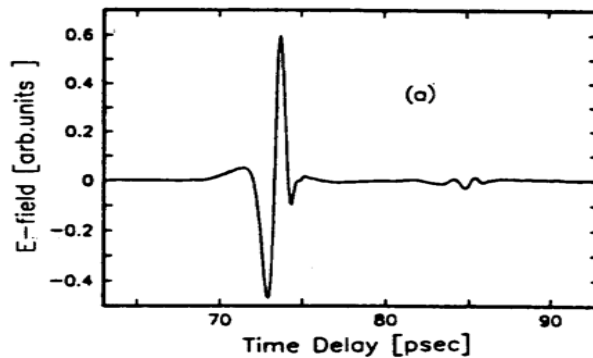
Figure 3.3. The first peak (ordinary signal) at 73 psec refers to the recorded THz pulse when the C-axis of the crystal perpendicular to the polarization, the second small peak (the extraordinary signal) at 85 psec corresponds to the reflected when the E is parallel to the C axis [13].

The above characterization method is based on recording the THz spectrum from a series of THz pulses and probe pulses with various time delays for both the sample and the reference [12, 65, 66, 69, 88]. Another similar sampling technique is performed where instead of implanting a series of THz pulses, a single laser pulse is used to characterize the target [12]. Although this technique allows THz-TDS to be used in detecting the moving or stationary sample with a short scanning time, strong THz signals are required to implement the single laser pulse detection technique [12].

Spectroscopy through terahertz TDS can be performed in two modes, transmission and refraction mode, based on the nature of the material. However, the transmission mode is the prevailing structure in the literature because of the obtaining of reliable and quantitative terahertz spectra [44, 68]. The refraction

configuration requires considerable calibration; thus, it is primarily utilized for detecting opaque samples. However, few works have used the reflection mode in characterizing [44].

3.3.1. Transmission Mode:

Transmission mode has been implanted in studying the surface properties of the sample such as excitation, bulk or superstrate layer of a sample's properties, as well as characterization and detection of a variety of materials including explosive, pharamatcular, protein, and polymer if the thickness of the sample is optically detectable through THz-TDS [3, 13, 54, 75, 82]. Analyzing those properties is based on deduction of the signal-to-noise ratio (SNR) and of the frequency-dependent dynamic range (DR) that must be high since the change in the transmitted waveform shaped from the material's characteristic frequency response is an explicit reference for the kind of material [4, 75, 78].

Arguably the sensitivity of this system can be described by its ability to detect slight changes with a high signal compared to the background noise, which is determined by multiple factors including the experimental set up or the type and the thickness of the sample [1, 43 66].

Generally, THz-TDS has a high sensitivity with a high SNR owing to the utilization of the time-gating detection, which offers an internal resolution for the THz pulse in ps as well as avoids the Johnson noise [3, 23, 30, 50, 66]. Also, the polarization sensitivity of THz-TDS has been determined to be high since 1966 by the characterization of y-cut sapphire sample with its C axis parallel to the surface [28, 43]. This sapphire has a number of active lattice modes in the THz band [13, 28]. Finding the ratio between the ordinary signal, as reflected when the electric field is perpendicular to the C axis, to the extraordinary signal, as reflected when the E is parallel to the C axis [see Figure 3], has been calculated to be approximately 25:1 [13, 28, 70]. This gives the ordinary index of refraction n_o = 3.07, which shows an increase in the absorption coefficient for thick target with weak higher frequencies stemming from limiting the range of

the reliable data to 2 THz from the wide bandwidth [70]. However, Jeoen et al. have investigated how to resolve this by determining the DR for the operating system [4].

The thickness and the type of the sample are of capital importance in the characterization process through THz-TDS because of yielding the lowest measurement uncertainty in the optical constants [1, 3, 14, 62, 64, 66, 67, 78]. THz signal suffers from a strong attenuation with optically dense samples, such as high doping semiconductors with large thickness causing obscuring of the THz signal into the background noise, or multiple reflections in the sample resulting in overlapping of the THz signals; thus, the transmission mode cannot be applied [14, 78].

Optically thick material in the range of hundred of microns, or optically thin material with high conductively or high hydrogen level thickness in the range of nanometers have been measured through the transmission mode of THz-TDS with high SNR [1, 18, 36, 61, 78]. Further cases are manifested in many optically thin materials such as polymer, in which the highest sensitivity of conventional THz-TDS with 10^7 SNR ration is considered low for sensing because of the difficulty in detecting phase shifts that are less than the coherence length of the THz radiation (~ 150 um) [50, 64, 73]. Several approaches aimed to increase the sensitivity of the THz-TDS system for sensing such films are described later [1, 50, 67, 73].

Extracting dielectric and optical properties of a target through THz-TDS transmission mode will be interpreted for two sample configurations: optically thick sample and optically thin sample.

Before embarking on a detailed discussion of extracting information related to materials' properties through the transmission mode, the noise sources and the relation between the SNR and DR need to be addressed. Because analyzing materials' properties is based on deduction of the SNR and DR [4, 12-15].

3.3.2. Signal-to-Noise Ratio and Dynamic Range:

Noise sources in THz-TDS system are manifested into two categories, random

noise sources and systematic noise sources [65, 66, 75, 78]. The random noise sources could occur from jitter in the delay stage, sample relocation, laser intensity fluctuation, and optical and electronic white noise in the detection system [4, 12, 17, 66]. The sources of systematic noise are exemplified in recording errors, mechanical drift, etc [66, 78]. Noises in the usual case of spectroscopy by THz-TDS, regardless of what the noise stems from, are controllable through computational treatment such as Central Limit Theorem, due to the high SNR obtained from a target with a thickness comparable to or larger than the THz wavelength (1 THz = 300 μm) [66, 75, 78]. However, if the film thickness is thinner than THz wavelength, then the effect of the noise sources have to be considered to avoid misinterpretation of the dielectric properties of the target [4, 12, 17, 66].

Various methods have appeared to alleviate these fundamental and mechanical noises. The simplest method utilized to obtain a high-resolution characterization by avoiding the multiple THz reflection while propagating in the sample sweeps over a long delay range from 7.5 GHz or less to higher frequencies in order of 4 THz [29].

Lock-in amplifier technique has been used in THz-TDS system with the aim of obtaining characterization of THz spectrum with high SNR through reducing the noise from the laser fluctuation [12, 52, 78]. This approach is based on monitoring the output signal from the detector by enabling THz pulse with certain frequency and phase amplified and detected for THz measurements [12, 52]. The efficiency of this technique in diminishing the noise level in THz signal is poor due to the impact of the mechanical drift [12]. Only approximately 10^{-6} noise reduction from the original noise has been reported since the lock-in technique works only on the probe laser beam noise and not on the THz pulse noise because the noise carried in THz pulse has the same frequencies and phase [12]. However, a mechanical chopper modulating the pump beam at a certain frequency has been used to increase the SNR [52]. For example, investigating polymer targets including PP, PET, and PMMA through THz-TDS exhibits changes in the refractive index of less than 6%, from 1.4 to 1.8 with discrete behaviours for the absorption coefficient of each polymer due to its

frequency-dependency [52]. In this case the mechanical chopper is adjusted to modulate the pump beam at 2 kHz [52]. Anther approach is based on using two-dimensional contour plots of the root mean-square (rms) error usually applied between conceptual and experiment data to minimize the uncertainty measurements as well as to illustrate the important parameters in a model [27].

The uncertainty in THz measurements raised from the lack of delimiting the target's thickness has been resolved by using the optimum thickness model [78]. This model is encompassed by two choices: performing the spectroscopic either on a wide bandwidth or at a certain frequency regarding the required precision in the measurements; of these, the latter spectroscopic technique is more accurate [78].
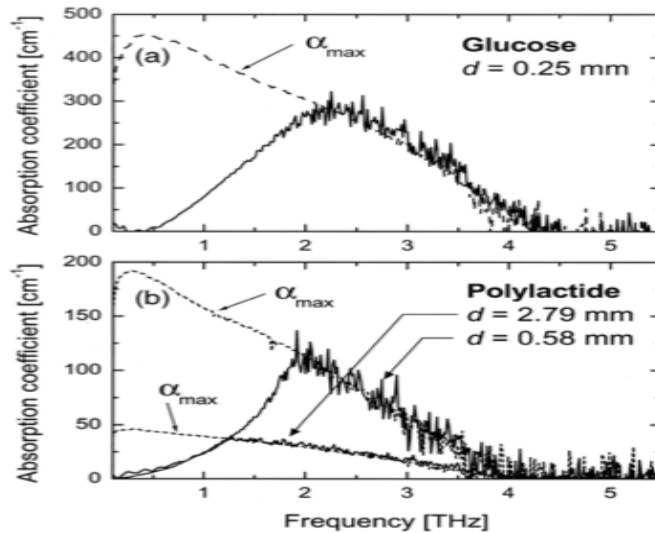
Figure 3.4. (a) and (b) the dashed curve refer to the DR of the experimental measurement, determining the reliable measured for both samples [14].

Dynamic range has been explained as the strength of the reference signal, or the maximum signal generated by the emitter, compared to the associated noise floor of the system, which is the minimum signal detectable [26, 43]. THz-TDS has a wider dynamic range compared with other infrared conventional spectroscopies since it calculates the electric field of the THz wave rather than its intensity [23, 75]. In many instances, high sensitivity THz-TDS has potential in characterizing a target which has as a low transmission coefficient, for example, in order of 10^{-8}, with high SNR [23]. Figure 4 exemplifies the frequency-dependence of DR and the importance of

36

determining the DR for quantitative analysis by indicating the validity of the THz measurements [4].

3.3.3. Optically Thick Sample:

Extracting information about materials' properties through the transmission mode encompasses the following steps [12-15, 40, 63]:

1- Recording THz signals twice - reference signal and sample signal;
2- Calculating the complex transmission coefficient from the ratio of Fourier transformation of the reference and the sample signals; and
3- Extracting materials' properties through calculating the complex refraction index from the transmission coefficient, which is usually implemented to solve the inverse problem.

3.3.3.a. Recording THz Signals:
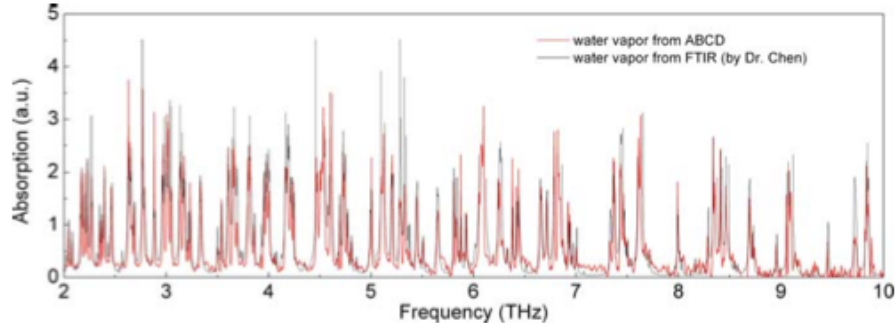
Figure 3.5. Absorption spectrum of water vapor within bandwidth from 2 to 10 THz [11].

Two THz signals in time-domain are measured after traveling through the transmission set up without sample: reference signal and with sample, as described in Chapter 2 [2, 5, 13, 26, 84]. The reference signal has been recorded first to establish the reliable scanning range frequency, which is affected by the THz pulse duration and the time resolution of the receiver. Thus, the scanning range frequency increases as long as the pulse duration and/or the time resolution of the detector go down [13, 27]. Recording of reference signal is commonly performed in nitrogen-purged atmosphere to diminish THz absorption induced by ambient humidity [15, 42, 54].

Utilizing THz air-breakdown-coherent -detection (ABCD) with FTIR approaches on characterizing the interaction between THz frequencies from 2 to 10 THz and the water vividly show the effect of the strong absorption of the reflective vibration and rotation transitions of water molecules [see Figure 5] [19].
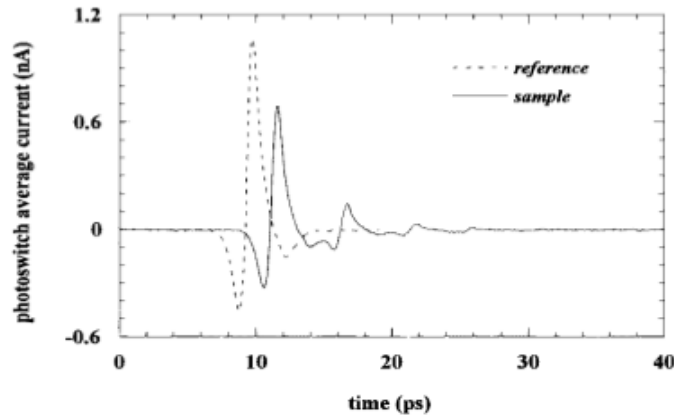
Figure 3.6. Dashed curve and solid curve show the measured THz pulse for the reference and the sample respectively, p-type doped Si with 225 μm thick [15].

Recording the target signal is performed by placing the sample into THz propagating path between the THz generator and detector. This leads to change in the THz phase due to time delay, and reduces the magnitude of the THz signal owing to traveling through the target thickness [see Figure 6] [27, 59, 60, 61]. Deconvolving the sample pulse with a reference pulse has been utilized to extract the optical properties of the target [12, 26, 33, 50]. The time-dependency of the THs pulse has been measured by scanning the time delay between the excitation pulse and the probe pulse [27, 66, 75, 84, 86].

3.3.3.b. Calculating the Complex Transmission Coefficient:

38
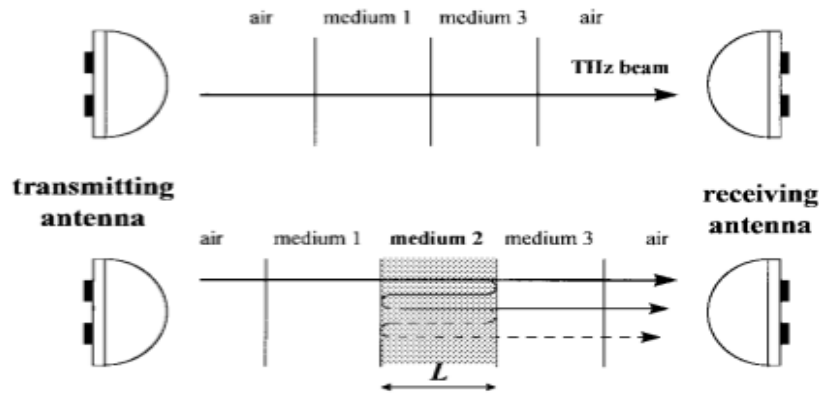
Figure 3.7. The THz pulse path between the source and the detector; upper part and lower part indicated recorded THz pulse for the reference and the sample respectively. In the lower part medium 2 present the sample with thickness L, only the transmitted THz pulse through the sample is considered by using time-window technique [15].

Versatile techniques have been used to obtain the complex refractive index of many materials [14, 15, 69]. One characterization technique, which is described here, is based on comparing THz signals from two samples with the same materials but different thicknesses [14, 15]. For a well-known thickness, the optical properties can be extracted experimentally by using equation (7) [27]. To avoid an overestimation of the calculated complex refractive index raised from beam defocusing, a collimated beam or long-focal length beam has been utilized with such samples [78]. However, in the case of an arbitrary thickness, the complex refractive index has been calculated numerically and then compared with the experimental data; alternatively, extracting the optical properties from different echoes will give the actual value of the sample thickness [14, 69].

Fast Fourier Transform (FFT) has been applied on recorded signals by traveling the three-medium (air-dielectric-air, Fabry-perot resonator) to calculate the frequency-dependent complex permittivity of the target [see Figure 7] [14-16, 23, 55, 75]. Since the THz signal is a measurement of the electric field of the THz wave, the absorption coefficient refers to the attenuation in electric field, which is half of the absorption coefficient calculated for the field intensity [43]. This allows the THz transmission spectrums to encompass the magnitude and the phase of the signals which can be given by [15, 26, 27, 29]:

39

$$E_s(\omega)/E_r(\omega) = t(p,\omega) = \frac{T(p,\omega)_{sample}}{T(p,\omega)_{ref}} = \tau(\omega)\, r^p P^{2p+1}(\omega,d).\exp\left[j\,\frac{\omega d}{c}\right] F_{rsr}(\omega) \quad (7)$$

Where t (p, ω) is the complex transmission coefficient defined as the ratio of the electric field between the sample E_s and the reference E_r [14, 15]. $T(p,\omega)_{sample}$ and $T(p,\omega)_{ref}$ are the complex transmission spectrums [15]. r(ω), P(ω,d), and $\tau(\omega)$ are the reflection, propagation coefficient, and transmission respectively [15]. The thickness of the sample and the radial frequency are d and w [15]. F_{rsr} refers to a Fabry-Perot defined as $F_{rsr}(\omega) = \sum_{i=0}^{i}[r_{sr}^2 \exp{(i\,\frac{2\tilde{n}(\omega)\omega d}{c})}]^i$ due to Fresnel losses, and i is the number of internal refraction [27]. The symbol p refers to the temporal echoes observed in the transmission spectrums resulting from the etalon effect [see Figure 8] [15, 43, 69].
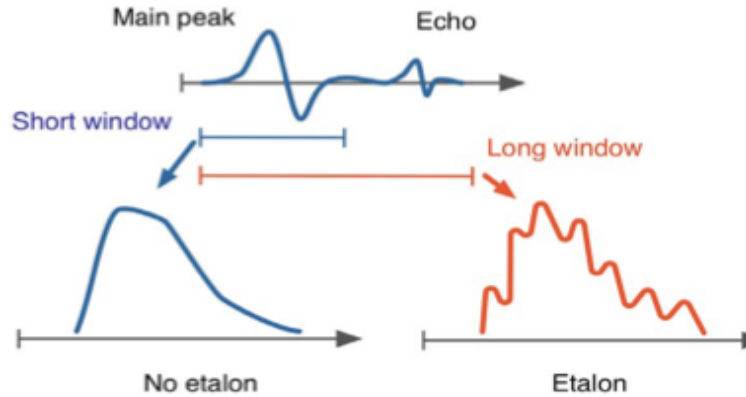
Figure 3.8. Fourier transform when applying the time gating (short window) approach for echo number 0 (the main peak), and the opposite case illustrated in the measurement with long window [12].

Considering the temporal echoes makes this technique stand out among other methods due to the accuracy and efficacy obtained through evaluating the confidence interval in a measurement [15, 64, 69]. Extracting the material properties is achieved only on the directly transmitted pulse corresponding to echo zero (p=0), which does not suffer from internal reflection inside the sample [17, 69]. The time window approach has been carried out to explore the directly transmitted THz pulse, while other echoes appearing from the reflection of the THz pulse at the interfaces of optical elements such as beam splitters and lenses are isolated from the measurements of extracting the optical properties of the target [17, 43, 55]. If the

waveform scan-length is long enough, then these echoes show up as smaller replicas of the main pulse [17, 43]. These echoes have been utilized to explore random errors in the THz-TDS system [17]. THz waveform is considered to be suffering from etalon effect, if these echoes are included in the Fourier Transform [see Figure 8] [43]. In addition, some works in the literature do not consider the Fabry-Perot (FP) effect in the measurements of optically thick sample, assuming that Fresnel losses from the recorded THz spectra are already removed from applying the temporal window of the signal [68, 77].

The absorption coefficient $\alpha(\omega)$ and the refractive index n (ω) are obtained from the two spectra of pulses after finding the amplitude A (ω) and phase $\emptyset$ (ω) of the electric field [4, 8, 12, 13, 15]:

$$\alpha(w) = -\frac{2}{(2p+1)d} \ln \left\{ A(p,w) \frac{[n(w)+1]^{2p+2}}{4n(n-1)^{2p}} \right\} \quad (8)$$

$$n(w) = \frac{1}{2p+1} \cdot (1 - {^c\!/\!_{wd}}) \emptyset(v) \quad (9)$$

Calculating the absorption coefficient in the transmission mode is frequency-dependent based on a number of constraints including the sample thickness and the range of the DR [4]. Usually the frequency range extends from 0.1 GHz to 5 THz in conventional PC THz-TDS [4, 13, 26, 34]. Recently, air/plasma polymer emitter in THz-TDS provides a broad bandwidth from 0.1 to 10 THz, bringing the THz technology close to broadband imaging, standoff detection, materials identification, and quantification [36]. Figure 9 shows the broad bandwidth characterization [36].

In conventional THz-TDS, **at low frequencies the absorption coefficient** of the sample under investigation can be easily calculated from the above equation (8) [4, 26, 55]. Owing to the use of high-brightness and short-pulse source, THz-TDS has the potential to characterize targets with relatively high absorption coefficient [55].

However, **at high frequencies, extracting the absorption coefficient** from the THz spectrum is limited to the dynamic range of the experiment, which can be integrated by applying a roll-off approach [4]. The roll-off technique has been

explored by Kojima et al. to study properties of the PMMA at high frequencies using a THz-TDS to extract the complex refractive index of the PMMA as well as in an attempt to understand the origin of Boson Peak (BP) [59]. In the roll-off method, first a noise floor (electronic noise) of the system spectrum accounted by blocking the THz beam path is determined [4, 43, 59]. Frequency-dependent dynamic range (DR) of the experiment is obtained by normalizing the THz reference pulse and the sample pulse spectrums from the noise floor spectrum [see Figure 4] [4, 26]. The absorption coefficient at high frequencies can be calculated from the following equation [4]:

$$\alpha_{max}d = 2 \ln \{DR \frac{4n}{(n+1)^2}\} \qquad (10)$$
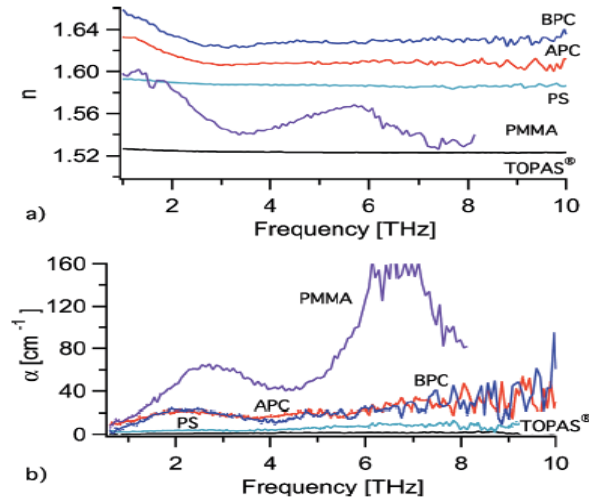
Figure 3.9. The refractive index and the absorption coefficient for different polymers recorded in wide bandwidth from 0.1 to 10 THz in THz-TDS system [16].

As long as the absorption coefficient value is below or equal to the maximum absorption coefficient with a specific DR, then the absorption coefficient for the sample is reliable [4, 17, 26]. Moreover, in order to consider the measurement of the absorption coefficient as a sample property, the value of the absorption coefficient has to be within the DR. This highlights the advantage of determining the DR, which helps to avoid the misinterpretation of the value of the absorption coefficient of the sample and determine the cut-off frequency [4, 12].

Cut-off frequency differs regarding the material and the thickness of the samples and the DR of the system [4]. For example, material with high reflective index such as amorphous glucose with a thickness of 0.25 mm allows reliable measurements of

the absorption coefficient within frequencies ranging from 0.1 to 5 THz [see Figure 4] [4].

The reflective index in the transition mode is given by equation (9) [4]. This index is frequency independent, so there is no effect of the DR on the extracting value of the reflective index of the sample [4].

The absorption spectrum for THz radiation has been used to identify and characterize the target. Databases including Terahertz Database (http://thzdb.org) consist of the absorption range in THz range for a large number of materials [32].

For optically thin material with high conductivity, modification of the equations (7) has been performed to calculate the dielectric properties of the thin film with slightly different techniques in recording the THz signals [1, 18, 15, 26, 62, 68]. Recording THz signals in sensing thin film differs in that besides recording THz signals with and without the sample, the substrate of the sample is scanned and the THz scanning is performed on the film on the substrate to avoid the effect of the substrate on the film in calculating the film's features [62, 68]. For conductive thin film, negligible optical thickness [nwd/c << 1, and kwd/c <<1] assumption has been considered [27, 63, 68]. Also, the frequency-dependent conductivity is calculated to find the complex refractive index [18, 23]. This presumption leads to the application of changes in the Fabry-Perot part in equation (7) by considering the assumption limit of Fabry-Perot (i=infinity "the number of internal refraction") and inserting this in the transmission coefficient formula to obtain the following [27, 63]:

$$t(w) = \frac{2}{2 + i\sigma d Z_0} \quad (11)$$

Where Z_0 is the impedance of free space, and σ is the conductivity of the film [27]. Film with a few nanometers of thicknesses can be measured in the conventional transmission mode of THz-TDS [1, 18, 27, 62, 63, 68].

Optically thin film with a high hydrogen level has been detected either by taking the measurements many times (such as 20 times) on the sample, or by using metallic mesh-based biosensor, waveguides, or filters along with implanting different calculation techniques [60, 61, 66].

3.3.4. Optically Thin Sample:
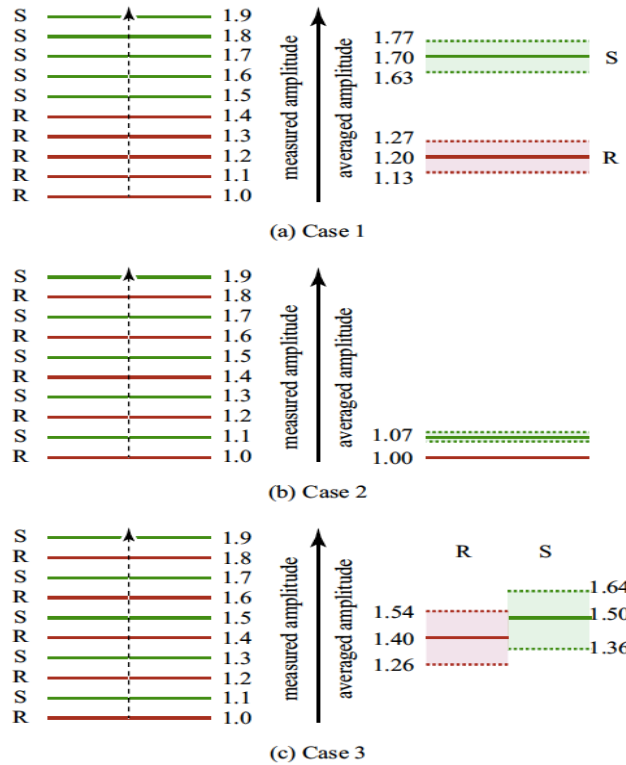
Figure 3.10. reduce measurements uncertainty by constraining all of the noise sources into the confidence intervals (case 3) [17].

Sub-wavelength film, small amount of samples, or thin film are descriptions employed to refer to a target with a film thickness much less than a wavelength which cannot be detected by THz-TDS due to its small complex refractive index, thus no THz phase changes have been observed [1, 18, 36, 64, 66]. Many factors contributing to such limitation of sensing have been observed in THz thin film sensing including Fabry-Perot effect (etalon effect) in which the main transmitted pulse and the partial internal reflection are overlapped, as well as short interaction time between the material and THz wave in which no changes are observed in the THz signals between the reference and the target [1, 4, 18, 50]. Further elements are demonstrated [1, 4, 18, 50, 64, 66, 77]: 1- low SNR due to low system sensitivity for sensing small changes in the THz signal; 2- the femtosecond laser system influencing the THz generation is not stable, resulting in fluctuation in the generated and detected T-ray; 3- the chance of determining the real thickness of the sample owing to its properties; 4- long wavelength of the THz wave resulting in reduction in the sensitivity of the

system; and 5- basic signal loss for T-ray such as water absorption.

Two conditions have been established by Withawat[64] to describe the properties of the minimum thickness of freestanding film under free-space THz-TDS measurement [1, 4, 18, 64]. However, these cases are limited to freestanding film [1, 66]. Recently, Withawat et al. have successfully detected a round 2 μm film with a level of confidence of 68% through conventional THz-TDS [66]. This technique has the ability to sense common thin-film configurations through performing alternative scans on the sample and the reference and then taking the scans average for the sample and the reference separately [66]. By this method, the uncertainty in measurements is reduced by constraining all of the noise sources into the confidence intervals [see Figure 10] [66]. Two equations have been established to describe the minimum detectable thickness by conventional THz-TDS as follows [66]:

$$l_{c,m} > \frac{k_p}{|\Delta k|} \frac{c}{\omega} \sqrt{\frac{2}{N_r}} \, s_{In|E_r|} \quad (12)$$

$$l_{c,p} > \frac{k_p}{|\Delta n - 2n_f \Re(\rho_{total})/[\Re(\rho_{total})]|} \frac{c}{\omega} \sqrt{\frac{2}{N_r}} \, s_{arg(E_r)} \quad (13)$$

Where $l_{c,m}$ and $l_{c,p}$ are the amplitude-based critical thickness and the phase-based critical thickness utilized to detect and characterize the target respectively [66]. k_p is a coverage factor which can be 1, 2, and 3 defined confidence intervals with a level of confidence of 68, 95, and 99.7%, consecutively [66]. Standard deviation $s_{arg(Er)}$ obtained from a set of repeated reference measurements using the Monte Carlo method after the phase of each measurement is properly unwrapped and extrapolated [66]. The following equations have been used to calculate the optical constants $\Delta n(\omega)$ and $\Delta k(\omega)$ (the amplitude counterpart) and the phase component $arg(H(\omega))$ of thin film [66]:

$$\Delta n(\omega) > \frac{k_p}{\sqrt{N}} S_n(\omega) \quad (14)$$

$$\Delta k(\omega) > \frac{k_p}{\sqrt{N}} S_k(\omega) \quad (15)$$

$$\arg(H(\omega)) = \arg(E_s) - \arg(E_r) = \arg(\tau_{total}) - \Delta n \frac{\omega l}{c} + \arg(FP_f) \quad (16)$$

Where $\Delta n(\omega)$ and $\Delta k(\omega)$ are the difference in the real refractive index and extinction coefficients of the sample and reference materials, $S_n(\omega)$ and $S_k(\omega)$ are the empirical standard deviations of the sample refractive index and extinction coefficient respectively, N denotes the number of sample measurements, and $\tau_{total} = \frac{\tau_{af}\tau_{fs}}{\tau_{as}}$ describes the total of the complex Fresnel coefficients [1, 4, 18, 64, 66]. Utilizing the phase component to extract the sample properties for the detection purpose is more reliable than the amplitude counterpart [66].

As feature sizes move toward 100 nm; chip frequencies are scaled up to the upper gigahertz range; the need increases for a THz frequency, non-contact, room temperature scanning system; then the importance of thin film characterization and detection thrusts the development towards present or new technologies, which are presented in Table 3 [1, 50]. These approaches aim to increase the sensitivity of the THz-TDS system [50]. Table 3 summarizes the differences between various approaches used to sense thin film [1]. Establishing a stringent comparison between these approaches for the purpose of determining which one is the best in sensing thin film is subjective because each approach utilizes different measurements, has various requirements in the configuration of the sample, and may or may not be designed for characterization or detection [1]. However, links between the techniques are elucidated to provide an overview before embarking into details.

Approach	Scheme	Complexity	Contact	Thickness	Material $n - j\kappa$
Mod. trans.	C	High	N	300 nm [43]	Parylene-n 1.62
Mod. reflect.	C	High	N	3.3 µm [52]	Polyarylether 1.67
Waveguide	C	Moderate	Y	20 nm[a] [68]	Water $2 - j0.5$
Filter	D	Moderate	Y	40–80 nm [88]	DNA $1.05 - j0.07$
Metamaterial	D	Low	Y	50 nm [103]	Silicon-nanospheres 3.42
Plasmonics	D	Moderate	Y	50 nm[b] [148]	"Absorbing analyte" $2.08 - j1.2$

Table 3.3. This table is adopted from reference 1, highlighting the differences between the approached used in developing the THz thin film spectroscopy [4].

Modulations in the transmission mode and the refraction mode and use of THz waveguides have been utilized in thin film characterization due to their wide broadband [1]. Despite the complexity in modulating the transmission and refraction modes of THz-TDS system compared to applying the THz waveguides method, they offer non-contact free-space measurements [1, 76]. Giving non-contact measurements endows a variety of options to prepared samples, and avoids uncertainty in measurements resulting from apparatus-sample reactions [48, 57]. Although there are constraints on the frequency scanning range, the resolution of the system varies from the contact measurements, and the coupling and propagation experiences losses in THz waveguides technique, THz waveguides are most favourable for use in characterization owing to the system's high sensitivity and simplicity [1, 70, 72, 76].

As illustrated in the Table 3, metamaterial-based sensing is the simplest in comparison to the filter and plasmonics detection systems in the sense of the straight conducting of free-space measurements on metamaterial substrate [1, 80]. **In our work, we successfully obtain this feature by introducing the SPR device as a substrate to the thin film into the free-space THz-TDS transmission mode, which also has been demonstrated by other groups.** Aside from the system's complexity, on-chip filter-based method is more advantageous than the metamaterial devices due to the high selectivity and throughput, which are important factors for industrial applications [1, 79]. Comparing the sensitivity of the three systems is not necessary because of the different applied measurements, various necessities in the configuration of the sample, and the materials of the sample [1].

Two main techniques are utilized in thin film THz-time domain spectroscopy: developing the algorithms applied for the optically thick film, and enhancing the signal and reducing the noise level [1, 18, 23]. The enhancement in algorithms is performed in conventional free-space THz-TDS [23]. On the contrary, the improvement in SNR has been achieved through reconfiguring THz-TDS system, or using the free-space THz-TDS configuration by allowing the terahertz surface wave

to traverse a greater length of analyte through using the concept of the THz plasmonic or waveguides [1, 15, 18, 39]. **In our work we characterize 2 μm PMMA by using the SPR device with conventional transmission mode Terahertz TDS [37].**

3.3.4.a. Improvement by Algorithm:

The nature of materials contributes to making scanning through THz-TDS possible or not, even though their thicknesses are considered optically thin [1, 23]. Signal-processing algorithms have been employed to enhance the STN ratio of the recorded THz signals by almost 30% [47].

Spatially Variant Moving Average Filter (SVMAF) has been utilized in sensing thin film through THz-TDS [1, 2]. This method is based on enhancing the optical material parameter extraction technique by reducing the noise effect on the recorded THz spectra, hence enabling THz-TDS to detect samples with 100 μm thickness [2]. The obtained complex refractive index from any changes in the detected THz signal is reliable as long as those measurements fall under the dynamic range of the system, as discussed in section 3.3.1 [2, 4].

Further algorithm approach is based on diminishing the uncertainty measurement by determining the sample thickness at the same time as recording the complex refractive index [1, 2]. This is performed by applying the total variation technique with Nelder-Mead search [2]. Fourier transformation is utilized on the recorded signal, as affected from many reflection spectra due to Fabry-Perot (FP) effect [1, 2]. Using the real thickness of the sample to model the THz spectra minimizes the Fabry-Perot effect, thus resulting in detecting a sample with 28 μm thickness [1]. Alternatively, Scheller et al. have established an algorithm approach to detect thin film with non-uniform surface by the transmission mode for conventional THz-TDS [73]. This approach is based on applying an additional Fourier transformation on the recorded THz pulse suffering from FP effect and the obtained complex refractive index resulting in analyzing material features in a quasi space domain [73, 77]. However, the real refractive index of the target has been deemed in driving the time domain error functions [73, 77]. Later work has combined the initial estimation of

frequency domain by QA, and Nelder–Mead approaches to determine time domain error functions have been introduced through considering the complex refractive index of the material [77].

3.3.4.b. Improvement by Enhancing Signal or Reducing Noise:
3.3.4.b.1. Metamaterials:

Artificially structured materials or metamaterials have been used for a variety of applications at THz frequencies, mainly to overcome a number of limitations in terahertz technology including modulation device for THz wave modulating 50% of THz transmission wave as well as improving THz transmission through photonic crystals [23]. Strong magnetic behaviour has been observed when THz waves interact with specially designed metamaterials [1, 23, 80], despite the fact that there is a weak influence of the magnetic materials on THz frequencies due to the short THz wavelength compared to electromagnetic wave counterparts such as radio wave [23].
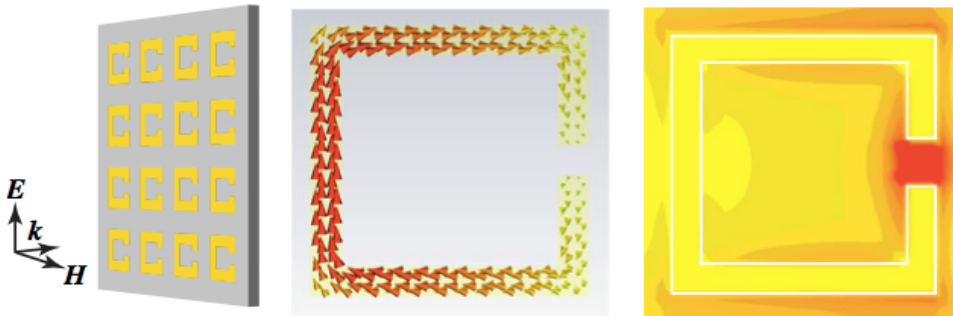
Figure 3.11. The SRR device and the electric field distribution over the surface of a single SRR on resonance [18].

Split-Ring Resonator (SRR) and high Q-factor resonators are planar metamaterials which have been investigated widely for sensing thin film[1]. The capital advantage of SRR and high Q-factor resonators is that they do not require modulation on the configuration of the conventional THz-TDS [1, 49, 71, 79]. SRR is the first approach created from metamaterials implanted in sensing thin film with a theoretical ability to sense film as thin as 10 nm [1, 71]. SRR consists of a nested pair of concentric rings with slits or gaps etched in opposite sides placed in a certain shape forming a loop with an open gap [see Figure 11] [1]. The primary key pursues the structure of split-ring resonators, whose natural oscillation frequencies rely

49

critically on the permittivity of the boarding dielectrics [71]. However, the diffraction-limited spot size of the terahertz beam excitation (~1 mm) constrains the minimum thickness of the sample deposited in the SRR device, unless the near-field sensing is applied [1, 49, 79].

High Q-factor resonator is a near field technique utilized to confine the THz spot size beam into a resulting small diameter [1, 38, 79, 80]. The operating idea is tantamount with the SRR device, yet it has the ability to recognize a very small shift in the THz pulse. This results in a noticeable change in the recorded THz transmission pulse because sensing close to the sub-diffraction terahertz source leads to alleviating the number of excited resonators, and minimal film areas result in increasing the Q factor and decreasing the sample volume [1, 38, 79]. This technique has high potential for moving THz thin film sensing applications to industry purposes due to its great number of advantages. Further details are available in References 1 and 79.
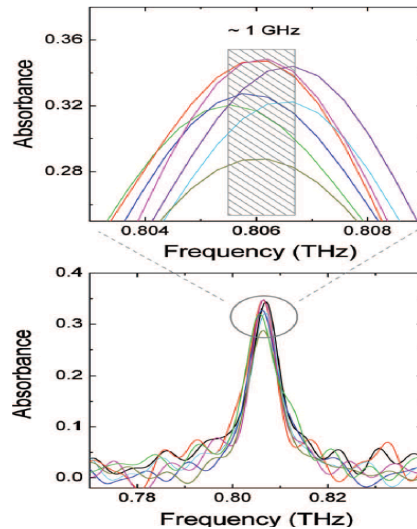
Figure 3.12. Narrow THz spectra provided by applying the waveguide technique. The absorption spectra of the lowest frequency mode of the 4INBP/Al film [19].

3.3.4.b.2. Waveguides:

Utilizing waveguides with terahertz TDS system has been developed to improve the characterizing and sensing abilities of THz-TDS technique due to various advantages [1, 70, 76, 81]. This process endows time-resolved scanning with picosecond with the following: 1- secure and long-path with high pressure for toxic materials

and precious gases [1, 67, 70, 76]; 2- narrow THz spectra are provided at cryogenic temperatures associated with the vibrational modes of the molecules with no need for high power [see Figure 12] [67, 70, 72, 74, 76]; and 3- long interaction time is allowed with the THz signal reducing the analyte amount to 1/100 of the amount required to be used in free-space terahertz TDS due to the increase in the system's sensitivity [1, 70, 72, 74].

Two major configurations of the waveguide with different kinds of materials including dielectric or metal have been implemented in THz technology: Parallle-Plate Waveguide (PPWG) and Microstrip Waveguide [see Figures 13] [1, 67, 70, 72, 81]. These specific waveguide configurations have been utilized into THz-TDS because of their ability to hamper the THz pulse from the high group velocity dispersion when propagating into the waveguide is alleviated [70, 72]. The microstrip waveguide differs from the PPWG in structure and performance [1]. Transmission lines fabricated on a chip guide the terahertz wave to propagate along those lines [1]. This technique is not utilized in sensing thin film, yet it has been implemented in characterizing various optically thick materials [1].
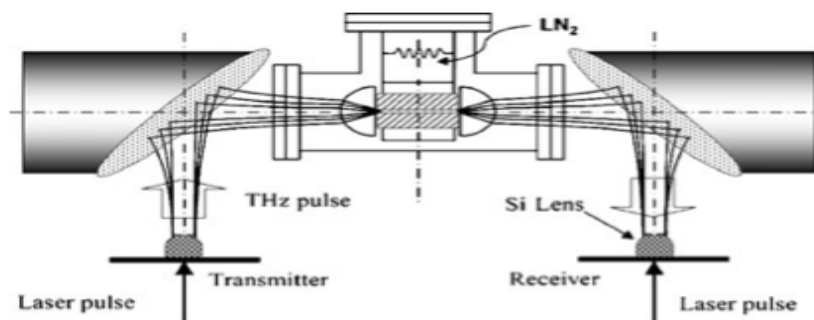
Figure 3.13. The configuration of waveguide THz-TDS system (PPWG TDS) [19].

PPWG TDS is well-known for sensing thin film including biological molecules, pharmaceutical materials, and explosives with thicknesses as low as 20 nm, even though the film is not uniform, due to the high transmission amplitude of the THz (approximately 35%) when coupling the THz waves with TEM mode or 20% without coupling to the TEM mode normalized to the transmission amplitude of the THz by the free-space TDS method [1, 67, 70, 74, 76]. Despite the advantages mentioned

above, PPMG TDS has many instrumentation limitations regarding the potential of this technique including restricting the broad range of the conventional THz system. As well, the technique of sample preparation or sample interaction with the waveguide material makes the characterization of unknown sample by PPWG TDS unreliable [1, 67].

3.3.4.b.3. Filters and Resonators:

This technique combines the concept of both waveguides and resonators [1]. Filter loaded transmission line and photonic crystal waveguide conceptually exemplify the use of this approach for thin film sensing [1, 71]. Here, 10^3 times less target quantity than the conventional THz-TDS has been successfully detected through differentiating between the refractive index of various analyte, yet no information has been obtained about the natural frequency on the molecule [1, 51, 60]. Most of the work has applied these two techniques by implanting on materials that respond resonantly at THz frequencies such as DNA and some explosive materials [1, 60, 71]. THz sensing for biomolecules develops the label-free detection technique, which is more advantageous than the complexity and non-reproducibility of a fluorescent labeling-based approach [60, 71]. Therefore, details about this technique are beyond the scope of this thesis since the ability and sensitivity of detecting thin film cannot be compared or generalized to counterpart sensing techniques. References 1 and 51 provide more information.

3.3.4.b.4. Terahertz Plasmonic:

Surface plasmon polaritons (SPPs) at metal-dielectric interfaces have been proven for several decades as a reliable technique for surface analysis and investigation of thin films due to the two dimensional nature of SPPs and the strong electromagnetic field at the interface which allows for obtaining measurements of thin film spectroscopy including optical and dielectric constants, film thickness, and inhomogeneities with high precision [85-87]. **Our technique is based on utilizing THz SPP wave in sensing the organic material of thin films for quality control issues, as discussed in Chapter 4.**

3.3.4.b.5. Modified Transmission Mode THz-TDS:

This technique differs from the previous approaches in that it is based on reducing the noise to enhance the sensitivity and hence the SNR [1, 50].

Differential Time-Domain Spectroscopy (DTDS) approach has been utilized to increase the SNR in characterizing samples with μm-thickness [15, 18, 50]. DTDS has the ability to detect phase changes of less than 0.6 fs [50]. A galvanometer attaches to the conventional terahertz TDS to enable swapping the target and the reference within 0.1 to 0.01 sec [1, 15]. On the other hand, exchanging the reference and the sample requires one or several minute(s) to complete, which results in noise and signal drift in the measurements [1, 15, 18]. However, the galvanometer by itself can not alleviate the noise effectively; hence, a lock-in amplifier or a system with double lock-in amplifier is utilized beside the galvanometer to remove the noise from the laser fluctuation [1, 18].
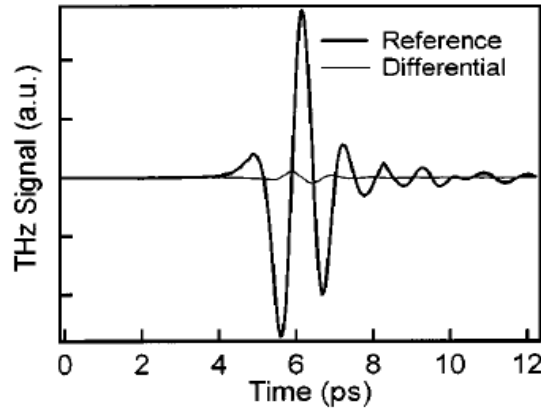
Figure 3.14. THz waveform of the differential and the reference in terahertz DTDS system [20].

Extracting optical properties of the target in DTDS technique is based on calculating the refractive index of the target by finding the ratio of the differential amplitude to the field amplitude as follows [18]:

$$E_{diff}(\omega) \equiv E_{film}(\omega) - E_{ref}(\omega) \quad (17)$$

$$n = \left| \frac{E_{diff}(\omega)}{E_{ref}(\omega)} \right| \qquad (18)$$

Figure 14 depicts the THz wave of both the reference and the differential signals [18]. DTDS approach provides access for THz-TDS to characterize sample with um-thickness or less through reducing the noise level and taking advantage of increasing the dynamic range of the measurements [1, 18]. A further appealing feature of applying the DTDS approach in bio-sensing applications is that it not only detects the change in the refractive index between the samples, such as the resonator and cavity technique; but also gives information about the nature of the changes in the molecules, for example, by detecting morphological changes in living cell monolayers [1]. This approach has great potential for industrial applications in the future once the cost of the lock-in amplifiers and the computational complexity has been overcome through establishing alternative means [1, 73].
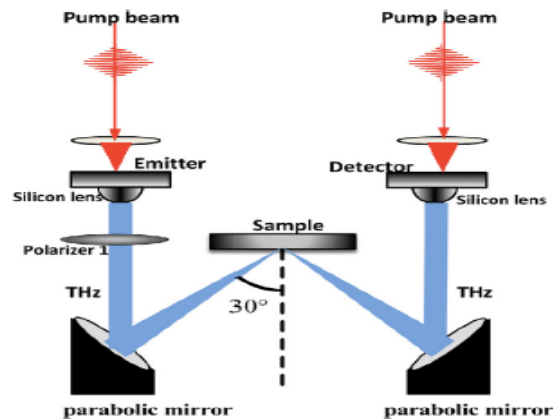
Figure 3.15. A schematic diagram of the THz ellipsometer technique [21].

Alternately, characterizing a freestanding film with 2 μm thickness is simply achieved through attaching a Michelson interferometry into the conventional THz-TDS which causes the splitting of a THz beam into two paths: one with a 180-degree shift from the other path to probe the sample [1, 50, 56]. Recombining the two signals results in destructive interference [1, 50, 56]. Removing the noise resulting from laser fluctuations enhances the depth and the special resolution of the measurements [1, 50, 56].

3.3.5. Reflection Mode:

Reflection mode is utilized based on the type of extraction data and sample properties [5, 55]. Samples with high conductivity and optical density or samples with low transmittance are more desirable to be detected or characterized through reflection mode due to the huge attenuation for the transmitted THz pulse [5, 31]. For example, measuring the dielectric properties for a dielectric or a semiconductor material is more easily achieved by the reflection mode owing to the large absorption coefficient, which gives more accurate characterizing data for the sample [4]. Two major configurations for the reflection mode in THz-TDS are utilized: terahertz ellipsometric and Attenuated Total Reflection (ATR) system [46].
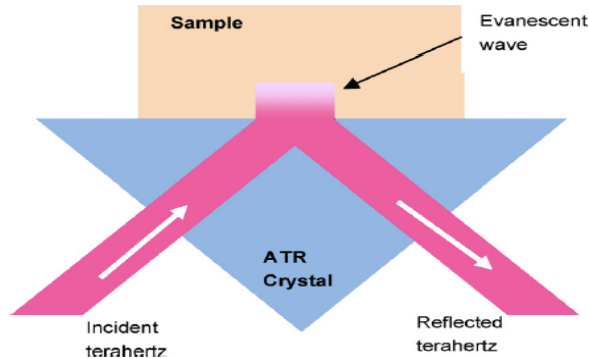
Figure 3.16. Terahertz ellipsometric and Attenuated Total Reflection (ATR) system [22].

Figure 15 depicts a schematic diagram of the THz ellipsometer technique [31]. THz ellipsometer characterizing technique is built on providing the optical and dielectric features of the target with no need to reference measurement through employing THz polarizer and designing an optical path by complex configuration [10, 46]. Extracting information about the materials has been explored by converting the S and P polarized complex reflectance of the target to the ellipsometric angle, which is the function of the material's complex refractive index [1, 10, 46]. To date, Lai et al. have demonstrated an easy and simple mechanism to measure the optical and dielectric properties with no need to use complex configuration by placing a wire-grid polarizer in front of the sample with a specific angle which can be changed by using a fixed rotation angle [31]. Therefore, a simple signature in the reflected signal reveals changes in the polarization state of the already polarized incident signal on the

sample [31]. However, the reflected signal has to be strong with strong S-polarized radiation to be sensible [1]. A highly sensitive THz source and detector including Backward Wave Oscillator (BWO) are mandatory for use in detecting low-reflective target [1].

As illustrated in Figure 16, ATR is a technique which uses a Dove prism, a triangular prism made from high reflective index, low dispersion and transmission loss such as silicon [26, 44, 46]. Terahertz ATR measurements have been performed directly simply by placing a small amount of powder or liquid sample onto the crystal [26, 44, 46]. When the incident THz with angle is more than the critical angle on the prism, it exhibits a total reflection from the surface of the prism [26, 44, 46]. The optical properties can be obtained from two scans with and without the sample [26, 44, 46]. ATR technique does not require sample preparation and a small amount of the sample can be sufficient [26, 44]. However, this technique is not used for rapid screening of many samples because it is not suitable for characterization due to the need for complex calibration [26, 44].

Extracting optical properties from the reflected THz pulse is performed by a method similar to the extraction of optical properties from the transmitted THz pulse [4-6, 19, 44, 83]. The only differences are the use of a highly reflective metal mirror with a reflection coefficient of minus unity, such as Au mirror, to measure the reference signal; as well, the complex refractive index is calculated from the ratio between the reflection electric fields from the reference and the target [4, 5, 8, 23, 31]. The detector receives reflected THz signals with reflection of p (parallel reflection), s (perpendicular reflection), and polarization wave considering Fresnel principles [19, 23]. The absorption coefficient and the refractive index are calculated from the reflection coefficient as follows [4]:

$$|r| \exp(i\emptyset) = \frac{\hat{n}-1}{\hat{n}+1} = \frac{n+ik-1}{n+ik+1} \quad (17)$$

$$n = \frac{1-|r|^2}{1+|r|^2-2|r|cos\emptyset} \quad (18)$$

$$\alpha = \frac{4\pi v}{c} = \frac{2|r|sin\emptyset}{1+|r|^2-2|r|cos\emptyset} \quad (19)$$

One significant drawback in the reflective mode is the isolated characterizing of the sample and the reference signal causing misplacement errors [8, 31, 83]. This leads to uncertainty in calculating the complex reflective index because the sample position in the reflective mode directly controls the THz phase [31]. However, versatile approaches have been reported in the literature regarding the misplacement inaccuracy [31, 44, 83]. For example, maximum entropy principle has been utilized in correction of the phase shift [8, 31]. Given its high efficiency in rectifying small misplacement error in order of ± 1 um, this technique is the most novel method [8, 31]. A further technique for solving the misplacement error is based on measuring the P and S THz wave polarization by utilizing the conventional THz ellipsometer method [31]. This technique has advantages over the maximum entropy technique in determining the optical properties of the target in addition to the dielectric features, as well as its simplicity [31].

3.3.5.a. Modified Reflection Mode THz-TDS:

An approach based on remolding reflection mode for THz-TDS and using substrate for the target material has been utilized in THz thin film sensing technology [1]. The key point in this approach is taking advantage of THz's ability to distinguish between the film and the substrate due to propagating through film-substrate interface; this significantly enhances the detectable signal for the thin film [1]. Three techniques - terahertz ellipsometry, goniometric terahertz TDS, and thin-film interface - have been reported in the literature as employing the purpose of sensing film with a subwavelength thickness by THz rays [1, 44, 46, 83].

The concept of terahertz ellipsometry has been introduced in Section 5. Terahertz ellipsometry for thin-film sensing has not been well-established because of the need for strong THz generator and highly sensitive detection, yet a number of works have been reported in sensing thin semiconductor and metamaterials film [1].

Goniometric terahertz TDS (GTDS) is based on improving the recorded signal from thin film by carrying on a series of complex reflected signals at different angles

to identify the Brewster angle of the film/material interface in order to obtain the changes in the phase around the Brewster angle [1]. Not a lot of work on GTDS in sensing thin film has been utilized because of the alignment required from the complex hardware [1].

Reflection from the two interfaces of the substrate-backed film in the reflection mode of THz-TDS has been demonstrated to enhance the reflected signal from thin film [1]. In this technique, the thickness and the complex refractive index of the thin film are extracted at the same time through applying a theoretical model beside the experimental result [1]. Thicknesses of 15 μm have been detected by this approach [1]. Given 30 THz of bandwidth, film with thickness in order of 1 μm is expected to be measured [1]. It is anticipated that the use of nonlinear THz generator and detector will improve the sensing signal from the thin film by using this technique since the recorded signal from the interface has been observed to occur beyond the convectional THz-TDS bandwidth limit [1].

3.4. Detection and Characterization:
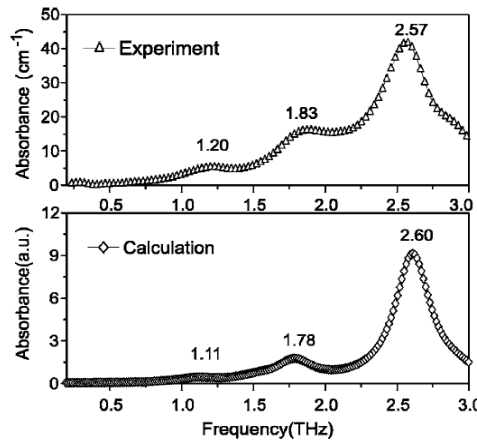
Figure 3.17. For optimum characterization results from THz-TDS the experimental and the theoretical calculation are performed on the sample (here MDMA) [23].

Density Functional Theory (DFT), Partial Least Square (PLS) regression, Gaussian, Crystal, CPMD, Castep, and VASP exemplify some of the computational software that has been used to elucidate the origin of THz absorption spectrums owing to the lack of group characteristic frequency in THz spectra of analyte

materials [32, 33]. The solid-state DFT has been demonstrated to reproduce crystalline structures and THz spectra with accuracy unparalleled by other methods because of its ability to consider all kinds of motions including intra/inter molecular regardless of the need for a significant number of computational resources [41, 65, 83]. Using waveguide THz-TDS in developing these theoretical models is expected to broaden the use of THz-TDS in industrial applications due to its helpfulness in predicting and understanding solid-state THz vibrational spectra, thus improving the precision in identifying and characterizing materials [72].

Generally, numerical simulations vary regarding whether THz-TDS system is designed for detection or characterization [1, 26, 32]. Alternatively, other approaches have been developed for calculating optical properties of the target theoretically with respect to the experimental results [26, 32]. The combination between experimental and theoretical results optimizes the efficiency and accuracy of applying THz-TDS in characterization [see Figure 17] [32, 33, 34, 41].
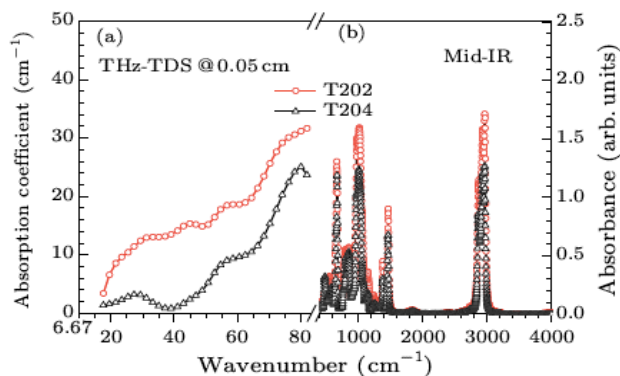
Figure 3.18. Studying changes in THz signals in the lower-wavenumber region for T202 and T204 versus changing one property of the target, such as concentration. At the higher-wavenumber region the MIR spectrometer is preferred due to the lower STR of THz-TDS at high frequencies [24].

The essence of any characterization system is the accuracy in the analyst data because for empirical applications, probing a target is necessary for detecting the kind of analyte and quantitatively estimating its content in mixtures using knowledge of spectral data of various molecule components that require a THz-TDS system with high sensitivity, which is subject to various factors [1, 55, 78]. Free-space THz-TDS offers accurate identification of sample compositions with the quantity of

each component owing to the very broad bandwidth containing a large amount of information obtained in time-resolved [1, 48]. Quantitative analysis in THz-TDS is performed by studying changes in THz signals for a sample versus changing one property of the target, such as concentration [see Figure 18] [26, 32, 35, 41].

Homogeneous samples or samples with crystalline structure are much more easily characterized than heterogeneous samples or samples with amorphous structure due to their uniform and parallel surface as well as their strong absorption peak [1, 32, 35, 65]. Thus, applying a linear least squares regression is made possible, and is utilized to examine the reliability of the experimental result [see Figure 19] [1, 32, 35, 65].
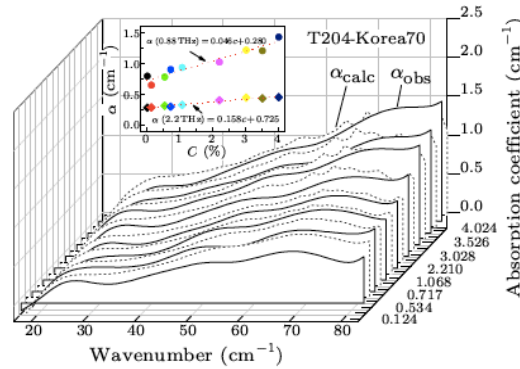
Figure 3.19. Compression between THz measurements experimentally "solid line" and theoretically "dotted line". The inset illustrate different concentrations of the simples computed theoretically at 0.88 and 2.2 THz [24].

In contrast, heterogeneous samples leave various features on THz spectra causing a mandatory need to use algorithm software such as (PLS) regression [1, 32]. King et al. have manifested the presence of effect or influence between the lattice phonon modes upon each other, resulting on simultaneous absorption which can be resolved using PLS [26, 32].

Conventional THz-TDS detection system does not require determination of samples' dimension and geometry; therefore, there is no need to identify the intrinsic broadband properties [1, 32, 55, 64]. Ideally, sufficient contrast and shift in frequency between the sample and reference samples are enough to detect samples, leading to the conclusion that only equation (14) should be satisfied in considering

the film detectable or not [64]. Principal Component Analysis (PCA) is a chemometric method used in the detection system of THz-TDS to identify the material, which results in frequency shift in THz spectra due to its refractive index [1, 32].

Consequently, free-space THz-TDS is capable of detecting samples with thicknesses smaller than those used for characterization, and only the noise in the system (the sensitivity of the detection) has an impact on the detected signal [64, 66]. This lack in the quantitative analysis results from both uncertainties in determining the geometry of the sample as well as the high electronic noise compared to THz signal [1, 64, 66].

Other computational models have been implemented to reduce the level of uncertainty in THz measurements, such as a Monte Carlo simulation and Withawat et al. model [75]. These models can be applied to obtain a reliable measurement when the evaluation of uncertainty is critical such as in detecting explosive material and in pharmaceutical materials for quality control [75].

3.5. Conclusion and Outlook:

Up until the present, THz-TDS has proven its potential whether in characterizing, detecting, or imaging in a ubiquitous range of applications including tomographic imaging, quality control of packaged goods, high-temperature superconductor characterization, label-free genetic analysis, and chemical and biological sensing [45, 47, 48, 84].

In many instances, the ability to extract the absorption coefficient and the refractive index directly from the THz spectrum in THz-TDS offers advantages over other spectroscopic techniques in that it endows calculation of the complex refractive index and the complex permittivity of the sample while avoiding the uncertainty caused by Kramers–Kronig or by implementing more than the spectroscopic technique on the same sample to obtain different information [7, 12, 22, 23, 28, 59]. THz-TDS is a coherent technique with pulsed radiation allowing for characterization with time-gated approach resulting in the development of terahertz imaging and the following advantages [27, 32, 44-47, 60]: 1- carrying out the

experiment at room temperature in less than 20 ms, because applying the time-gated detection avoids the extraneous ambient noise; and 2- Fabry-Perot reflections can be taken away from the recorded spectrum [27]. As a further appealing feature over other IR spectroscopy techniques, characterization of organic materials by THz-TDS provides information on both molecular conformation and the intermolecular environment with safety and high internal resolution, such as distinguishing between polymorphism and chirality [29, 30, 32, 47-51, 57, 84]. Therefore, THz-TDS has replaced the linear spectroscopy Far-IR Fourier-Transform Spectroscopy for characterization materials in the range between 20 and 500 μm. As well, THz-TDS has become more favourable for use in characterizing organic materials compared to a molecular organic conductor (TTF-TCNQ) owing to its complexity [45, 63].
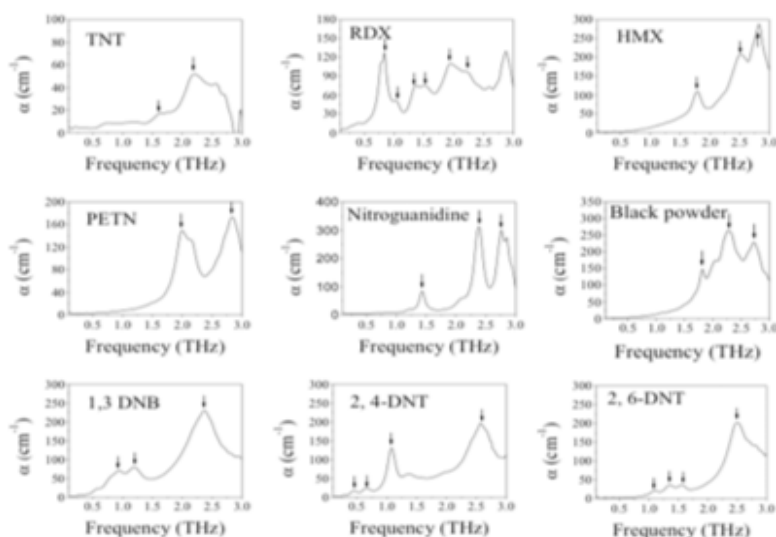
Figure 3.20. Number of the explosive materials that have been detected and identified by THz-TDS [12].

Since THz-TDS is a non-contact and real time detection technique, it is used in explosive identification at standoff distances of a few centimeters while imaging the distribution of the spectral characteristics of the structures [43, 48, 54, 57]. Figure 20 shows some of the explosive materials that have been detected and identified by THz-TDS [43]. These materials can be detected with very low levels of radiation compared to X and gamma ray, even in plastic, paper, non-metallic materials, and

cloth due to the ability of THz wave to penetrate such materials [41-43, 48, 57, 74, 84].
Figure 21 illustrates a real time terahertz TDS device for explosive identification [43].
THz wand prototype is being used to scan people without need to perform hand-
searching [57].

In addition, nanostructures have been characterized through THz-TDS in order to
explore the physics behind the quantum confinement phenomena in characterizing
versatile devices such as semiconductor devices or medical devices [24, 25, 32]. To date,
the results of the extensive research in this area are that THz-TDS offers a resolution
of up to $\lambda/3000$ and a video-rate recording for THz near field imaging, which is an
appealing feature over IR illumination in, for example, cancer diagnosis [53, 54].

Zomega's Micro-Z handheld THz time-domain spectrometer

Figure 3.21. A real time terahertz TDS device for explosive identification [12].

However, the strong absorption of water molecules hampers the standoff
distance detection by limiting the detection distance to a few centimeters or less
than a meter, as well as by preventing THz-TDS from identifying or detecting
materials which have a resonance near a water line [43, 74]. The low THz photon
energy poses inherent difficulties in the detailed interpretation of weak complex
intermolecular interaction [44]. On the other hand, these features of THz ray are very
attractive for biological spectroscopy and imaging applications since, for example,
THz ray can distinguish the unnatural supply of blood and water in cancer areas
within the human body [54].

THz-TDS in sensing thin film has been outdone to some extent by some of the

spectroscopic techniques through, for example, avoiding the impact of the dead-layer effect on thin-film measurements and providing a direct window into the complex refractive index of the film [66, 68]. Also, for THz-TDS thin film spectroscopy and imaging, targets with micron thickness or less have been successfully characterized or imaged using DTDS or waveguides approaches [66, 50]. The current challenge is to perform spectroscopy and imaging tasks by using the conventional transmission mode for THz-TDS without a need to compensate in price, algorithm, or system complexity.

Terahertz TDS has enormous potential to become a detector for many industrial applications deducting from the above features and developments and because its three configurations - transmission, reflection, and imaging - open up the possibility of effectively and efficiently sensing a variety of samples. To live up to its enormous inherent potential, THz-TDS should be developed to offer reliable measurements both swiftly and inexpensively including enhancement in the software used to identify materials probed by THz radiation.

That motivates us to implement THz radiation to characterize materials such as PMMA and those used in organic light emitting diode (OLED) to address the material quality control issues in OLED production. This characterization has been conducted using the conventional transmission THz Time Domain Spectroscopy. We investigate the characteristic of thin PMMA film using terahertz surface plasmon near-field sensor. The reasons behind choosing terahertz plasmon over other approaches, discussed in this chapter, will be clarified after introducing the following chapter.

CHAPTER 4

TERAHERTZ PLASMONIC AND TERAHERTZ SURFACE PLASMON RESONANACE (SPR) NEAR-FIELD SENSOR

4.1. Introduction:

Compact devices have fueled a quest of concentrating and guiding electromagnetic waves into small volumes, resulting in the innovation of waveguides, transmission lines, plasmonics, and optical fibers [1]. Plasmonics are being explored to generate, propagate, and detect plasmonic waves [25]. An alternative definition of plasmonics is to guide and manipulate the electromagnetic wave beyond the diffraction limit and combine photonics, nanotechnology, and electronics [6, 8, 11-13]. For example, the use of surface plasmons enables the confining of EM waves into a small volume (this is unachievable by the conventional focusing techniques and dielectric lenses), as well as minimizing the length scales of photonic circuits through concentrated and channeled light by utilizing subwavelength structures [6, 8, 11-13, 38]. Before the plasmonic generation, fabricated nanoelectronic devices containing photonic circuits were challenged because the optical components, which are encompassed from optical fibers and waveguides, could not be scaled down owing to prevention by the diffraction of the confinement of propagating light when optical fibers and waveguides dimensions became smaller than the propagating wavelength [25].

The history of plasmonics dates back to 1902 when Wood reported an observation of narrow dark bands where visible polarized light was reflected on a metallic grating [4, 7, 10]. This phenomenon was explained theoretically by Otto and

Raether as surface plasmons (SP) causing a drop in reflectivity in the attenuated total reflection method [4, 7]. SP is an oscillation of electron waves on the boundary between metal and dielectric induced from the electric field of the electromagnetic wave impinging on the metal surface [1-4, 9]. A hybrid of electromagnetic wave and SP wave is called Surface Plasmon Polarization (SPP) [1, 2, 8, 12].

In the late 1970s, SPP was utilized in sensing thin film applications due to the tremendous field enhancement associated with SPP waves [4, 6, 8]. Most works focused on applying the optical frequencies through using noble metals because frequencies of free-electro waves on noble metals lay in the optical and ultraviolet regime, thereby determining the coupling nature [1, 6]. In another words, since the permittivity of metals is very small at the optical and ultraviolet frequencies, the penetration of the electromagnetic field carrying these frequencies is considerably great yielding in strong confinement [1, 8]. Depositing dielectric thin film on the surface of metals has significant impact on properties of SPP waves, hence allowing for the identification or characterization of the film because the propagating characteristic of SPP is extremely sensitive to any changes in its surrounding medias [4, 5].

In addition to detecting thin film, SP waves have been explored for their potential in various devices including magneto-optic data storage, microscopy, surface-enhanced Raman scattering, surface plasmon spectroscopy, and surface plasmon resonance sensors [3, 6, 8]. SP concept has matured greatly within a large area of applications in optical frequencies compared to terahertz frequencies due to the intrinsic plasma frequency on the conductor being present in the visible and UV range [1-4]. Radiation carrying THz frequencies is weakly confined to free-electron waves on the metals due to the large permittivity and ohmic losses of metals at THz frequencies which leads to the large propagating length of the SPP [1]. In addition, compared to the frequencies of counterparts in the electromagnetic spectrum, confining THz radiation into a sub-millimeter scale poses inherent difficulties by using conventional means such as coupled photonic-crystal resonators and stripline

resonators due to its long wavelength [38].

However, as mentioned in the previous chapter, exploring the importance of THz sensing for a variety of applications has led to the investigation and development of THz technologies. For THz plasmons, two major approaches have been proposed to confine THz ray into subwavelength structure and strengthen the confinement of SPP in THz regime: SPP on semiconductors or SPP on metals with surfaces containing holes or grooves [1, 4, 5].

Our goal is to fabricate SPR near-field sensor to characterize thin organic film and those used in organic light emitting diode (OLED) production to meet the challenge of material characterization and sensing in the terahertz (THz) range. The advantage of high near-field enhancement and confinement at the boundary between the SPR structure and dielectric layer makes the proposed sensor operating in the Terahertz region pertinent for material sensing [68].

Two SPR devices containing **either** 2D periodic circular or square hole array in 500 nm Al on an 5 mm-thick intrinsic silicon, **or** a single subwavelength aperture surrounded by concentric periodic grooves of a set period in a metal plate (which is known as a Bull's eye structure), were fabricated by following the micro-fabrications process encompassed from UV photolithography and wet and dry etching to transfer the pattern into the Al film. As explained in chapter 3 about THz spectrum measurement through conventional THz-TDS, the SPR device consisting of 2D periodic circular or square hole array with and without thin Poly(methyl methacrylate) (PMMA) film on it is placed at the focus of the THz beam in transmission THz-TDS, where the spectrum is obtained from the Fourier-transformed sample and reference THz pulses. The transmission is obtained from the ratio between the sample spectrum and reference spectrum, whereas the phase change is the phase difference between the two spectra. To avoid overlap with water absorption lines, the optimal SPR device design has a period of 320 μm and square holes of 150 μm side length. We successfully confirmed the theoretical SPR frequencies for metal-silicon mode and demonstrated a shift to 0.9211 THz due to 2

μm of PMMA layer on the surface [68].

This chapter is organized as follows: SPP is defined and the dispersion relation of SPP on planner surface is given to investigate and understand the parameter effect and influence on the SPP. A literature review of THz plasmonics with an emphasis on the extraordinary transmission of THz SPP through subwavelength hole arrays fabricated on metal is presented in Section 4.4. This chapter will present and establish the motivation behind this work as well as our SPR design.

4.2. What is the Surface Plasmon Polarization (SPP)?
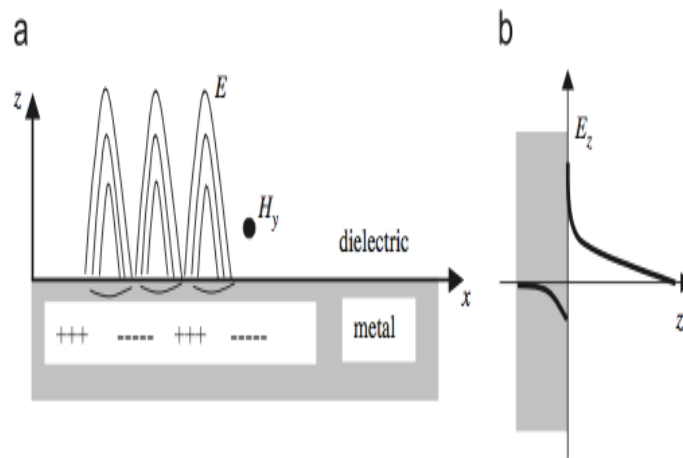
Figure 4.1. (a) Shows the electric and magnetic field oscillation on the interface between metal and dielectric media. (b) The penetration depth on both medias depending on the dielectric of the metal and the dialectic media as well as the resonant frequencies of SP waves on the conductor and the EM waves traveling in the dielectric media [25].

Figure 1 illustrates SPP propagating on metal-dielectric interface with different permittivity. Surface plasmon polarizations are an inhomogeneous combination of transverse and longitudinal waves stemming from free electrons on the interface between a conductor/dielectric media with unique geometries simulated from the electromagnetic field which are coupled by using different means [1, 5, 9, 13-15, 25, 41]. However, the excitation of the SPP depends on the polarization of the EM waves and the incident direction, which is usually perpendicular to the metal surface with p-polarized wave due to the z-direction of the SPP oscillation [1, 13, 14, 41]. SPP propagates non-radiatively along the x-direction. The lack of a momentum match between the

two wave numbers results in a non-direct transformation between light and SPP along the interface [1, 5, 25]. Various methods have been used to match the momentum between the EM waves and SPP waves, including an aperture excitation approach and a grating technique, thereby achieving the confinement [see Figures 2 and 3] [1, 25]. This confinement between the SP waves and the incident's electric field of the same frequency results in SPP waves carrying a high momentum that is greater than the EM waves with shorter wavelength [8, 13].
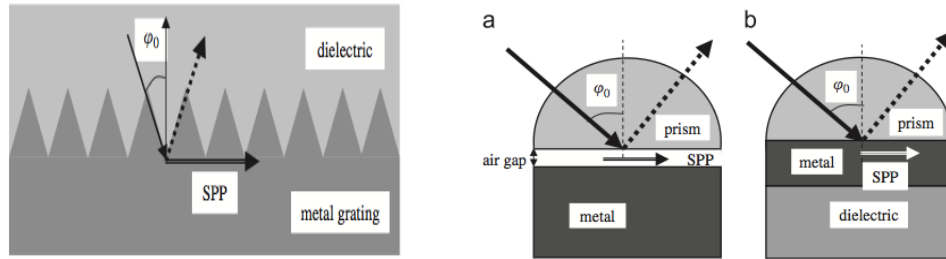
Figure 4.2 (on the right). Grating in the metal surface used for SP and EM waves momentum matching. Figure 4.3(on the left). (a) the Otto method, (b) the Kretschmann method for momentum matching between SP and EM waves [25].

4.2.1. Dispersion Relation of SPP at Planer Surface:

The physical principles of EM SPP on metal-dielectric interface have been explained by Maxwell equations through applying the electromagnetic boundary condition and using Drude model, as explained in Chapter 3, to obtain the dispersion relation of the SPP propagating on metal/dielectric interface, which is based upon two factors [1, 5]:

First, the real parts in the permittivity of the two medias in which the SPP form and propagate must have an opposite sign. This is the case in the metal/dielectric at the optical frequencies as indicated in the following equation [25]:

$$\frac{k_{zd}}{\varepsilon_d} = -\frac{k_{zm}}{\varepsilon_m} \qquad (1)$$

Where k_{zd} and k_{zm}, and ε_d and ε_m are the real wave vector in the z direction describing the surface mode of the EM SPP wave, and the real permittivity of the dielectric and the metal medium, respectively [1, 25]. In order for this equation to be

valid, the $|\varepsilon_m| > \varepsilon_d$ has to satisfied to form SPP [48]. The continuity for the in-plane condition is applied and the wave number calculated from Maxwell equations are considered to obtain the wave number of the SPP wave as given by the following [1, 25]:

$$k_{spp} = \frac{\omega}{c}\sqrt{\frac{\varepsilon_d\varepsilon_m}{(\varepsilon_d+\varepsilon_m)}} \qquad (2)$$

From this equation the wavelength of the SPP can be acquired by [25]:

$$\lambda_{spp} = \frac{2\pi}{k_{spp}} = \frac{2\pi c}{\omega}\sqrt{\frac{(\varepsilon_d+\varepsilon_m)}{\varepsilon_d\varepsilon_m}} \qquad (3)$$

It can be established that the ratio between the SPP wavelength and the EM wavelength traveling in the dielectric medium $\frac{\lambda_{spp}}{\lambda_0}$, $where$ $\lambda_0 = \frac{(\frac{2\pi c}{\omega})}{\sqrt{\varepsilon_d}}$, has to be less than one for subwavelength optics [25].

Second, for determining the penetration depth and the propagation length, it is mandatory to devote effort and time into selecting the appropriate metal, surface configuration, coupling technique, and EM wavelength required to form and implement SPP by the following equation[1, 5, 9, 13, 14]:

$$k_{zd} = i\sqrt{\gamma(\gamma + 2k_0)} = k_{zd}^{''} \qquad (4)$$

Where $k_{zd}^{''}$ is the imaginary wavenumber components in the perpendicular direction inside the dielectric [1]. The symbol $\gamma = k_x - k$ is the confinement parameter of the SPP to the interface, which will be strong if $\gamma > 0$, meaning that the real wave number of the free-electron (k_x) is larger than the wave number of the EM incident wave [1]. Practically, considering Fano mode, the metal permittivity has to be negative with its value larger than the dielectric permittivity to achieve high field confinement [49]. k_0 is utilized to describe the dispersion relation of the SPP under the assumption of low loss metal. It is defined as $k_0 = \frac{w}{c_0}n_d$, where n_d is the refractive index of the dielectric [1].

70

Thus, SPP wave is an evanescent wave, or a near field wave that suffers from exponential decay perpendicularly in both medias when SPP reaches its maximum. This has been defined as the penetration depth L_p or the skin depth of metal at which the amplitude of the SPP declines by a factor of $1/e$ due to absorption from metal and scattering [see Figure 4] [1, 5, 7, 8, 13]. This leads to the highly localized wave being confined near the conductor surface, which is very attractive for sensing applications [5]. The confinement can be adjusted by altering the conductivity of the substrate [5, 9].
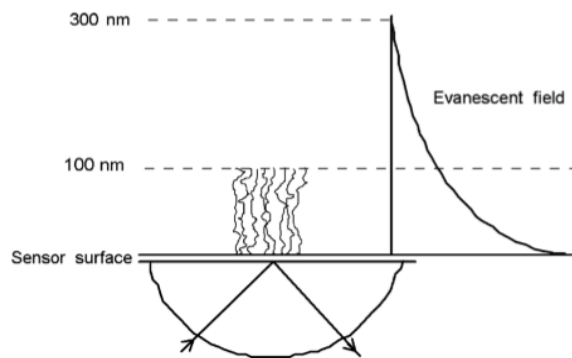
Figure 4.4. Decaying length of SPP waves into the dialectic medium illustrating the limited range of SPP sensitivity to around 300 nm above the conductor surface [26].

To summarize, in order for the SPP confinement to occur efficiently and be applicable, the EM wave traveling in the space has to have an effective index less than that of the free-electrons wave on the conductor surface. As well, the propagating distance of SPP has to be suitable for this use. For example, silver has been utilized in photonic circuits due to its low loss at the optical frequency, which results in long propagation distance for SPP [1-8, 48]. When considering the opposite situation between the permittivity of the EM in the dielectric media and the SP on the conductor, weak confinement of the SPP to the interface has been reported with long propagation distance that is the case with THz wave and noble metals [1-9]. Therefore, three parameters have been used to investigate and manipulate the SPP: wavelength of the SPP, propagation length, and decay length [1, 5, 25].

Sensing and detection capabilities of THz radiation to thin film can be significantly improved by employing the SPP concept due to its tighter confinement

of the high field near a metal-dielectric interface [21]. Thus, to implement the SPP concept in the THz frequencies, the permittivity of the dielectric must be increased or materials must be used with low permittivity, if the concept of planar surface is desired [1, 5]. Coating or depositing a dielectric film on top of noble metal enables lowering the permittivity of the dielectric media [1, 5, 9]. The other technique which is based on using materials with low permittivity has been accomplished through using semiconductors such as In-Sb, since utilizing a semiconductor as a surface of the SP offers the possibility of tuning the permittivity of the material to a certain frequency by changing the deposition density [1, 5, 9].

A further approach reporting extraordinary THz transmission is performed by engineering a surface plasmon at almost any frequency, as "metals are nearly perfect conductors from zero frequency up to the threshold of the terahertz regime"; this is known in the THz SPP field by the sub-wavelength metallic hole arrays approach [5, 14].

4.3. Literature Overview of THz Plasmons:
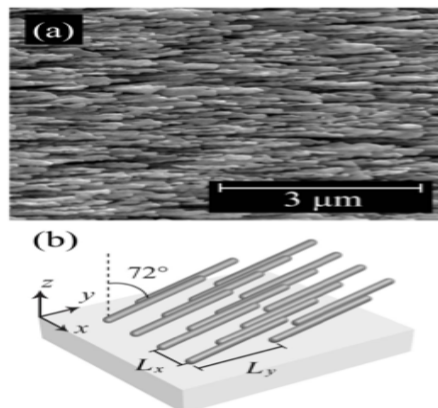
Figure 4.5. (a) SEM image for the silver nanorods, (b) Dimensions of these silver nanorods used by Cao et al. [27]

Owing to the SPP features and the well-developed characteristics of the SPP, THz plasmonics are being developed very quickly, including near field THz imaging and spectroscopy, THz photomixing source, photoconductive THz source and photoconductive THz detector, nanoscale devices, and THz thin film spectroscopy [3, 16, 23, 24]. The plasmon concept has been applied in THz sources and detectors to

increase THz radiation powers from a plasmonic PC generator 50 times higher compared with a similar PC generator with non-plasmonic contact electrodes, as well as 30 times higher THz detection sensitivities from a plasmonic PC detector compared with a similar PC detector with non-plasmonic contact electrodes [24].

.
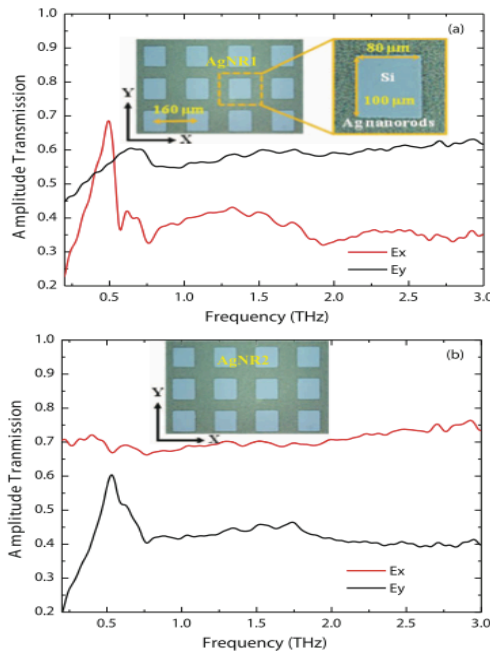
Figure 4.6. Illustrate the SPR device fabricated on the silver nanorods and the direction of the pattern of the SPR structure whether in the long side of the rectangular or the short axis with respect to the Ag nanorods direction [27].

THz plasmonic nano-structure materials, like carbon nanotube and THz-scattering near-field optical microscopy, have demonstrated potential in working as a waveguide of THz frequencies. Many applications will benefit, including biochemical sensing, nano-antenna, and DNA chips [26, 27]. For example, carbon nanotube characteristics, including small junction areas, high electron mobilities, and low estimated capacities, make them more attractive than solid-state components, such as metal waveguide [28]. THz nanotechnology-based techniques are being utilized to overcome a number of challenges in the THz field, such as improving the low performance of the THz sources, and increasing the resolution of THz imaging [28]. Recently, Cao et al. have demonstrated a novel approach in which silver nanorodes are utilized as a substrate to fabricate the subwavelength

structures [see Figures 5 and 6 in 29] [29]. This approach can serve as THz polarization filtering, switching, tuning, sensing, and narrowband filtering devices because the polarization-dependent extraordinary transmission of THz pulse through the subwavelength structures is supported by the anisotropic nanoscale surface morphology of the silver nanorodes, thereby increasing the material anisotropy at THz frequencies 3 orders of magnitude longer than the nanorod length scale [29].

THz plasmonics and metamaterials are examples of other areas being utilized to improve the applications in THz technology, such as SPP THz sensing because of the ability of designing metamaterials to respond to THz radiation by using methods that cannot occur in natural materials [25, 29].
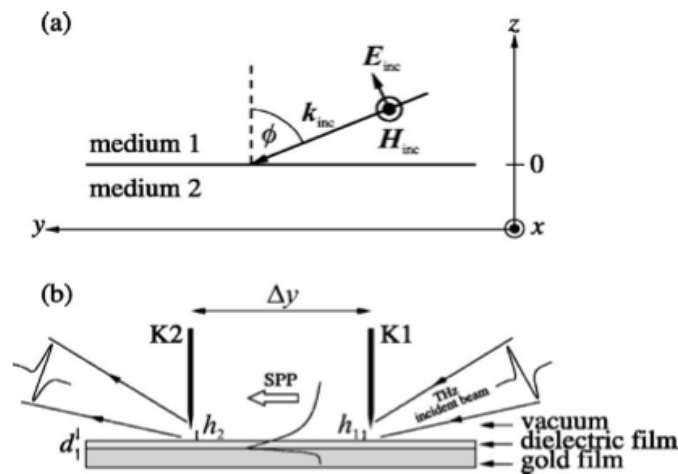
Figure 4.7. (a) SPP wave coupling geometry, (b) Gold film covered with a dielectric film [28].

Before embarking in a concise description of approaches utilized to confine THz ray into subwavelength structure and strengthen the confinement of SPP in THz regime, it is interesting to differentiate between surface waves and surface plasmon polarization [5, 16].

Plasmonic surface waves are a configuration of EM surface waves, such as Zenneck waves or Sommerfeld waves (known as surface waves) [5, 17]. Surface waves, which were discovered in 1907, are radio waves able to propagate into the surface

of the ground or the sea [17]. Later, surface waves were implanted in localized radiation application, including Zenneck waves on a flat metal surface and the Sommerfeld wave on a single metal wire [16, 17, 48]. Surface waves differ from SPP waves in that Zenneck waves are formed between two dielectric interface media, while the permittivity has to carry different signs for both medias where the plasmonic surface waves form [16, 17, 48]. Surface waves at THz frequencies are being explored as SPP mode, if studied conducted on a noble metal surface in some works in the literature, while other studies consider this to be two different phenomena [5, 16, 17, 26].

As mentioned above, three approaches in the literature have been utilized for thin film spectroscopy: dielectric film coated on a noble metal, the use of low permittivity substrate, and the sub-wavelength metallic hole arrays [1, 5, 14, 15].
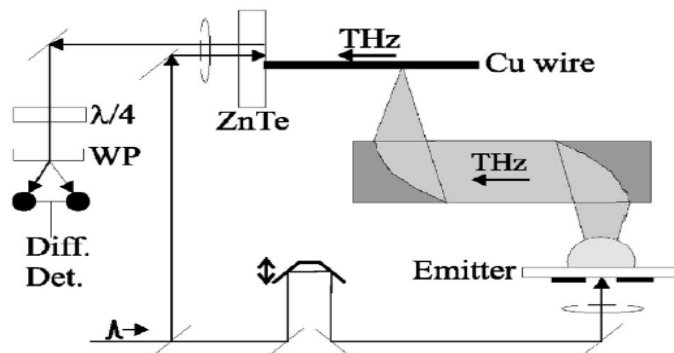
Figure 4.8. THz detector is fixed by the end of the metal wires [29].

The former technique is vividly illustrated in Figure 7 [19]. Two cyclotene films are presented "as an example of how the dielectric thin film used to increase the permittivity of the dielectric media" with thicknesses of 3.8 and 9 μm deposited on gold substrate have been successfully characterized [5]. To couple the THz pulse to the SP wave, two razor blades are fixed at specific heights from the dielectric film separated by a certain distance to form the in-coupling and out-coupling apertures [see Figure 7] [19]. This technique utilized in SPP technology to couple the EM wave with the SP wave is known as the aperture excitation approach [19]. Another technique using the same principle conceivably coats dielectric film on metal wires [18, 20]. Unlike the use of flat surface, such as in the above example, the use of metal

75

wires increases the sensitivity of spectroscopy measurements because wires do not spread out the THz SPP waves. This leads to a decrease in the frequency and an increase in the phase velocity and group velocity approaching the speed of light, thereby resulting in estimating an ability of sensing thin film with a few nanometers [18, 20]. Sharp needles from the same material of metal wires are attached to the metal wires to couple the THz pulse with SPP wave [18]. The THz detector is fixed by the end of the metal wires to detect the propagating THz SPP waves [see Figure 8] [18, 19]. Further information about the dispersion relation of THz SPP when utilizing this technique is available in Reference 19.

While high resistivity semiconductors are transparent to THz waves, highly doped semiconductors exhibit metal behaviour at THz frequencies, thus forming SPP resonance in terahertz regime [5, 15, 21, 22, 36]. As mentioned above, THz SPP on highly doped semiconductors including Indium antimonide (InSb), n-doped Si, and p-doped Si is another approach utilized in THz spectroscopy and imaging [5, 15, 21, 22, 36]. Rivas et al. have revealed the first demonstration of THz-TDS measurements of broadband SPP pulses propagating on complex structures including gratings or grooves [15]. The key behind the use of semiconductor substrate is the natural behaviour of a semiconductor at low frequencies as metals in the optical range, thereby making it possible to excite and propagate SPPs on semiconductor/dielectric interfaces at THz frequencies with the ability to change the permittivity and influence the strength of the confinement [5, 15, 25, 40, 47]. This leads to increasing the sensitivity of spectroscopy measurements by reducing the SPP group velocity [5, 15, 25, 40, 47]. The coupling techniques are also necessitated, in this approach, if the semiconductor surface is smooth, or contains grooves spreading in large areas [15]. Grating, holes, or apertures which have formed on semiconductor substrate have been used to investigate the impact of SPP at THz spectroscopy and imaging [5, 15, 21, 22]. Extraordinary transmission of THz pulse through subwavelength hole arrays on semiconductors, including n-type silicon and InSb, have been achieved by the resonant tunneling of SPP, which increases by increasing the size of the aperture, and reducing the thickness of the grating, to some extent [30, 40, 47]. Azad

76

et al. have shown that the efficiency of the extraordinary transmission is polarization-dependent; that is, the transmission efficiency maximum when the major axis of the aperture is perpendicular to the polarization of THz electric field E//x is due to the preservation of the input linear polarization for the surface plasmons when E//x [40]. Also, the amplitude of the transmission pulse is reduced when the dielectric permittivity of the area surrounding the Si increases, such as deposited thin film on the Si substrate, unlike what occurs on the metallic substrate [40]. However, for sensing thin film using the smooth semiconductor surface, a trade-off is expected to occur between increasing the interaction length and a reliable change between the reference and the sample signal due to the high propagation loss [5].

4.4. Terahertz Surface Plasmon Resonance (SPR) Near-Field Sensor:

4.4.1. Subwavelength Metallic Hole Arrays:

Extraordinary transmission of light through subwavelength hole arrays has attracted many areas of applications including optical data storage, near field microscopy, optical displays, and thin film sensing [5, 30, 34, 39]. The enhancement in the tunneled transmission light stemming from the coupling with SPP by the surface configurations has been explored through the waveguide theory and the grating theory of the frequency-selective characteristic of SPP resonances [30, 32, 34, 35, 36, 41, 42].

Ebbesen et al. have established the concept of extraordinary transmission of light through subwavelength hole arrays [38, 39, 42, 46]. The extraordinary transmission phenomena was observed for light tunneled through subwavelength aperture arrays fabricated on optically thick metal with efficiency higher than unity normalized to the fraction of the grating's surface occupied by the holes [36, 38, 42, 43]. This observation extends beyond what Bethe theoretically predicted as explained in the diffraction theory, which indicates that the transmission energy (T) of EM wave through an isolated circular hole in an optically thick metal film is determined by the diameter of the aperture (d) and the wavelength of the light (λ) by the following

77

relation [38, 39]:

$$T \propto (d/\lambda)^4 \qquad (5)$$

At THz frequencies, the extraordinary transmission through thin metallic hole arrays has been demonstrated through the excitation of SPP on the metal–dielectric interface confining the incident THz pulse around the holes, hence precluding THz pulse from easily passing and attenuating into the conductor [30, 32, 35, 38, 46]. This process is explained theoretically and experimentally by using THz-TDS to investigate and study the SPP properties at THz frequencies including the resonant transmission effects of hole shape, dielectric properties of materials, and thickness of the arrays [30, 35, 38, 43, 45]. In this approach, the periodic aperture arrays cause the coupling of THz pulse and SPP wave through scattering energy into a tangential diffractive component [36, 38, 45, 46].
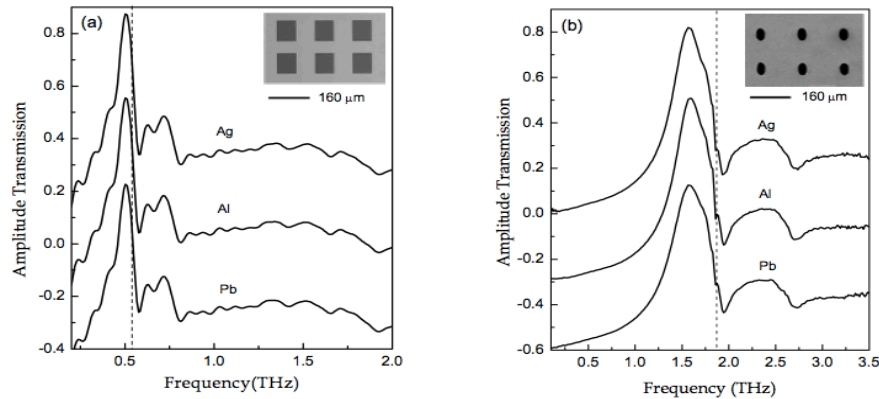
Figure 4.9. THz amplitude transmission in different materials depends on the shape of the metallic aperture arrays [30]. Also depends on the dielectric of the metal " metal with a higher ratio between real and imaginary parts of the metal permittivity endows a higher amplitude transmission, such as 87%, 85%, and 82% for Ag, Al, and Pd consecutively [30].

The extraordinary transmission occurrence of THz SPP has been observed on metal/dielectric interface with a ratio of the real and imaginary part of the metal permittivity more than unity $\frac{-\varepsilon_{rm}}{\varepsilon_{im}} \gg 1$, which exhibits a discrepancy against what has been proven about SPP at THz frequency [31, 36, 38, 46]. Essentially, the configuration of the surface, which is known as surface plasmon resonance device, leads to a rise in the effective dielectric constant and establishes the SPP resonance even with the

ratio $\frac{-\varepsilon_{rm}}{\varepsilon_{im}} \gg 1$ [21, 36, 38, 50]. A variety of metals have been reported as offering extraordinary transmission at THz frequency including lead (Pd), silver (Ag), and aluminum (Al) [33, 36, 38]. The dielectric function of the applied metal influences the extraordinary transmission amplitude of THz SPP wave through the hole arrays [see Figure 9] [36, 38]. The experimental results agree with what is expected theoretically in which the metal with a higher ratio between real and imaginary parts in the permittivity endows a higher amplitude transmission, such as 87%, 85%, and 82% for Ag, Al, and Pd consecutively [36, 38]. When this metal layer has been deposited on thick high resistivity Si, or the thick high resistivity Si has been placed on the back of the wafer carrying the metal layer, the thickness ranges from 2mm to 10 mm, clean observations of plasmon dynamics are obtained through eliminating the backside reflection [32, 36, 42].
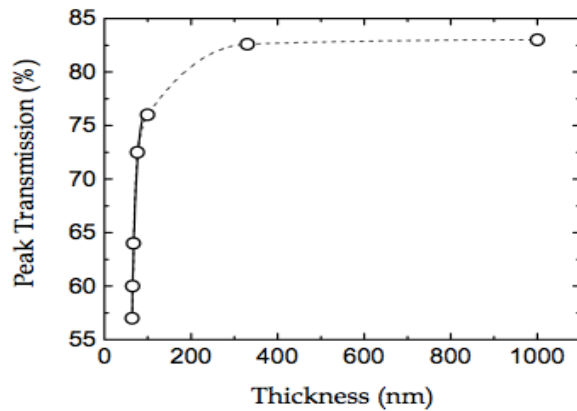
Figure 4.10. The dependence of THz transmission amplitude on the thickness of the metal film, the metal here is Pd [30].

The thickness effect of the metal on the transmission amplitude at THz frequencies has been investigated [see Figure 10] [36, 38]. The product of this study can be explained as transmission efficiencies measure above 90% of their maximum amplitude transmission when the metal thickness is equal to one-third of the skin depth [36, 38]. The skin depth has been defined in section 4.2.1 as the penetration depth at which the amplitude of the SPP declines by a factor of 1/e [25, 36 38]. Metal thickness above or under the skin depth reveals a reduction in the transmission amplitude of THz pulse [36]. For the latter case, no SPP enhancement is measured until

the thickness of the metal increases to a critical thickness in which the effect of SPP resonant on the THz transmission amplitude starts to be measured [36, 38, 43]. In the former situation, the transmission amplitude of THz pulse is alleviated due to the attenuation from long tunneling distance [36, 38].

The shape, size, and period of the hole arrays at THz frequencies directly impact the SPP resonant mode and the amplitude of the transmission [33, 35, 36, 38, 41, 42]. Figure 9 illustrates this dependence. Rectangular aperture shape expresses strong polarization dependence, yet circular hole, or any other aperture with fourfold symmetry is not polarization dependent [35, 36]. Various resonant transmission amplitudes and line shapes regarding the aperture shape result in a higher phase change observed from the rectangular compared to circular hole because the rectangular shape preserves the input linear polarization, yet the circular hole does not [35, 36, 42, 43]. The size of the hole arrays affects the transmission amplitude of THz SPP; in other words, the larger the size of the hole the higher the transmission amplitude of THz SPP, yet until it reaches a critical size, the transmission amplitude decreases rapidly [33].

4.4.2. Bull's eye Structure on Metallic Film:
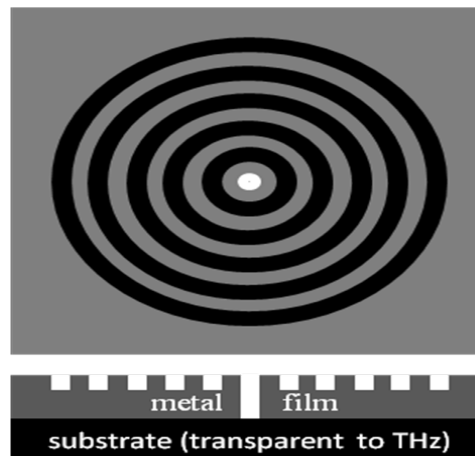
Figure 4.11. Schematic diagram of the Bull's eye structure.

Bull's eye structure is another configuration of the SPR device consisting of a single hole surrounded by concentric periodic annular corrugation [see Figure 11]

31, 37, 38, 44.

Similar to the above structure, this configuration has a history in optical frequencies before implanting in THz frequencies, and it also exhibits extraordinary transmission of THz SPP [31, 38, 44]. The extraordinary transmission of THz SPP can be achieved by a certain distance between the annual rings and the position of the bull's eye [31, 37, 38]. Further observation is established in which the extraordinary transmission of THz SPP is suppressed by changing the distance between the rings and the aperture [31, 38]. Two phenomena are responsible for either extraordinary transmission or transmission suppression: a single cycle pulse "non-resonant transmission" and a damped oscillation "resonant transmission" [31, 38]. The former phenomenon leads to the regular transmission of the THz through the hole [31, 38]. The latter phenomenon describes the interaction of the THz pulse with the annual rings causing the extraordinary transmission of THz SPP [31, 38].

4.4.3. Motivation of This Thesis Work:

It can be deduced that THz SPP sensors are indispensable due to their high sensitivity among other sensors, particularly in biology [25]. In other words, implementing THz SPP in thin film sensing has great potential for industrial applications because the two dimensional nature of SPPs and the strong electromagnetic field at the interface [15, 19] with the THz natural reaction with the material "Chapter 3" provides reliable measurements of thin film spectroscopy including optical and dielectric constants, film thickness, and inhomogeneities at interfaces with high precision. This motivates the investigation of the characteristics such as purity of thin organic film including PMMA and those used in organic light emitting diode (OLED) through THz SPR devices.

4.4.4. Experimental Setup of Transmission Mode THz-Time-Domain Spectroscopy:

Similar to the experimental set up for transmission mode photoconductive (PC) switches with large aperture as explained in Chapter 2, we employ THz-TDS to

experimentally measure the transmission magnitude and phase change of THz pulses through thin metallic films patterned with subwavelength hole arrays on silicon wafer. The data acquisition of the THz pulses is performed using LabView software and Lock-in amplifier. The silicon wafer was 2" in diameter and placed using a special sample holder at focus of the THz beam.

For THz spectrum measurement, the SPR device on the 2" Si wafer with and without thin (PMMA) film on it is placed at the focus of the THz beam in transmission THz-TDS, where the spectrum is obtained from the Fourier-transformed sample and reference THz pulses. The transmission is obtained from the ratio between the sample spectrum and reference spectrum. The SPR device contains 2D periodic circular or square hole array in 500 nm Al on an 5 mm- thick intrinsic silicon, and was fabricated by photolithography and wet etching. We then measured SPR device that has a period of 320 μm and square holes of 150 μm side length.

4.4.5. SPR Devices Design and Simulation:

The fabricated metallic array of holes with diameter D and period P is shown in Figure 12.
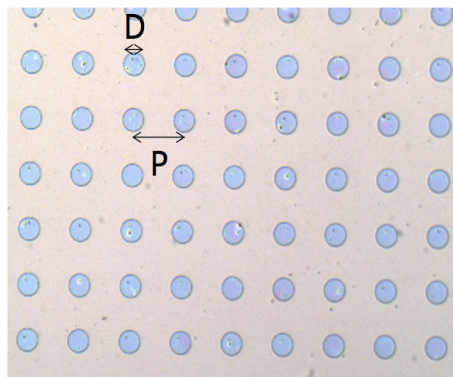
Figure 4.12. The fabricated array of metallic holes with diameter D and period P.

We designed and fabricated three SPR structures. One SPR structure is shown in Figure 13 and it is fabricated on 500 μm quartz wafer and is an array of circular holes with diameter of 100 μm and period of 200 μm and 1.57 μm layer of PMMA on

the structure. The second one is fabricated on 5 mm thick high resistive silicon to avoid reflection from the substrate and thus allowing longer THz scan using THz-TDS [see Figure 13]. To avoid overlap with water absorption lines, the optimal SPR device design has a period of 320 μm and square holes of 150 μm side length.
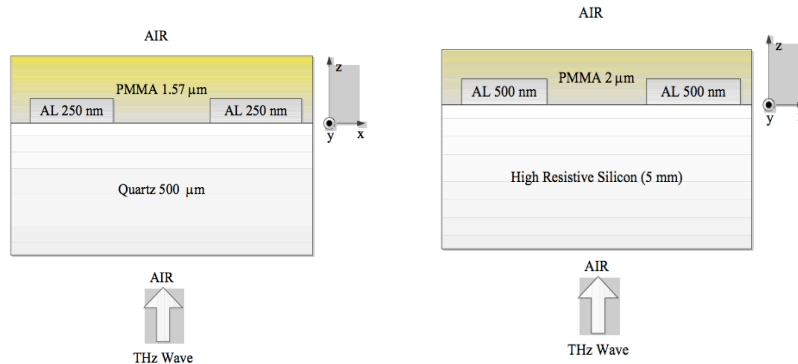
Figure 4.13 on the left. The SPR structure to simulate using HFSS to fin d the SPR frequencies of an array of metallic holes on 500 μm of quartz and thin film layer of 1.57 μm PMMA on it. For the simulation, the refractive index of quartz used was n_{quartz} = 1.96 and for PMMA n_{PMMA} = 1.436 based on terahertz transmission measurement. The SPR structure considered here is an array of circular holes with diameter of 100 μm and period of 200 μm and layer of PMMA on the structure. The simulated SPR resonance frequency for Metal/PMMA-Air interface mode (0,1) is 1.4878 THz. On the right. The SPR periodic structure on high resistive silicon with thickness of 5 mm for THz-TDS measurement

The third SPR device, the Bull's eye structure is fabricated using our proposed methods. In the first method (Figure 14), we first pattern the structure in a thick (tens of μm) photo-resist SU-8 by photolithography. Because SU-8 is transparent to terahertz, we will coat an aluminum film of 0.5-1 μm thickness (opaque to terahertz) on it by sputter deposition that coats the SU-8 structure sidewall as well. Next, the hole in the center will be patterned by a second photolithography step and wet etching of aluminum (critical dimension CD control is not an issue since Al here is very thin compared to the aperture size). In the second method, lithography transfers the bull's eye structure into the 300 nm thick Al film sputtered into 200 μm thick Si wafer. Instead of using thick Si wafer in order of 5 mm thickness, a very thin wafer will be used, with the "eye" structure etched through the wafer using deep silicon etching by RIE. The cost of using the expensive thick Si wafer is reduced in applying this technique by removing the complicity in the fabrication processes. Then the SU-8 ring structure is patterned by a second photolithography

step and coted with 0.6 μm Al film using sputtering technique.

4.4.6. Fabricating SPR Devices:

Fabricating subwavelength metallic hole arrays at THz frequencies is more amenable and easier than fabricating subwavelength metallic hole arrays at optical and microwave frequencies, which necessitate the use of e-beam lithography or focused ion-beam (for subwavelength optical devices) and mechanical techniques including printed circuit board milling (for subwavelength microwave devices) [34, 38, 39]. At THz frequencies, the subwavelength metallic aperture arrays are fabricated through traditional micro-fabrications techniques, such as thin film deposition approaches, standard photolithography, as well as wet and dry etching techniques [38, 42, 45].
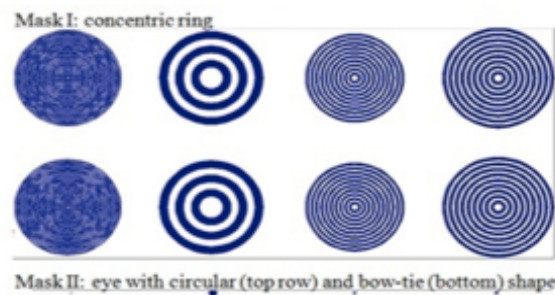
Figure 4.14. Mask design for the Bull's eye structure.

The fabrication of the bull's eye structure has been performed by conventional chemical etching techniques into stainless steel foils to form the annular rings and milling of the aperture on the centre of the rings' structure [31, 37, 44].

The fabrication has been performed in the Giga-to-Nanoelectronics Centre (G2N) at University of Waterloo.

4.4.6.a. SPR Device on 5 mm Quartz Wafer:

The SPR device on 500 μm quartz wafer was fabricated by depositing 250 nm Al film using electron beam physical vapor deposition (e-beam deposition) [66] [see Figure 15]. The deposition process took place under pressure of 10^{-6} Torr and the deposition rate was 2 angstrom/minute with e-beam power ranging from 15 to 16 W. Next, the Al film was treated using O_2 plasma to promote the adhesion of ARC to the Al surface.
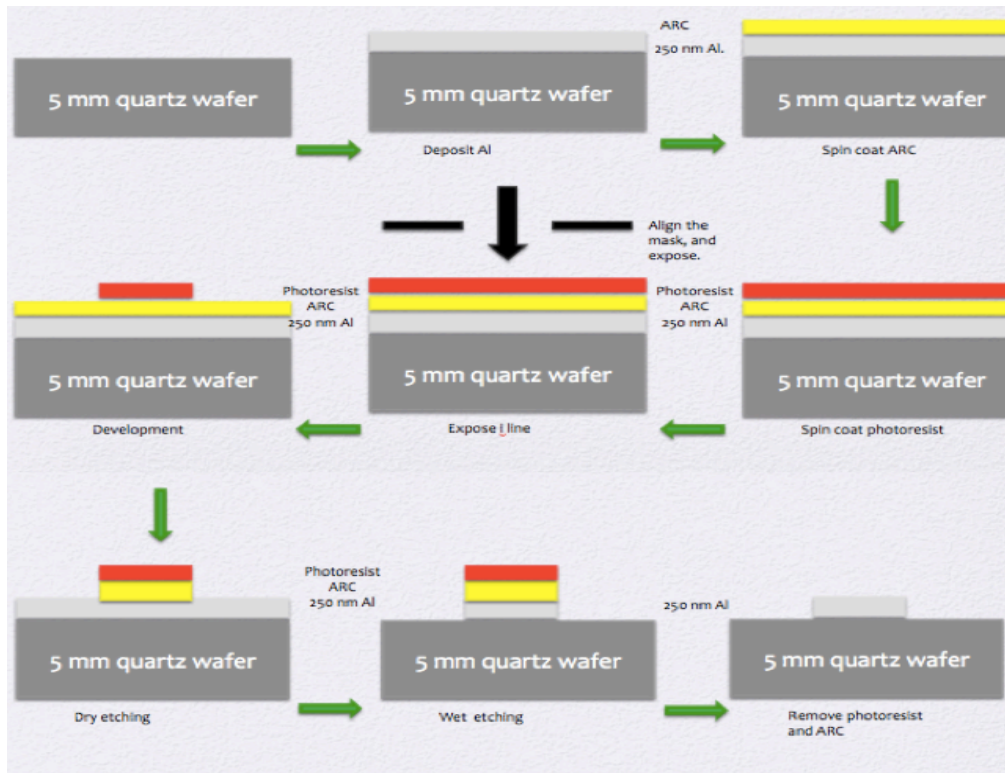
Figure 4.15. Schematic diagram of the fabrication steps.

Anti Reflection Coating (ARC) was spun on the Al film by utilizing the spin coating approach [50] as protection from the developer AZ 300MIF, which was used to develop a photoresist. Owing to the poor adhesion of the Al to quartz wafer, AZ 300 MIF attacked the Al film by peeling. Although the peeling of the Al film was slow, it was necessary to apply a protective layer due to the very thin Al layer. A high acceleration and spin speed in order of 2000 rpm for 40 sec was performed on the ARC film after dispensing the ARC into the whole wafer. Following the spin coating

process, the ARC layer was baked at a high temperature of 180 ^{0}C for two minutes to fasten the curing time for the ARC. The ARC thickness was 1 μm, which was found by applying the Dektak to determine the etching rate.

Negative photoresist nLOF 2035 was spun on the ARC layer by utilizing the same conditions of baking the photoresist for 1 minute at 110 ^{0}C to drive off the excess photoresist solvent in preparation for the UV exposure.

Exposing the negative photoresist was achieved by using the photolithography technique. The wafer was placed under the SPR mask, which was used to transfer the array of circular holes with a diameter of 100 μm and a period of 200 μm into the photoresist. The exposure time was 3 sec using the i line at contact mode.

Since the photoresist was negative, the photoresist was baked for 1 minute at 110 ^{0}C to form crosslinking in the exposed area, thus making it insoluble in the developer. This process, which is known as Post Exposure Baking (PEB), is usually applied for negative photoresist. Development was carried out using AZ 300MIF developer to transfer the SPR pattern to the photoresist.

Transferring the hole arrays into the Al layer was accomplished by the wet-etching technique after transferring the pattern into the ARC using dry etching for 2 minutes under the following conditions: 20 sccm O_2 flow, 20 W RF, and 20 mTorr. Phosphoric Acetic Nitric (PAN) etcher was prepared and used for Al etching. To accelerate the speed of etching, the PAN was heated to between 40 to 45 ^{0}C, resulting in etching of the Al layer in 1.5 minutes.

Finally, the wafer was dipped into AZ Kwik stripper at 60 ^{0}C for 2 minutes to take off the photoresist layer which was protecting the Al film. The ARC layer was etched away by using the RIE under the above conditions.

4.4.6.b. SPR on 5 mm Thick High Resistive Silicon:

Two SPR devices were fabricated on top of 5 mm thick high resistivity Si wafer. The SPP apertures arrays were patterned on 500 nm Al film and 1000 nm Al doping

ZnO (AZO) film [see Figure 16]. The fabrication processes for both materials were tantamount with each other, yet the deposition techniques and the solvents for the wet-etching step were different.

E-beam evaporation was utilized to deposit the Al film under the above conditions. The PECVD was used to deposit the AZO film using the following conditions: power 100w, pressure 2mTorr, Temp 250°C, and Ar gas for 1H.

Spin coating positive photoresist S1813 with 2000 rpm acceleration and spin speed for 40 sec was applied to both wafers which were then baked at 110 °C for 1 minute. Note that the ARC film was not coated on the Al film because the exposed areas would have been removed after developing, leading to the exposure of the Al areas, which were supposed to be etched away to transfer the patterns into the Al layer. Therefore, there was no need to protect these areas.
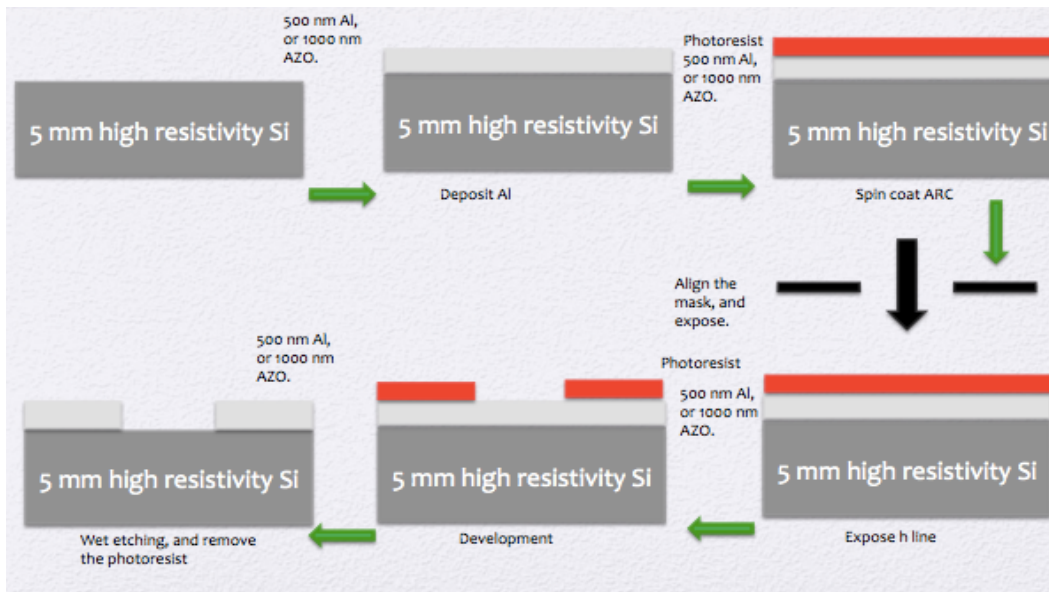
Figure 4.16. Schematic diagram of the fabrication steps.

After aligning a mask which was designed for a period of 320 μm with square holes of 150 μm side length, the h-line was used to transfer the patterns from the mask into the photoresist with 3.5 sec exposure time.

The same above developer was used to transfer the pattern into the photoresist

layer; the developer dissolved the exposed regions, while the unexposed areas remained to protect the Al and AZO film during the wet etching process. The Al was etched as mentioned above by PAN. HCL solution was prepared and used to etch the AZO film. Etching the AZO film took 2 minutes.

   Finally, the remaining photoresist used as an etching mask was removed by acetone.

 4.4.6.c. Bull's Eye Structure SPR:
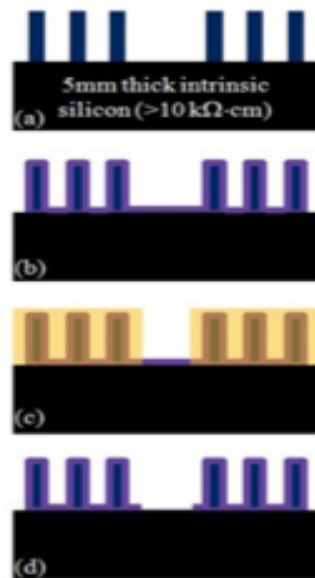
Figure 4.17. Schematic diagram of the fabrication steps.

   It was challenging to fabricate the bull's eye structure lithographically on 600-nm-thick aluminum film deposited on silicon substrate, which to the best of the authors' knowledge has not been done before. Difficulties were imposed on spin coating the photoresist such as S1813 onto a surface containing grating with height of approximately 25 µm. Various attempts were performed with the aim of uniformly spin coating the S1813 for a second exposure step. Before describing the attempts at resolving this issue, the fabrication processes should be introduced [see Figure 16].

Negative photoresist SU-8 2015 [51, 52] was applied into 5 mm high resistivity Si wafer. The spin coating, baking, exposure, and PEB and development conditions are illustrated on Table 1. Tackling SU-8 2015 photoresist was challenging due to three reasons: first, the baking and PEB temperature had to be precisely 95 ^{0}C during the entire baking time; second, the exposure time had to be sufficient, otherwise the patterns would fall off during the development time; third, SU-8 2015 was difficult to remove once it was patterned into the substrate, if any errors occurred during the device fabrication. However, SU-8 2015 provided a thick high aspect ratio structure in the order of 10:1 exposed by the inexpensive conventional photolithography. Since SU-8 2015 adheres well to the Si substrate in order of 53 Mpa [51, 52], and it is transparent to THz frequency, it has been chosen for use as a structure layer in the bull's eye device. A test pattern was run to examine the resolution of SU-8 2015 resist.

THE EXPERIMENT CONDITION		
1	Coat SU 8 -15 for 40 sec at 2000 rpm, bake for 5mint at 95 C, exposure for 4 sec, PEB for 5 mints at 95 C, development for 5mint.	✖
2	Coat SU 8 -15 for 40 sec at 2000 rpm, bake for 5mint at 95 C, exposure for 6 sec, PEB for 5 mints at 95 C, development for 5 mint.	✖
3	Coat SU 8 -15 for 40 sec at 2000 rpm, bake for 5mint at 95 C, exposure for 8 sec, PEB for 5 mints at 95 C, development for 5 mint.	WORK

Table 4.1. SU-8 2015 spin coating, baking, exposure, PEB, and development conditions.

600 nm Al film was sputtered at deposition rate 6.74nm/minute on top of the SU-8 2015 ring structures utilizing DC magnetron sputter deposition technique, which is classified under a physical vapor deposition approach. The deposition conditions were performed under low pressure 5.7 E-7 mTorr to alleviate the incorporation of argon (Ar) atoms into the Al film, acting as nucleation sites for the grains resulting in stress, small grain size, and high electric resistivity [66]. Next, bull's eye structures were supposed to be lithography transferred to Al layer in the middle of the ring structures. However, due to the annual ring structures, protecting the Al film from the wet etching was not achieved. In other words, the photoresist which was used as

an etching mask did not prevent the Al layer from being etched from the SU-8 2015 structures. To achieve this protection, the following attempts were utilized.

First, the S1815 photoresist was spin coated on the Al film covering the annual ring structure by:

1- O_2 treatment to the Al layer was followed by spin coating the S1815 to enhance the adhesion; this spin coating was performed under low speed in order of 500 rpm for 40 sec.
2- After O_2 treatment to the surface, the photoresist S1815 was dispensed on one side of the wafer and allowed to flow towards the other side by tilting the wafer. The S1815 was left on the wafer for a few seconds and spun using different speeds of 1000, 700, and 500 rpm for 30 sec.
3- Exposing the S1815 was performed directly after dispensing the S1815 onto the treated surface with O_2 plasma without spinning.

Bull's eye structures were lithographically fabricated on Al film between the ring structures. These attempts were **unsuccessful** because the Al covering the ring structures were etched away following PAN etching.

Second, planarizing the surface of the annular ring configurations was proposed to resolve the above issue. This was achieved by preparing a thick layer of PMMA dissolved in chlorobenzene and spinning it on the annular ring structures. Metalizing of the PMMA surface was achieved by evaporating Cr or SiO_2 on the PMMA film, or coating UV nano-print resist, which was used as a robust surface of the bull's eye lithography. Covering the PMMA surface was implemented to transfer the bull's eye structure into the metal or the UV nano-print resist surface, PMMA, and then the Al surface. The SiO_2 and the UV nano-print resist were excluded because they did not work experimentally due to cracking of the SiO_2 and the UV nano-print resist during the curing steps for the S1815.

Planarizing the surface of the annular ring configurations with the PMMA/Cr was successfully achieved. Bull's eye structures were patterned into the 50 nm thick Cr

film and then transferred to the Cr layer through wet etching. Finally, RIE etching for PMMA and Al was carried out and the bull's eye structures surrounded by the annular ring configurations with height of approximately 25 μm was acquired.

However, due to the long period of etching for the PMMA layer using O_2 gas, residues were observed in the Si substrate in the bull's eye regions. At first, it was supposed that the wet etching for the Cr was not performed properly. The fabrication steps were performed many times by using new Cr etcher solution, changing the etching time, or changing the deposition rate for the Cr, yet the same residues were observed. The literature was investigated in terms of transferring pattern through dry etching as the second assumption for generating these residues. It was noted that Tsuji et al. recorded similar observations while transferring nano-imprinted grating patterns to distribute feedback laser diodes (DFB LDs) [see Figures 17] [57]. These residues are formed in reaction to Si-containing resin and oxygen since O_2 is exclusively supplied as the etching gas [57]. Three methods have been proposed to resolve this problem; however, these were not utilized [57]. Instead, we considered changing the fabrication process for the aim of simplicity.
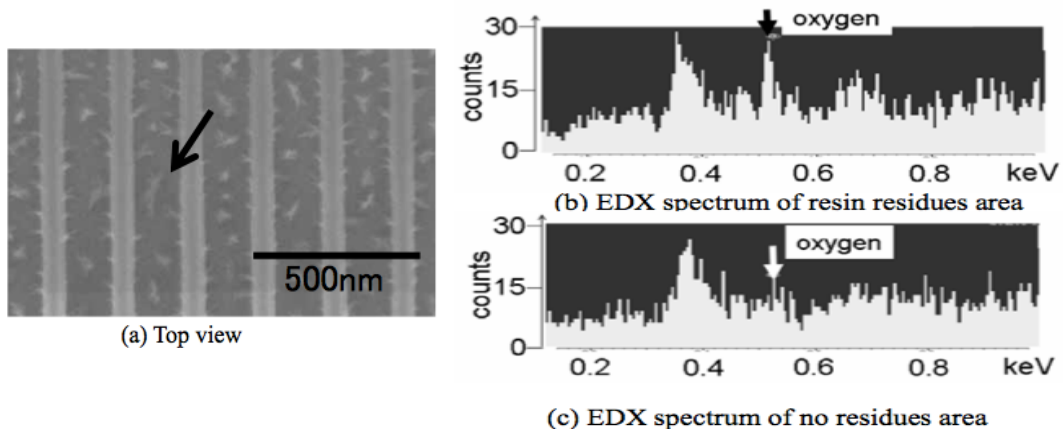
Figure 4.18. (a) SEM images for the resin residues, (b) and (c) EDX spectrum for the area with and without resin residues [31].

Third, lithography transfers the bull's eye structure into the 300 nm thick Al film sputtered into 200 μm thick Si wafer. Instead of using thick Si wafer in order of 5 mm thickness, a very thin wafer was used, with the "eye" structure etched through the wafer using deep silicon etching by reactive ion etching (RIE). The cost of using

the expensive thick Si wafer was reduced in applying this technique by using the thin Si wafer as well as the complicity in the fabrication processes was avoided.

Deep Si etching is well established in the literature through the application of two major techniques: cryogenic process and Bosch process [53-65]. The former technique has been performed by etching the Si anisotropy using SF_6 gas under low temperature [65]. Comparatively, the latter technique applies SF_6 gas with flowing Teflon C_4F_8 gas in a cycle to reduce the effect of the SF_6 natural isotropic etching through passivation of Si sidewalls [53, 62, 65]. The same result can be accomplished by mixing a specific percentage from O_2 gas with SF_6 [55, 56, 60-65]. Oxygen gas has been utilized to etch Si with SF_6 for two reasons: to increase the etching rate and to produce anisotropic fluoride based etching [55, 56, 60-65].

The deep Si etching was performed through bull's eye structures by implementing the Bosch approach. At the same time, a reliable RIE recipe was established by using a mixture of SF_6 and O_2 plasma as well as CF_4 and O_2 for etching nano-features [see Figure 18 and 19].
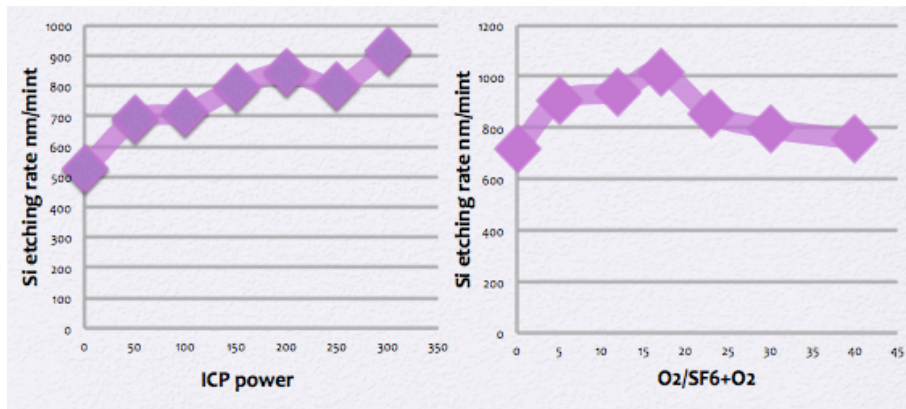
Figure 4.19. The effect of ICP (inductively coupled plasma) power on the Si etching rate (on the left). The Si etching rate increases with increase the ICP power because electromagnetic field generated by inductive coupling coil can sustain electron cycling movement in plasma for a long period, which has greatly increased ionization probability [63]. The influence of the addition of O_2 gas into the SF_6 plasma on the etching rate and the etching profile of Si [55, 56, 60-65]. The Si etching rate increases with the addition of 17 % O_2 to SF_6+O_2 plasma because O_2 ions create high voltage leading to increase the etching rate, yet increasing the concentration of O_2 gas behind 17% from the total gases concentration in the plasma yields in decreasing the etching rate of Si due to the dilution of F^* radicals in the plasma [55, 56, 60-65]. The RIE recipe was used: 200 V DC, 300 W ICP, 100 mTorr, 60 sccm SF_6 with varying the flow of O_2 gas: 0, 5, 12, 17, 23, 30, 40 sccm.

After etching approximately 135 μm with an etching rate of approximately 2.5 μm/minute, the wafer was etched from the backside to thinner the wafer and to open the bull's eye apertures to avoid losing the bull's eye features. The annual ring structures with 25 μm height was lithography patterned into the wafer which already contained the bull's eye holes and was metalized by sputtering 600 nm Al.
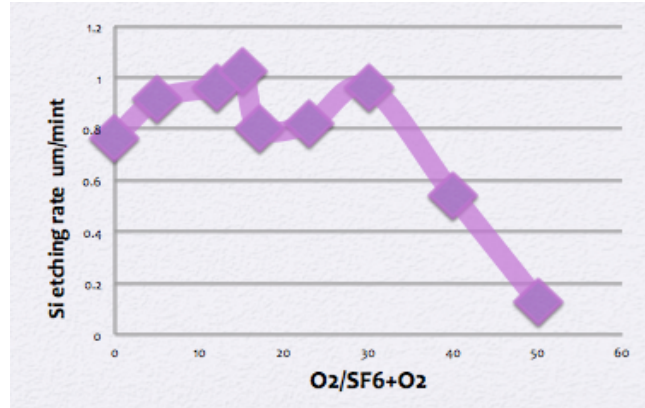
Figure 4.20. The effect of the addition of O_2 gas into the SF_6 plasma on the etching rate and the etching profile of Si. Here the RIE recipe was changed because we want to use less DC and ICP power: 150 V DC, 200 W ICP, 200 mTorr, 60 sccm SF_6, 0, 5, 12, 15, 17, 23, 30, 40, 50 sccm O_2.

4.4.7 Result and Discussion:

4.4.7.a. Theory of THz SPP on Al Substrate Patterned with Periodic Hole Arrays and Numerical Simulations of SPR Structure:
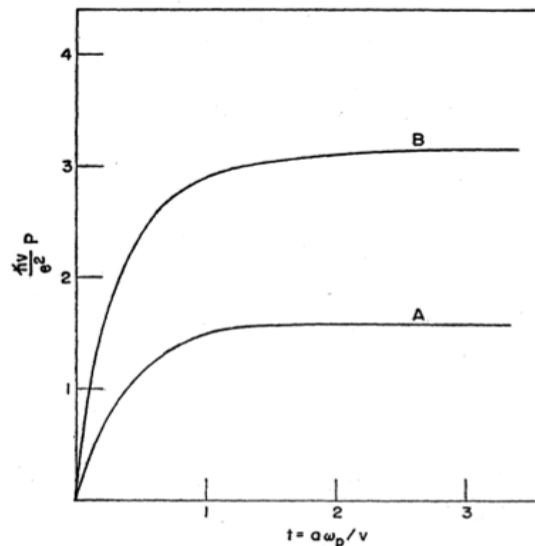
Figure 4.21. Curve A illustrates the reduction in the interaction probability of the EM waves and the

93

PS waves as the metal thickness goes down, Curve B depicts the probability for loss at low PS frequencies [32].

Regarding the equations 5 and 6 in chapter 3, the permittivity of the metal surface becomes positive if the frequency of the incident EM waves are at lower frequencies. Essentially, THz frequency and the SPP will not form under this condition [35, 38, 48, 49]. However, in 1957, Ritchie proved that the SPP propagation on a thin film of metal has resonant frequencies ranging from 0 to $\frac{\omega_{spp}}{\sqrt{2}}$ due to the small thickness of the metal film, resulting in broadening the frequencies range which can excite SPP waves [see Figure 20] [48]. The Al film has a very large permittivity at THz frequency, which is $\varepsilon_{Al} = -3.3 \times 10^4 + i\, 6.4 \times 10^5$; i is used to denote the imaginary part of the Al permittivity, which leads to the approximate wave number of the SPP in the terahertz region as [35, 42]:

$$k_{spp} = k_0\sqrt{\varepsilon_d} \quad (6)$$

The coupling condition of the SP in the periodic hole arrays has been counted as a form of 2-D grating yielding suitable tuning of the in-plane momentum to excite SPPs, even under normal wave incidence [35, 38, 42]:

$$k_{spp} = K_0 \pm mk_x \pm nk_y \quad (7)$$

Where K_0 is the component of the incident wave vector in the metallic (Al) film plane which is equal to 0 at normal incident, k_x and k_y are the array (grating) momentum wave vectors with ($|k_x| = |k_y| = 2\pi/P$), P is the period of metallic array, and m and n are the integers corresponding to the modes [35, 42]. This equation demonstrates that for a given SPP wave vector, the SP wave vector has to match the in-plane momentum wave vectors in order for the resonant coupling to take place [42].The wavelength of the SPP excited by the array is given by [35]:

$$\lambda_{resonance} = \frac{P}{\sqrt{m^2 + n^2}}\sqrt{\varepsilon_d} \quad (8)$$

As described in Chapter 3, two THz pulses propagating through air and sample, respectively, are recorded and their spectral amplitudes and phases are compared:

$$E_s(w)/E_r(w) = T(\omega)e^{j\varphi(\omega)}$$

The theoretical SPP resonance frequencies in the THz range are determined for the metal-silicon modes and metal-air modes with period of 320 μm. The calculated SPP (m, n) resonance frequencies for the metal/air interface and mode (0,±1) is 0.9375 THz, for the metal/silicon interface and mode (0, ±1) is 0.2743 THz, and for metal/silicon interface and mode (±1,±1) is 0.3879 THz. The measured refractive index of PMMA in the THz range is n = 1.4359.
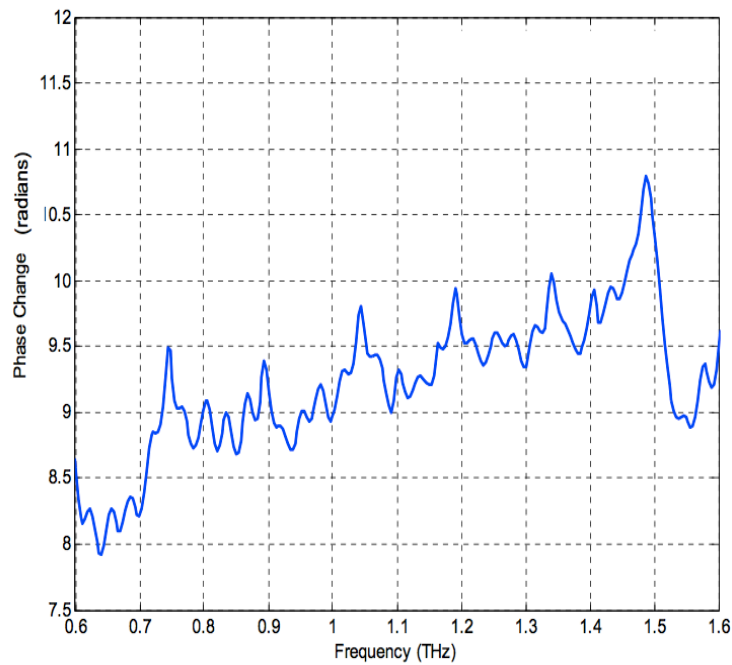
Figure 4.22. The high-resolution comparative phase change in radians for the SPR sensor on quartz wafer with PMMA layer on it. The hole array has diameter of 100 μm and period of 200 μm.

In order to determine the theoretical value of SP resonance with a thin layer of PMMA such as in Figure 13, we conducted Electromagnetic (EM) simulations to find the SP resonance frequencies and corresponding field distribution. We employed an eigenvalue solver in HFSS [67] to simulate the array of 100 μm diameter holes with period of 200 μm and a layer of 1.57 μm layer of PMMA. One unit cell of the periodic structure was modeled in HFSS and periodic boundary conditions were applied to the unit cell and measured refractive index of n_{PMMA}=1.436 used in the simulation. The theoretical value for the Metal/Air interface mode (0, ±1) for period of 200 μm

is 1.5 THz. As PMMA layer is deposited on it the SP resonance frequency shifts based on thickness and refractive index of PMMA. The measured Metal/PMMA-Air mode (0,±1) is 1.4870 THz where it is seen as a phase change sharp peak in Figure 21, and the HFSS simulated SP resonance frequency was 1.4878 THz. Figure 22 shows the Ez electric field distribution above the metallic array with layer of PMMA on it. The aluminum metallic layer is 250 nm. The measurement results match electromagnetic simulation results.
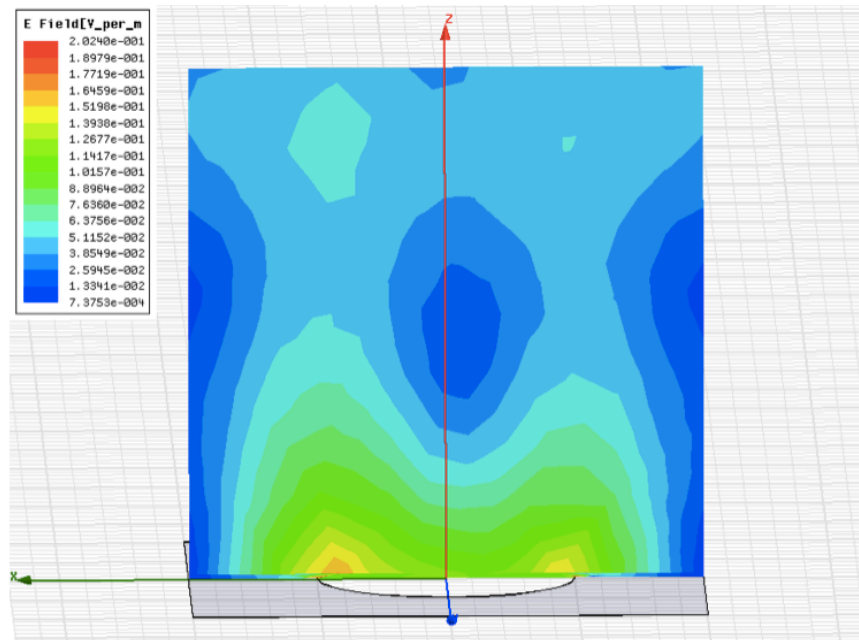
Figure 4.23. The *Ez* electric field at the metal/PMMA-air interface for mode (0, ±1) and circular hole with diameter of 100 μm and period of 200 μm on quartz substrate.

4.4.7.b. Experimental Results:

The theoretical SP resonance frequencies in the THz range are determined for the metal-silicon modes and metal-air modes with period of 320 μm. The calculated SP (m, n) resonance frequencies for the metal/air interface and mode (0,±1) is 0.9375 THz, for the metal/silicon interface and mode (0, ±1) is 0.2743 THz and for metal/silicon interface and mode (±1,±1) is 0.3879 THz.

Based on the sharp phase peaks centered on the SP resonance modes, the measured SP (m, n) for the case with and without PMMA are found from Figures 23 and 24. The measured SP resonance for the metal/air interface without PMMA layer is 0.9431 THz. The measured SP resonance frequency for Metal/PMMA-Air and mode (0, ±1) is 0.9211 THz with 2 µm layer of PMMA on SPR device. The measured SP resonance for the metal/silicon interface was 0.2765 THz for mode (0, ±1) and 0.3864 THz for mode (±1,±1). The measurement results confirmed the theoretical SPR frequencies for metal-silicon mode and demonstrate a shift to 0.9211 THz due to 2 µm of PMMA layer on the surface.
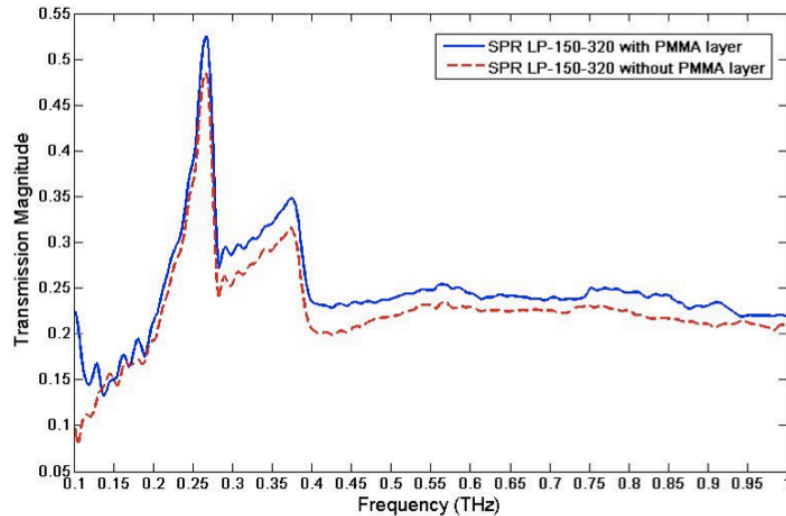
Figure 4.24. Spectra of the measured transmission magnitude of the signal pulse compared with the reference pulse for square 150 µm × 150 µm hole arrays with period of 320 µm. The transmission magnitude is shown without PMMA layer (dashed line) and with PMMA layer (solid line).

Table 2 shows the comparison of SPR frequencies for device with and without PMMA for square holes with length of 150 µm and period of 320 µm. The values were obtained from measured phase change peaks and transmission magnitude of Figure 23 and Figure 24.
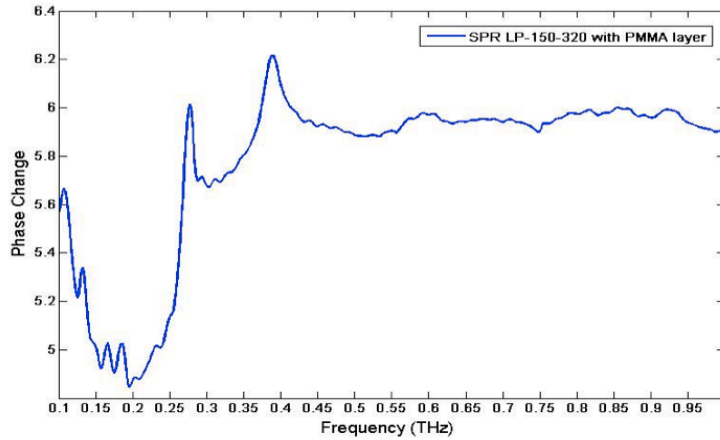
Figure 4.25. The comparative phase change in radians for the 150 μm ×150 μm square metallic hole arrays with period of 320 μm. The SP resonance frequencies occur at sharp peaks of the phase change.

Interface	Mode	Theory (THz)	Measured (THz)
Metal/Air	(0,1)	0.9375	0.9431
Metal/PMMA-Air	(0,1)		0.9211
Metal/Silicon	(0,1)	0.2743	0.2765
Metal/Silicon-PMMA	(0,1)	0.2743	0.2765
Metal/Silicon	(1,1)	0.3879	0.3864
Metal/Silicon-PMMA	(1,1)		0.390

*PMMA Thickness is 2 μm

Table 4.2. Comparison of SPR frequencies for device with and without PMMA for square hole array with side length of 150 μm and period of 320 μm.

4.5. Conclusion:

We present the use of Terahertz (THz) SPR near-field sensor to characterize materials such as PMMA and those used in organic light emitting diode (OLED). The SPR devices contain **either** 2D periodic circular or square hole array in 500 nm Al on an 5 mm-thick intrinsic silicon or quartz substrate, **or** the Bull's eye structure and was fabricated by photolithography and wet etching. For THz spectrum measurement, the SPR device with and without thin (PMMA) film on it is placed at the focus of the THz beam in transmission THz Time Domain Spectroscopy (TDS), where the spectrum is obtained from the Fourier-transformed sample and reference

THz pulses. To avoid overlap with water absorption lines, the optimal SPR device design has a period of 320 μm and square holes of 150 μm side length. The theoretical SPR frequencies in the THz range are determined for the metal-silicon modes and metal-air modes (0.9375 THz for mode (0, ±1)). The measurement results confirmed the theoretical SPR frequencies for metal-silicon mode and demonstrate a shift to 0.9211 THz due to 2 μm of PMMA layer on the surface.

Bibliography

References for Chapter 1:

1- Y-S Lee, Chapter 1 from Principles of Terahertz Science and Technology, New York Springer 978-0-387-09540-0 (2009).
2- X-C Zhang, and J. Xu, Terahertz Radiation Chapter 1 from Introduction to THz Wave Photonic, Springer Science and Business Media, LLC (2010).
3- D. Saeedkia. Handbook of Terahertz Technology for Imaging, Sensing, and Communications, Woodhead Publishing Series in Electronic and Optical Materials No. 34 (2013).
4- D. Liu, U. Pfeiffer, J. Grzyb and B. Gaucher, Advanced Millimeter-Wave Technologies-Antennas, Packaging and Circuits, Wiley (2009).
5- J. Dai, J. Zhang, W. Zhang, and D. Grischkowsky, Terahertz Time-Domain Spectroscopy Characterization of the Far-Infrared Absorption and Index of Refraction of High-Resistivity, Float-Zone Silicon, J. Opt. Soc. Am. B. No. 7 (2004).
6- A. K. Azad, J. F. Hara, R. Singh, H-T. Chen, and A. J. Taylor, A Review of Terahertz Plasmonics in Subwavelength Holes on Conducting Films, IEEE Journal (2013).
7- J. Han, A. K. Azad, M. Gong, X. Lu, and W. Zhanga, Coupling Between Surface Plasmons and Non-Resonant Transmission in Subwavelength Holes at Terahertz Frequencies, Applied Physics Letters 91, 071122(2007).
8- D. Saeedkia, Terahertz Photoconductive Antennas: Principles and Applications, TeTechS Inc, EuCAP (2011).
9- A. Stlianou, M. Talias, Nanotechnology-Supported THz Medical Imaging, Research.2-100.v1(2013).
10- C. Schmuttenmaer, Exploring Dynamics in the Far-Infrared with Terahertz Spectroscopy, Chem, Lett 104, 1759-1779 (2004).
11- D. Grischkowsky, S. Keiding, M. V. Exter, and Ch. Fattinger, Far-Infrared Time – Domain Spectroscopy with Terahertz Beams of Dielectrics and Semiconductors, Optical Society of America B journal (1990).
12- I. Pupeza, R. Wilk, and M. Koch, Highly Accurate Optical Material Parameter Determination with THz Time-Domain Spectroscopy, Optical Society of America (2007).
13- Applied Research & Photonics, Inc. http://arphotonics.net.
14- J. Saxler, J. G. Rivas, C. Janke, H. P. M. Pellemans, P. H. Bollvar, and H. Kurz, Time-Domain Measurements of Surface Plasmon Polaritons in the Terahertz Frequency Range, Physical Review B 69, 155427(2004).
15- X. W. Xin, L. Jing, and P. JiHong, THz-TDS Signal Analysis and Substance Identification via the Conformal Split, Information Sciences (2011).
16- P. N. Prasad, Nanophotonic Book, Wiley inter-since (2004).
17- J. Homola, Electromagnetic Theory of Surface Plasmons, Springer Ser Chem Sens Biosens (2006).
18- W. L. Barnes, A. Dereux, and T. W. Ebbesen, Review Articles, Surface Plasmon

Subwavelength Optics, Nature, VOL 424 (2003).

19- S. Pidishety, and N. l K. Viswanathan, Polarimetric Measurement of Optically Perturbed Surface Plasmonic Field, Optical Society of America (2013).

20- J. F. O'Hara, W. Withayachumnankul, I. Al-Naib, A Review on Thin-film Sensing with Terahertz Waves, Springer Science+Business Media, LLC (2012).

21- M. Liang, Z. Wu, L. Chen, L. Song, P. Ajayan, and H. Xin, Senior Member, IEEE, Terahertz Characterization of Single-Walled Carbon Nanotube and Graphene On-Substrate Thin Films, British Crown Copyright (2011).

22- M. Brucherseifer, M. Nagel, P. H. Bolivar, H. Kurz, and A. Bosserhoff et al. Label-Free Probing of the Binding State of DNA by Time-Domain Terahertz Sensing, Appl. Phys. Lett. 77, 4049 (2000).

23- A. G. Markelz, Terahertz Dielectric Sensitivity to Biomolecular Structure and Function, IEEE (2008).

24- K. R. Jha, and G. Singh, Terahertz Planar Antennas for Future Wireless Communication: A Technical Review, Infrared Physics & Technology (2013).

25- P. Shumyatsky, and R. R. Alfano, Journal of biomedical optics, http://biomedicaloptics.spiedigitallibrary.org, 16(3), 033001(2011).

26- A. G Davies, E H Linfield, and M B Johnston, The Development of Terahertz Sources and their Applications, Phys. Med. Biol. 47 3679–3689 (2002).

27- I. S. Gregory, W. R. Tribe, C. Baker, B. E. Cole, and M. J. Evans, et al, Continuous-Wave Terahertz System with a 60 dB Dynamic Range, Appl. Phys. Lett. 86, 204104 (2005).

28- M. Walther, B. M. Fischer, A. Ortner, A. Bitzer, A. Thoman, and H. Helm, Review: Chemical Sensing and Imaging with Pulsed Terahertz Radiation, Anal Bioanal Chem 397:1009–1017, Springer-Verlag (2010).

References for Chapter 2:

1- X-C Zhang, and J. Xu, Introduction to THz Wave Photonic Book, Springer Science and Business Media, LLC (2010).

2- D. Saeedkia. Handbook of Terahertz Technology for Imaging, Sensing, and Communications, Woodhead Publishing Series in Electronic and Optical Materials No. 34 (2013).

3- D. Liu, U. Pfeiffer, J. Grzyb, and B. Gaucher, Advanced Millimeter-Wave Technologies-Antennas, Packaging and Circuits, Wiley (2009).

4- Y-S Lee, Chapters 1, 3, and 4 from Principles of Terahertz Science and Technology, New York Springer 978-0-387-09540-0 (2009).

5- R. J. Hwu, and K. J. Linden, Terahertz and Gigahertz Electronics and Photonics V book, San Jose, (2006).

6- M. Bass, P. A. Franken, J. F. Ward, and G. Weinreich, Optical Rectification, Physical Review Letters (1962).

7- Chemical Rubber Corporation, Handbook of Chemistry and Physics, 80th edition, (1999).

8- V. Pacebutas, A. Biclūnas, S. Balakauskas, A. Krotkus, G. Andriukaitis, D. Lorenc, A. Pugžlys, and A. Baltuška, Terahertz Time-Domain Spectroscopy System Based on Femtosecond Yb:fiber Laser and GaBiAs Photoconducting Components, Appl. Phys.

Lett (2010).

9- G. Chang, C. J. Divin, C-H. Liu, S. L. Williamson, A. Galvanauskas, and T. B. Norris, Power Scalable Compact THz System Based on an Ultrafast Yb-Doped Fiber Amplifier, Optical Society of America (2006).

10- http://www.rp-photonics.com/pockels_effect.html.

11- K. R. Jha, and G. Singh, Terahertz Planar Antennas for Future Wireless Communication: A Technical Review, Infrared Physics & Technology (2013).

12- C. Schmuttenmaer, Exploring Dynamics in the Far-Infrared with Terahertz Spectroscopy, Chem, Lett 104, 1759-1779 (2004).

13- P. Han, X. Huang, and X. C. Zhang, Direct Characterization of Terahertz Radiation from the Dynamics of the Semiconductor Surface Field, Appl. Phys. Lett. 77, 2864(2000).

14- P. Gu, M. Tani, S. Kono, K. Sakai, and X. C. Zhang, Study of Terahertz Radiation from InAs and InSb, J. Appl. Phys. 91, 5533(2002).

15- G. B. I, P. N. Saeta, D. R. Dykaar, S. Schmittrink, and S. L. Chuang, Far-Infrared Light Generation at Semiconductor Surfaces and Its Spectroscopic Applications, IEEE J. Quantum Electron., 28, 2302 (1992).

16- C. X. Zhang, T. J. Darrow, B. B. Hu, H. D. Auston, T. M. Schmidt, P. Tham, and S. E. Yang, Optically Induced Electromagnetic-Radiation from Semiconductor Surfaces, Appl. Phys. Lett., 56, 2228(1990).

17- Y. Jin, F. X. Ma, A. G. Wagoner, M. Alexander, and C. X. Zhang, Anomalous Optically Generated Thz Beams from Metal Gaas Interfaces", Appl. Phys. Lett., 65, 682(1994).

18- X. Yin, B. W-H Ng, and D. Abbott, Terahertz Imaging for Biomedical Applications, Springer, Pattern Recognition and Tomographic Reconstruction, Springer Science and Business Media, LLC (2012).

19- V. Exter, L. Fattingar, and D. Grischkowsky, High-Brightness Terahertz Characterized with an Ultrafast Detector, Applied Physics Letters, 55, pp. 337–339 (1989).

20- B. P. Gorshunov, A. A. Volkov, A. S. Prokhorov, and I. E. Spektor, Phys. Solid State 50, 2001 (2008).

21- J. A. Fan, M. A. Belkin, and F. Capasso, Wide-Ridge Metal-Metal Terahertz Quantum Cascade Lasers with High-Order Lateral Mode Suppression, Applied Physics (2008).

22- S. Preu, G. H. Do¨hler, S. Malzer, L. J. Wang, and A. C. Gossard, Tunable Continuous-Wave Terahertz Photomixer Sources and Applications, Journal of Applied Physics 109, 061301 (2011).

23- L.S. Gregory, W. R. Tribe, B. E. Cole, C. Baker, M. J. Evans, I. V. Bradley, E. H. Linfield, A. G. Davies, and M. Missous, Phase Sensitive Continuous-Wave THz Imaging Using Diode Lasers, Electronics Letters Vol. 40 No. 2 (2004).

24- S. Matsuura, and H. Ito, in Terahertz Optoelectronics, edited by K. Sakai (Springer, Berlin(2005).

25- S. Matsuura, G. Blake, R. Wyss, J. Pearson, C. Kadow, and A. Gossard, Design and Characterization of Optical THz Phase Matched Traveling Wave Photomixers, Pro. SPIE (1999).

26- V. Ryzhii, M. Ryzhii, V. Mitin, M. S. Shur, and A. Satou et al, Terahertz Photomixing Using Plasma Resonances in Double-Graphene Layer Structures, J. Appl. Phys. 113, 174506 (2013).

27- P. Smith, D. Auston, and M. Nuss, Subpicosecond Photoconducting Dipole Antennas, IEEE J. Quantum Electron. 24, 255 (1988).

28- M. V. Extra, and D. R. Grischkowsky, Characterization of an Optoelectronic Terahertz Beam System, IEEE vol 38, No. 11(1990).

29- D. Saeedkia, Modeling and Design of Photoconductive and Superconductive Terahertz Photomixer Sources, aterloo, Ontario, Canada (2005).

30- K. Sakai, and M. Tani, Introduction to Terahertz Pulses, Chapter 1 from Terahertz Optoelectronics, Topics Appl. Phys. 97, 1–31, Springer-Verlag Berlin Heidelberg (2005).

31- P. Shumyatsky, and R. R. Alfano, Journal of Biomedical Optics, Terahertz Sources, 16(3), 033001 (2011).

32- K. Yamamoto, and H. Ishida, Kramers-Kronig Analysis Applied to Reflection-Absorption Spectroscopy, Vibrational Spectroscopy, 15 (1997).

33- F. Wei, Review of Terahertz Semiconductor Sources, Journal of Semiconductors, Vol. 33, No. 3(2011).

34- A. Agrawal, and A. Nahata, Time-Domain Radiative Properties of a Single Subwavelength Aperture Surrounded by an Exit Side Surface Corrugation, Optical Society of America (2006).

35- J. Dai, J. Zhang, W. Zhang, and D. Grischkowsky, Terahertz Time-Domain Spectroscopy Characterization of the Far-Infrared Absorption and Index of Refraction of High-Resistivity, Float-Zone Silicon, Optical Society of America (2004).

36- D. Saeedkia, Terahertz Photoconductive Antennas: Principles and Applications, TeTechS Inc., Waterloo, Ontario, Canada, EuCAP (2011).

37- J. Saxler, J. G. Rivas, C. Janke, H. P. M. Pellemans, P. H. Bol′ıvar, and H. Kurz, Time-Domain Measurements of Surface Plasmon Polaritons in the Terahertz Frequency Range, Physical Review B 69, 155427 (2004).

38- D. M. Hailu, H. Aziz, S. Safavi-Naeini, D. Saeedkia, Terahertz Time-Domain Spectroscopy of Organic Semiconductors, Proc. of SPIE Vol. 8624(2013).

39- G.P. Gallerano et al, Overview OF Terahertz Radiation Sources, Proceedings of the FEL Conference, 216-221 (2004).

40- J. Keeler, Chapter 4, Fourier Transformation and Data Processing (2002).

41- M. Walther, B. M. Fischer, A. Ortner, A. Bitzer, A Thoman and H. Helm, Chemical Sensing and Imaging with Pulsed Terahertz Radiation, Springer-Verlag (2010).

42- http://www.rp-photonics.com/femtosecond_lasers.html.

43- Ch. Fattinger and D. Grischkowsky, Terahertz Beams, Appl. Phys. Lett. 54 (6), (1988).

44- D. H. Auston, and K. P. Cheung, Coherent Time-Domain Far-Infrared Spectroscopy, Opt. Soc. Am. B/Vol. 2, No. 4 (1985).

45- J. Hebling, G. Almasi, I. Z. Kozma, and J. Kuhl, Velocity Matching by Pulse Front Tilting for Large Area THz-Pulse Generation, Opt. Express, (2002).

46- A. M. Sinyukov, M. R. Leahy, L. M. Hayden, M. Haller, J. Luo, A. K-Y. Jen, and L. R. Dalton, Resonance Enhanced THz Generation in Electro-Optic Polymers Near the Absorption Maximum, Applied Physics Letters (2004).

47- J. D. Kraus, Antennas. New York: McGraw-Hill, http://www.scribd.com/doc/8688310/Kraus-Antennas.

48- D. W. van der Weide, Planar Antennas for All-Electronic Terahertz Systems, Opt. Soc. Am. B, Vol. 11, No. 12 (1994).

49- I. Katayama, R. Akai, M. Bito, H. Shimosato, K. Miyamoto, H. Ito, and M. Ashida, Ultrabroadband Terahertz Generation Using 4-N,N-dimethylamino-4′-N′- methyl-Stilbazolium Tosylate Single Crystals, Appl. Phys. Lett. 97, 021105 (2010).

50- P. C. M. Planken, C. E. W. M. van Rijmenam, and R. N. Schouten, Opto-Electronic Pulsed THz Systems, Semicond. Sci. Technol. 20 S121–S127(2005).

51- A. Leitenstorfer, S. Hunsche, J. Shah, M. C. Nuss, and W. H. Knox, Detectors and Sources for Ultrabroadband Electro-Optic Sampling, Experiment and Theory, Applied Physics Letters (1999).

52- E. Castro-Camus, M. B. Johnston, and J Lloyd-Hughes, Simulation of Fluence-Dependent Photocurrent in Terahertz Photoconductive Receivers, Semicond. Sci. Technol. 27 115011(2012).

53- Y. J. Quan, L. P. Xiang, X. D. Gang, L YingJin, and L. Da, THz Source Based on Optical Cherenkov Radiation, www.springerlink.com, (2011).

54- M. J. Nasse, M. Schuh, S. Naknaimueang, M. Schwarz, A. Plech, Y.-L. Mathis, R. Rossmanith, P. Wesolowski, E. Huttel, M. Schmelling, and A.-S. Müller, Flute: A Versatile Linac-Based THz Source, Rev. Sci. Instrum. 84, 022705 (2013).

55- M. van Exter, Ch. Fattinger, and D. Grischkowsky, Terahertz Time-Domain Spectroscopy of Water Vapor, optics letter,(1989).

56- A. Davies, E. H. Linfield, and M. B. Johnston, The Development of Terahertz Sources and their Applications, Phys. Med. Biol. 47 3679–3689(2002).

57- J. Mangeney, THz Photoconductive Antennas Made From Ion-Bombarded Semiconductors, Springer Science+Business Media, (2011).

58- A. Bergner, U. Heugen, E. Bründermann, G. Schwaab, and M. Havenitha, New p-Ge THz Laser Spectrometer for the Study of Solutions:THz Absorption Spectroscopy of Water, Review of Scientific Instruments 76, 063110 (2005).

59- D. Grischkowsky, S. Keiding, M. Van Exter, and C. Fattinger, Far-Infrared Time-Domain Spectroscopy with Terahertz Beams of Dialectics and Semiconductors, JOSA B, Vol. 7(1990).

60- S-G. Park, M. R. Melloch, and A. M. Weiner, Comparison of Terahertz Waveforms Measured by Electro-Optic and Photoconductive Sampling, Applied Physics Letters, Volume 73, N. 22,(1998).

61- J. F. O'Hara, W. Withayachumnankul, I. Al-Naib, A Review on Thin-film Sensing with Terahertz Waves, Springer Science+Business Media, LLC (2012).

References for Chapter 3:

1- J. F. O Hara. W. Withayachumnankul, I. Al-Naib, A Review on Thin-film Sensing with

Terahertz Waves, Springer Science (2012).

2- I. Pupeza, R. Wilk, and M. Koch, Highly Accurate Optical Material Parameter Determination with THz Time-Domain Spectroscopy, Optical Society of America, (2007).

3- Strachan, C.J., et al, Using Terahertz Pulsed Spectroscopy to Study Crystalline of Pharmaceutical Materials. Chem. Phys. Lett, (2004).

4- P. U. Jepsen and B. M. Fischer, Dynamic Range in Terahertz Time-Domain Transmission and Reflection Spectroscopy, Optics Letters (2004).

5- T-I. Jeon and D. Grischkowsky, Characterization of Optically Dense, Doped Semiconductors by Reflection THz Time Domain Spectroscopy, Applied Physics Letters (1998).

6- M. Van Extra, and D. R. Grischkowsky: Characterization of an Optoelectronic Terahertz Beam System, IEEE , VOL 38, No. 11, (1990).

7- S. E. Ralph, S. Perkowitz, N. Katzenellenbogen and D. Grischkowsky, Terahertz Spectroscopy of Optically Thick Multilayered Semiconductor Structures, Optical Society of America (1994).

8- K-E. Peiponen, and E. Gornov, Complex Refractive Index of Media in the THz Spectral Range, Chapter 3 from Terahertz Spectroscopy and Imaging book, Springer, c(2013).

9- J. M. Cowley, Diffraction Physics book, Third Edition (1995).

10- T. Nagashima, and M. Hangyo, Measurement of Complex Optical Constants of a Highly Doped Si Wafer Using Terahertz Ellipsometry, Applied Physics Letters (2001).

11- K. Wiesauer, and Ch. Jordens, Recent Advances in Birefringence Studies at THz Frequencies, Springer (2013).

12- Z. Xi-Cheng, and X. Jingzhou, Chapter 3 from Introduction to THz Wave Photonics Book, Springer (2011).

13- D. Grischkowsky, S. Keiding, M. Van Exter, and Ch. Fattinger, Far-Infrared Time-Domain Spectroscopy with Terahertz Beams of Dielectrics and Semiconductors, Optical Society America (1990).

14- L. Duvillaret, F. Garet, and J. Coutaz, A Reliable Method for Extraction of Material Parameters in Terahertz Time-Domain Spectroscopy, IEEE (1996).

15- D. Liu, B. Gaucher, U. Pfeiffer, J. Grzyb, Chapter Three from Advanced Millimeter-Wave Technologies, Wiley (2009).

16- J. W. Cooley, J. W. Tukey, An algorithm for the machine calculation of complex Fourier series, Math compute (1965).

17- L. Duvillaret, F. Garet, J-L. Coutaz, Influence of noise on the characterization of materials by terahertz time-domain spectroscopy, Optical Society of America (2000).

18- Z. Jiang, M. Li, and X.-C. Zhang, Dielectric Constant Measurement of Thin Films by Differential Time-Domain Spectroscopy, Appl. Phys. Lett. (2000).

19- Z. Xi-Cheng, and Xu. Jingzhou, Chapter 4 from Introduction to THz Wave Photonics Book, Springer (2011).

20- S. L. Dexhemimer, Chapter 1 from Terahertz Spectroscopy: Principles and

Applications, CRC (2007).

21- D. Saeedkia, Chapter 3 from Handbook of Terahertz Technology for Imaging, Sensing and Communications, Woodhead publishing, (2013).

22- S. L. Chuang, Chapter 5 from Physics of Photonic Devices, Second Edition Wiley (2009).

23- G. Gruner, Chapter 2 from Millimeter and Submillimeter Wave Spectroscopy of Solids, Springer (1998).

24- H. Roskos, M. Nuss, J. Shah, B. Tell, and J. Cunninghm, Terahertz Absorption between Split Subbands in Coupled Quantum Wells, Optical society of America on Picosecond Electronics and Optoelectronics (1991).

25- A. Stylianou, M. Talias, Review in Nanotechnology-Supported THz Medical imaging, Fl000Research (2013).

26- D. Saeedkia, Chapter 20 from Handbook of Terahertz Technology for Imaging, Sensing and Communications, Woodhead publishing, (2013).

27- J. Lloyd-Hughes, T-I Jeon, A review of the Terahertz Conductivity of Bulk and Nano-Materials, Journal of Infrared, Millimetre and Terahertz Waves (2012).

28- E. Russellt, and E. Bell, Optical Constants of Sapphire in the Far Infrared (1966).

29- M. Johnston, L. Herz, A.L.T. Khan, A. Kohhler, A. Davies, and E. Linfield, Low-Energy Vibrational Modes in Phenylene Oligomers Studied by THz Time-Domain Spectroscopy, Chemical Physics Letters (2003).

30- B. Jin, C. Zhang, P. Wu, Sh. Liu, Recent Progress of Terahertz Spectroscopy on Medicine and Biology in China, Terahertz Science and Technology (2010).

31- W. Lai, H. Zhang, Y. Zhu, Q. Wen, A Novel Method to Measure Dielectric Properties of Materials in Terahertz Spectroscopy, Optik (2013).

32- J. El Haddad, B. Bousquet, L. Canioni, P.Mounaix, Review in Terahertz Spectral Analysis, Elsevier (2013).

33- G. Wang, J. Shen, and Y. Jia, Vibrational Spectra of Ketamine Hydrochloride and 3, 4-Methylenedioxymethamphetamine in Terahertz Range, J. Appl. Phys. (2007).

34- M. Walther, B. Fischer, M. Schall, H. Helm, and P. U. Jepsen, Far-Infrared Vibrational Spectra of All-trans, 9-cis and 13-cis Retinal Measured by THz Time-Domain Spectroscopy, Chemical Physics Letters, (2000).

35- T. Lu, Z. Kun, Z. Qing-Li, S. Yu-Lei, and Z. Cun-Lin, Quantitative Analysis for Monitoring Formulation of Lubricating Oil Using Terahertz Time-Domain Transmission Spectroscopy, Chin. Phys. Lett (2012).

36- P. D. Cunningham, N.N. Valdes, F. A. Vallejo, L. M. Hayden, B. Polishak, X-H. Zhou, J. Luo, A. K-Y. Jen, J. C. Williams, and R. J. Twieg, Broadband Terahertz Characterization of the Refractive Index and Absorption of some Important Polymeric and Organic Electro-Optic Materials, J. Appl. Phys. (2011).

37- D. Hailu, S. Alqarni, B. Cui, D. Saeedkia, Terahertz Surface Plasmon Resonance Sensor for Material Sensing, SPIE (2013).

38- J. B. Pendry, A. J. Holden, D. J. Robbins, and W. J. Stewart, Magnetism from Conductors and Enhanced Nonlinear Phenomena, IEEE (1999).

39- T. H. Isaac, W. L. Barnes, and E. Hendry, Determining the Terahertz Optical

Properties of Subwavelength Films Using Semiconductor Surface Plasmons, Appl. Phys. Lett. (2008).

40- S. Wietzke, C. Jansen, M. Reuter, T. Jung, D. Kraft, S. Chatterjee, B.M. Fischer, and M. Koch, Terahertz Spectroscopy on Polymers: Review of Morphological Studies, Journal of Molecular Structure (2011).

41- M. D. King, W. D. Buchanan, and T. M. Korter, Identification and Quantification of Polymorphism in the Pharmaceutical Compound Diclofenac Acid by Terahertz Spectroscopy and Solid-State Density Functional Theory, Anal. Chem. (2011).

42- Z. Zhang, X. Yu, H. Zhao, T. Xiao, Z. Xi, H. Xu, Component Analysis to Isomer Mixture with THz-TDS, Optics Communications, (2007).

43- Zomega Terahertz Corporation, The Terahertz Wave eBook, (2012).

44- Y-C Shen, Terahertz Pulsed Spectroscopy and Imaging for Pharmaceutical Applications: A review, International Journal of Pharmaceutics (2011).

45- W. Zouaghi, M. D. Thomson, K. Rabia, R. Hahn, V. Blank and H. G. Roskos, Broadband Terahertz Spectroscopy: Principles, Fundamental Research and Potential for Industrial Applications, Eur. J. Phys, (2013).

46- M. Hangyo, M. Tani, and T. Nagashima, Terahertz Time-Domain Spectroscopy of Solids: A review, International Journal of Infrared and Millimeter Waves, (2005).

47- B. Ferguson, and X-C. Zhang, Materials for Terahertz Science and Technology, Review Article, Nature Materials, (2002).

48- Y. Watanabe, K. Kawase, T. Ikari, H. Ito, Y. Ishikawa, and H. Minamide, Component Analysis of Chemical Mixtures Using Terahertz Spectroscopic Imaging, Optics Communications, (2004).

49- S. Suranjana, Chapter 4 from Characterization of Terahertz Emission from High Resistivity Fe-doped Bulk Ga0.69In0.31As Based Photoconducting Antennas, Springer (2011).

50- S. P. Mickan, K-S Lee, T-M Lu, E. Barnat, J. Munch, D. Abbott and X-C. Zhang, Thin Film Characterization Using Terahertz Differential Time-Domain Spectroscopy and Double Modulation, SPIE (2001).

51- M. Neshat, D. Saeedkia, R. Sabry, and S. Safavi-Naeini, An Integrated Continuous-Wave Terahertz Biosensor, Proc. of SPIE, (2007).

52- Y-S Jin, G-J Kim, and S-G Jeon, Terahertz Dielectric Properties of Polymers, Journal of the Korean Physical Society, (2006).

53- Aurele Joseph Louis Adam, Review of Near-Field Terahertz Measurement Methods and Their Applications, How to Achieve Sub-Wavelength Resolution at THz Frequencies, J Infrared Milli Terahz Waves, (2011).

54- C. Yu, S. Fan, Y. Sun, and E. Pickwell-MacPherson, The Potential of Terahertz Imaging for Cancer Diagnosis: A review of Investigations to Date, Quant Imaging Med Surg (2012).

55- M. Naftaly, and R. E. Miles, Member IEEE, Terahertz Time-Domain Spectroscopy for Material Charectrization, Proc. Of IEEE, (2007).

56- S. Krishnamurthy, M. T. Reiten, S. A. Harmon, and R. A. Cheville, Characterization of Thin Polymer Films Using Terahertz Time-Domain Interferometry, Appl. Phys. Lett.,

(2001).

57- C. Baker, W. R. Tribe, T. Lo, B. E. Cole, S. Chandler, M. C. Kemp, People Screening Using Terahertz Technology, Terahertz for Military and Security Applications III, edited by R. Jennifer Hwu, Dwight L. Woolard, Mark J. Rosker, Proc. of SPIE Vol. 5790 (2005).

58- A. Majewski, P. Miller, R. Abreu, J. Grotts, T. Globus, and E. Brown, Terahertz Signature Characterization of Bio-Simulants,Terahertz for Military and Security Applications III, edited by R. Jennifer Hwu, Dwight L. Woolard, Mark J. Rosker, Proc. of SPIE Vol. 5790 (2005).

59- S. Kojimaa, M. Wada Takeda, and S. Nishizawa, Terahertz Time Domain Spectroscopy of Complex Dielectric Constants of Boson Peaks, Journal of Molecular Structure (2003).

60- T. Hasebe, S. Kawabe, H. Matsui, and H. Tabata, Metallic Mesh-Based Terahertz Biosensing of Single- and Double-Stranded DNA, J. Appl. Phys. 112, 094702 (2012).

61- M. Brucherseifer, M. Nagel, P. H. Bolivar, and H. Kurz, Label-Free Probing of the Binding State of DNA by Time-Domain Terahertz Sensing, Appl. Phys. Lett., Vol. 77. (2000).

62- G. Houzet , K. Blary , S. Lepilliet , D. Lippens , L. Burgnies , G. Velu , J. C. Carru , E. Nguema and, P. Mounaix, Ionic Polarization Occurrence in BaSrTiO3 Thin Film by THz- Time Domain Spectroscopy, Ferroelectrics, 430:1, 36-41(2012).

63- R. A. Kaindl, M. A. Carnahan, J. Orenstein, D. S. Chemla, H. M. Christen, H-Y Zhai, M. Paranthaman, and D. H. Lowndes, Far-Infrared Optical Conductivity Gap in Superconducting MgB2 Films, 10.1103/PhysRevLett.88.027003 (2002).

64- W. Withayachumnankul, Limitation in Thin-Film Detection with Transmission-Mode Terahertz Time-Domain Spectroscopy, arXiv:1111.3498v1 [physics.optics](2011).

65- K. C. Oppenheim, T. M. Korter, J. S. Melinger, and D. Grischkowsky, Solid-State Density Functional Theory Investigation of the Terahertz Spectra of the Structural Isomers 1,2-Dicyanobenzene and 1,3-Dicyanobenzene, J. Phys. Chem. A, Vol. 114, No. 47(2010).

66- W. Withayachumnankul, J. F. O'Hara, W. Cao, I. Al-Naib, and W. Zhang, Limitation in Thin-Film Sensing with Transmission-Mode Terahertz Time-Domain Spectroscopy, Vol. 22, No. 1 Optics Express (2014).

67- S. S. Harsha, J. S. Melinger, S. B. Qadri, and D. Grischkowsky, Substrate Independence of THz Vibrational Modes of Polycrystalline Thin Films of Molecular Solids in Waveguide THz-TDS, J. Appl. Phys. 111, 023105 (2012).

68- J. Petzelt, P.Kuzel, I. Rychetsky, A. Pashkin, and T. Ostapchuk, Dielectric Response of Soft Modes in Ferroelectric Thin Films, Taylor & Francis Inc. Ferroelectrics, 288: 169–185, (2003).

69- L. Duvillaret, F. Garet, and J-L. Coutaz, Highly Precise Determination of Optical Constants and Sample Thickness in Terahertz Time-Domain Spectroscopy, Applied Optics, Vol. 38, No. 2 (1999).

70- T. F. Berlin, Chapter 21 from Springer Handbook of Lasers and Optics, Springer, c(2012).

71- J. F. OHara, R. Singh, I. Brener, E. Smirnova, J. Han, A. J. Taylor, and W. Zhang, Thin-Film Sensing with Planar Terahertz Metamaterials: Sensitivity and Limitations, Optics Express, Vol. 16, No. 3(2008).

72- J. S. Melinger, S. Sree Harsha, N. Laman, and D. Grischkowsky, Guided-Wave Terahertz Spectroscopy of Molecular Solids, Invited, J. Opt. Soc. Am. B/Vol. 26, No. 9 (2009).

73- M. Scheller, C. Jansen, M. Koch, Analyzing Sub-100-lm Samples with Transmission Terahertz Time Domain Spectroscopy, Optics Communications 282 1304–1306, (2009).

74- N. Laman, S. Sree Harsha, D. Grischkowsky, and J. S. Melinger, 7 GHz Resolution Waveguide THz Spectroscopy of Explosives Related Solids Showing New Features, Optics Express 4094, Vol. 16, No. 6, (2008).

75- W. Withayachumnankul, B. M. Fischer, H. n Lin, and D. Abbott, Uncertainty in Terahertz Time-Domain Spectroscopy Measurement, J. Opt. Soc. Am. B/Vol. 25, No. 6, (2008).

76- N. Laman, S. S. Harsha, and D. Grischkowsky, Narrow-Line Waveguide Terahertz Time-Domain Spectroscopy of Aspirin and Aspirin Precursors, Applied Spectroscopy, Volume 62(2008).

77- X. Li, Z. Hong, J. He, and Y. Chen, Precisely Optical Material Marameter Determination by Time Domain Waveform Rebuilding with THz Time-Domain Spectroscopy, Optics Communications 283 4701–4706 (2010).

78- W. Withayachumnankul, B. M. Fischer, and D. Abbott, Material Thickness Optimization for Transmission-Mode Terahertz Time-Domain Spectroscopy, Optics Express 7382, Vol. 16, No. 10(2008).

79- W. Withayachumnankul, H. Lin, K. Serita, C. M. Shah, S. Sriram, M. Bhaskaran, M. Tonouchi, C. Fumeaux, and D. Abbott, Sub-Diffraction Thin-Film Sensing with Planar Terahertz Metamaterials, Optics Express 3345, Vol. 20, No. 3 (2012).

80- T. Chen, S. Li, and H. Sun, Review Metamaterials Application in Sensing, Sensors, 10.3390/s120302742(2012).

81- T. Michael, G. Daniel, and B. Rene, Sensitive Determination of Layer Thickness by Waveguide Terahertz Time-Domain Spectroscopy, Sensor Test Conference OPTO Proceeding (2011).

82- A. G. Davies, and E. H. Linfield, Molecular and Organic Interactions, R.E. Miles et al. (eds.), Terahertz Frequency Detection and Identification of Materials and Objects, 91–106, Springer (2007).

83- H-B. Liu, and X-C. Zhang, Terahertz Spectroscopy for Explosive, Pharmaceutical, and Biological Sensing Applications, R.E. Miles et al. (eds.), Terahertz Frequency Detection and Identification of Materials and Objects, 251–323, Springer(2007).

84- M. Chamberlain, Applied Terahertz Science: the Technology of the Future, and Always Will Be?, R.E. Miles et al. (eds.), Terahertz Frequency Detection and Identification of Materials and Objects, 341–352. Springer (2007).

85- J. G. Rivas, M. Kuttge, P. Haring Bolivar, and H. Kurz, Propagation of Surface Plasmon Polaritons on Semiconductor Gratings, The American Physical Society, PRL 93,

256804 (2004).

86- N. C. J. van der Valk, and P.C. M. Planken, Effect of a Dielectric Coating on Terahertz Surface Plasmon Polaritons on Metal Wires, Appl. Phys. Lett. 87, 071106 (2005).

87- K. Wang and D. M. Mittleman, Dispersion of Surface Plasmon Polaritons on Metal Wires in the Terahertz Frequency Range, PRL 96, 157401 (2006).
W. Withayachumnankul and M. Naftaly, Fundamentals of Measurement in Terahertz Time-Domain Spectroscopy, Springer Science+Business Media New York (2013).

References for Chapter 4:

1- D. Saeedkia, Chapter 3 from Handbook of Terahertz Technology for Imaging, Sensing and Communications, Woodhead publishing (2013).

2- P. N. Prasad, Nonophotonics, John Wiley and Sons, Inc. (2004).

3- H. Altan, Plasma Sensing Using Terahertz Waves, Chapter 1 from Terahertz and Mid Infrared Radiation, Mauro F. Pereira, Oleksiy Shulika, NATO Science for Peace and Security Series, Sub-Series B. Physics and Biophysics, (2011).

4- J. Homola, Electromagnetic Theory of Surface Plasmons, Chapte 1 from Surface Plasmon Resonance Based Sensors Springer Ser Chem Sens Biosens 10.1007/5346_013 (2006).

5- J. F. O'Hara, W. Withayachumnankul, I. Al-Naib, A Review on Thin-Film Sensing with Terahertz Waves, J Infrared Milli Terahz Waves 33:245–291(2012).

6- F. E. Hernandez, Optics and Plasmonics: Fundamental Studies and Applications, Chapter 7 from Reviews in plasmonics 2010, Geddes, Chris D, New York, NY : Springer, c (2012).

7- N. J. de Mol, and M. J. E. Fischer, Surface Plasmon Resonance: A General Introduction, Chapter 1 from Surface Plasmon Resonance: Methods and Protocols, Mol, Nico J. de, Fischer, and Marcel J. E, New York : Humana Press (2010).

8- W. L. Barnes, A. Dereux and T. W. Ebbesen, insight review articles, Surface Plasmon Subwavelength Optic, Nature, Vol 424, (2003).

9- X-C. Zhang, J. Xu, THz Wave Interaction with Materials, Chapter 4 from Introduction to THz Wave Photonics, Springer Science+Business Media, LLC, 10.1007/978-1-4419-0978-7_4 (2010).

10- R. W. Wood, Anomalous Diffraction Gratings, P Ei YS ICAL Review, Volume 48, (1935).

11- A. Moores, and F. Goettmann, The Plasmon Band in Noble Metal Nanoparticles: an Introduction to Theory and Applications, New J. Chem. 30, 1121–1132 (2006).

12- N. C. Lindquist, P. Nagpal, K. M. McPeak, D. J. Norris, and S- H. Oh, Engineering Metallic Nanostructures for Plasmonics and Nanophotonics, Rep Prog Phys. 75(3): 036501 (2012).

13- S. Pidishety, and N. K. Viswanathan, Polarimetric Measurement of Optically Perturbed Surface Plasmonic Field, J. Opt. Soc. Am. B / Vol. 30, No. 4(2013).

14- J. B. Pendry, L. Martın-Moreno, and F. J. Garcia-Vidal, Mimicking Surface Plasmons

with Structured Surfaces, Science VOL 305(2004).

15- J. G. Rivas, M. Kuttge, P. Haring Bolivar, and H. Kurz, Propagation of Surface Plasmon Polaritons on Semiconductor Gratings, The American Physical Society, PRL 93, 256804 (2004).

16- Aurele Joseph Louis Adam, Review of Near-Field Terahertz Measurement Methods and Their Applications; How to Achieve Sub-Wavelength Resolution at THz Frequencies, J Infrared Milli Terahz Waves, 10.1007/s10762-011-9809-2, Springer (2011).

17- A. Sihvola, J. Qi, and I. V. Lindell, Bridging the Gap Between Plasmonics and Zenneck Waves, IEEE Antennas and Propagation MagaZine, Vol. 52, No.1(2010).

18- N. C. J. van der Valk, and P.C. M. Planken, Effect of a Dielectric Coating on Terahertz Surface Plasmon Polaritons on Metal Wires, Appl. Phys. Lett. 87, 071106 (2005).

19- J. Saxler, J. G. Rivas, C. Janke, H. P. M. Pellemans, P. H. Bolıvar, and H. Kurz, Time-Domain Measurements of Surface Plasmon Polaritons in the Terahertz Frequency Range, Physical Review B 69, 155427 (2004).

20- K. Wang and D. M. Mittleman, Dispersion of Surface Plasmon Polaritons on Metal Wires in the Terahertz Frequency Range, PRL 96, 157401 (2006).

21- S. Li, M. M. Jadidi, T. E. Murphy, and G. Kumar, Terahertz Surface Plasmon Polaritons on a Semiconductor Surface Structured with Periodic V-Grooves, Optics Express 7042, Vol. 21, No. 6 (2013)

22- I. S. Spevak, M. Tymchenko, V. K. Gavrikov, V. M. Shulga, J. Feng, H. B. Sun, Yu. E. Kamenev, and A. V. Kats, Surface Plasmon-Polariton Resonance at Diffraction of THz Radiation on Semiconductor Gratings, arXiv:1305.1785, Physics Optics (2013).

23- V. Ryzhii, M. Ryzhii, V. Mitin, M. S. Shur, A. Satou, and T. Otsuji, Terahertz Photomixing Using Plasma Resonances in Double-Graphene Layer Structures, J. Appl. Phys. 113, 174506 (2013).

24- C.W. Berry, N. Wang, M.R. Hashemi, M. Unlu and M. Jarrahi, Significant Performance Enhancement in Photoconductive Terahertz Optoelectronics by Incorporating Plasmonic Contact Electrodes, Nature Communications 4:1622,10.1038, ncomms2638 (2013).

25- M. Dragoman, D. Dragoman, Review Plasmonics: Applications to Nanoscale Terahertz and Optical Devices, Progress in Quantum Electronics 32 1–41(2008).

26- Y. Wang, X. Wang, Q. Wu, X-j. He, T-l. Gui and Y-J Tong, Surface Plasmon Resonant THz Wave Transmission on Carbon Nanotube Film, Springer Science+Business Media, LLC (2011).

27- M. tonouchi, Review Articles Cutting-Edge Terahertz Technology, Nature Photonics, VOL 1, (2007).

28- A. Stylianou, and M. A Talias, Review Nanotechnology-Supported THz Medical Imaging, f1000research.2-100.v1(2013).

29- W. Cao, C. Song, T. E. Lanier, R. Singh, J. F. O'Hara, W. M. Dennis, Y. Zhao, and W. Zhang, Tailoring Terahertz Plasmons with Silver Nanorod Arrays, Scientific Reports, 10.1038/srep01766 (2013).

30- J. G. Rivas, C. Janke, P. H. Bolivar, and H. Kurz, Transmission of THz Radiation

Through InSb Gratings of Subwavelength Apertures, Optics Express, Vol. 13, No. 3(2005).

31- H. Cao, A. Agrawal and A. Nahata, Controlling the Transmission Resonance Lineshape of a Single Subwavelength Aperture, Optics Express 763, Vol. 13, No. 3(2005).

32- G. Li, Z. Jin, X. Xue, X. Lin, G. Ma, S. Hu, and N. Dai, Terahertz Coherent Control of Surface Plasmon Polariton Propagation in Subwavelength Metallic Hole Arrays, Appl. Phys. Lett. 100, 191115 (2012).

33- J. Han, Abul. K. Azad, M. Gong, X. Lu, and W. Zhang, Coupling Between Surface Plasmons and Nonresonant Transmission in Subwavelength Holes at Terahertz Frequencies, Appl. Phys. Lett. 91, 071122 (2007).

34- T. W. Ebbesen, H. J. Lezec, H. F. Ghaemi, T. Thio, and P. A. Wolff, Extraordinary Optical Transmission Through Sub-Wavelength Hole Arrays, Nature, VOL 391 (1998).

35- D. Qu, D. Grischkowsky, and W. Zhang, Terahertz Transmission Properties of Thin Subwavelength Metallic Hole Arrays, Optics Letters, Vol. 29, No. 8 (2008).

36- W. Zhang and Abul. K. Azad, Extraordinary Terahertz Transmission of Subwavelength Plasmonic Structures, from Terahertz Physics, Devices, and Systems, edited by M. Anwar, A. J. DeMaria, and M. S. Shur, Proc. of SPIE Vol. 6373, 63730P, (2006).

37- A. Agrawal, and A. Nahata, Time-Domain Radiative Properties of a Single Subwavelength Aperture Surrounded by an Exit Side Surface Corrugation, Optics Express, Vol. 14, No. 5(2006).

38- Abul. K. Azad, J. F. O'Hara, R. Singh, H-T. Chen, and A. J. Taylor, A Review of Terahertz Plasmonics in Subwavelength Holes on Conducting Films, IEEE Journal of Selected Topics in Quantum Electronics, VOL. 19, NO. 1(2012).

39- H. F. Ghaemi, T. Thio, D. E. Grupp, T. W. Ebbesen, and H. J. Lezec, Surface Plasmons Enhance Optical Transmission Through Subwavelength Holes, The American Physical Society VOL 58, N. 11(1998).

40- Abul. K. Azad, Y. Zhao, and W. Zhang, Transmission Properties of Terahertz Pulses Through an Ultrathin Subwavelength Silicon Hole Array, Appl. Phys. Lett. 86, 141102 (2005).

41- J. V. Coe, J. M. Heer, S. Teeters-Kennedy, H. Tian, and K. R. Rodriguez, Extraordinary Transmission of Metal Films with Arrays of Subwavelength Holes, Annu. Rev. Phys. Chem. 59:179–202 (2008).

42- D. Qu and D. Grischkowsky, Observation of a New Type of THz Resonance of Surface Plasmons Propagating on Metal-Film Hole Arrays, Phys Rev Lett.93.196804(2004).

43- F. Miyamaru, S. Hayashi, C. Otani, and K. Kawase, Terahertz Surface-Wave Resonant Sensor with a Metal Hole Array, Optics Letters, Vol. 31, No. 8 (2006).

44- K. Ishihara, T. Ikari, H. Minamide, J-I. Shikata, K. Ohashi, H. Yokoyama, and H. Ito, Terahertz-Wave Near-Field Imaging with Subwavelength Resolution Using Surface-Wave-Assisted Bow-Tie Aperture, Appl. Phys. Lett. 89, 201120 (2006).

45- K. Ishihara, G. Hatakoshi, T. Ikari, H. Minamide, H. Ito, and K. Ohashi, Terahertz Wave

Enhanced Transmission through a Single Subwavelength Aperture with Periodic Surface Structures, Jpn. J. Appl. Phys. 44 (2005).

46- H. Cao and A. Nahata, Resonantly Enhanced Transmission of Terahertz Radiation Through a Periodic Array of Subwavelength Apertures, Optics Express, Vol. 12, No. (2004).

47- C. Janke, J. G. Rivas, C. Schotsch, L. Beckmann, P. H. Bolivar, and H. Kurz, Optimization of Enhanced Terahertz Transmission through Arrays of Subwavelength Apertures, Physical Review B 69, 205314 (2004).

48- F. Yang, J. R. Sambles, and G. W. Bradberry, Long-Range Surface Modes Supported by Thin Films, Phys. Rev. B 44, 5855 (1991).

49- R. H. RITCHIE, Plasma Losses by Fast Electrons in Thin Films, Phys. Rev. VOL 106 N. 5 (1957).

50- N. P. Pham, E. Boellard, P. M. Sarro and J. N. Burghartz, Spin, Spray coating and Electrodeposition of Photoresist for MEMS Structures – a Comparison, Delft University of Technology, DIMES.

51- SU-8 Permanent Photoresists, MICRO-CHEM.

52- P. M. Dentinger, W. Miles Clift, S. H. Goods, Removal of SU-8 Photoresist for Thick Film Applications, Microelectronic Engineering 61–62 (2002).

53- J. Yeom, Y. Wu, J. C. Selby, and M. A. Shannon, Maximum Achievable Aspect Ratio in Deep Reactive Ion Etching of Silicon due to Aspect Ratio Dependent Transport and the Microloading Effect, J. Vac. Sci. Technol. B, Vol. 23, No. 6 (2005).

54- G. V. Bianco, M. Losurdo, M. M. Giangregorio, P. Capezzuto, and G. Bruno, Real Time Monitoring of the Interaction of Si (100) with Atomic Hydrogen: The "H-insertion/Si-Etching" Kinetic Model Explaining Si Surface Modifications, Appl. Phys. Lett. 95, 161501 (2009).

55- E. Dilonardo, G. V. Bianco, M. M. Giangregorio, M. Losurdo, P. Capezzuto, and G. Bruno, Silicon Doping Effect on SF6/O2 Plasma Chemical Texturing, J. Appl. Phys. 110, 013303 (2011).

56- J. H. Choi, L. Latu-Romain, E. Bano, F. Dhalluin, T. Chevolleaư and T. Baron, Fabrication of SiC n]Nanopillars by Inductively Coupled SF_6/O_2 Plasma Etching, J. Phys. D: Appl. Phys. 45 (2012).

57- Y. Tsuji, M. Yanagisawa, H. Yoshinaga, and K. Hiratsuka, Study of Reactive Ion Etching for Reverse Tone Nanoimprint Process, Journal of Physics: Conference Series 191 (2009).

58- D. L. Flamm, Mechanisms of Silicon Etching in Fluorine- and Chlorine-Containing Plasmas, pure & Appl. Chem.,Vol. 62, No. 9 (1990).

59- Y. Khairallah. F. Khonsari-Ar, E. I, and J. Amouroux, Decomposition of Gaseous Dielectrics (CF4,SF6) by a Non-Equilibrium Plasma. Mechanisms, Kinetics, Mass Spectrometric Studies and Interactions with Polymeric Targets, & Appl. Chem., Vol. 66, No. 6 (1994).

60- H. Zou, Anisotropic Si Deep Beam Etching with Profile Control Using SF_6/O_2 Plasma, Microsystem Technologies 10603–607 Springer-Verlag (2004).

61- Y-D. Lim, S-H. Lee and W. J. Yoo, Roles of F and O Radicals and Positive Ions in a SF_6/O_2 Plasma in Forming Deep Via Structures, Journal of the Korean Physical Society, Vol. 54, No. 5 (2009).

62- J. L. Lyman, and T. Noda, Thermochemical Properties of Si_2F_6 and SiF_4 in Gas and Condensed Phases, J. Phys. Chem. Ref. Data, Vol. 30, No. 1, (2001).

63- Z. Cui, Chapter 6 from Nanofabrication, Pringer Science Business Media, LLC (2008).

64- R. Knizikevicius, Simulations of Si and SiO_2 Etching in SF_6+O_2 Plasma, ACTA Physica Polonica, Vol. 117 (2010).

65- B. Wu, A. Kumar, and S.a Pamarthy, High Aspect Ratio Silicon Etch: A review, J. Appl. Phys. 108, 051101 (2010).

66- J. D. Plummer, M. D. Deal, and P. B, Griffin. Silicon VLSI Technology.

67- Ansoft HFSS ver. 13.1, Ansoft Corporation, 225 West Station Square Drive, Suite 200, Pittsburgh, PA 15219 USA, (2010).

68- D. Hailu, S. Alqarni, B. Cui, D. Saeedkia, Terahertz Surface Plasmon Resonance Sensor for Material Sensing, SPIE, (2013).

References for Figures:

1- Y-S Lee, Chapter 1 from Principles of Terahertz Science and Technology, New York Springer 978-0-387-09540-0 (2009).
2- X-C Zhang, and J. Xu, Terahertz Radiation Chapter 1 from Introduction to THz Wave Photonic, Springer Science and Business Media, LLC (2010).
3- M. Walther, B. M. Fischer, A. Ortner, A. Bitzer, A. Thoman, and H. Helm, Review: Chemical Sensing and Imaging with Pulsed Terahertz Radiation, Anal Bioanal Chem 397:1009–1017, Springer-Verlag (2010).
4- A. G Davies, E H Linfield and M B Johnston, The Development of Terahertz Sources and their Applications, Phys. Med. Biol. 47 3679–3689 (2002).
5- http://fir.u-fukui.ac.jp/thzlab/index_files/Eng_THz_TDS.htm
6- A. Tomasino, A. Parisi, S. Stivala, P. Livreri, A. C. Cino, A. Busacca, M. Peccianti, and R. Morandotti, Wideband THz Time Domain Spectroscopy Based on Optical Rectification and Electro-Optic Sampling, Scientific Reports doi:10.1038/srep03116 (2013)
7- http://optipedia.info/en_fiberlaser/subsection-Solid-state-laser.html.
8- K. Sakai, and M. Tani, Introduction to Terahertz Pulses, Chapter 1 from Terahertz Optoelectronics, Topics Appl. Phys. 97, 1–31, Springer-Verlag Berlin Heidelberg (2005).
9- C. Schmuttenmaer, Exploring Dynamics in the Far-Infrared with Terahertz Spectroscopy, Chem, Lett 104, 1759-1779 (2004).
10- X. Yin, B. W-H Ng, and D. Abbott, Terahertz Imaging for Biomedical Applications, springer, Pattern Recognition and Tomographic Reconstruction, Springer Science and Business Media, LLC (2012).
11- Z. Xi-Cheng, and Xu. Jingzhou, Chapter 4 from Introduction to THz Wave Photonics Book, Springer (2011).
12- Zomega Terahertz Corporation, The Terahertz Wave eBook (2012).
13- D. Grischkowsky, S. Keiding, M. Van Exter, and Ch. Fattinger, Far-Infrared Time-Domain Spectroscopy with Terahertz Beams of Dielectrics and Semiconductors, Optical Society America (1990).
14- P. Uhd Jepsen and B. M. Fischer, Dynamic Range in Terahertz Time-Domain Transmission and Reflection Spectroscopy, Optics Letters (2004).
15- L. Duvillaret, F. Garet, and J. Coutaz, A Reliable Method for Extraction of Material Parameters in Terahertz Time-Domain Spectroscopy, IEEE (1996).
16- P. D. Cunningham, N.N. Valdes, F. A. Vallejo, L. M. Hayden, B. Polishak, X-H. Zhou, J. Luo, A. K-Y. Jen, J. C. Williams, and R. J. Twieg, Broadband Terahertz Characterization of the Refractive Index and Absorption of some Important Polymeric and Organic Electro-Optic Materials, J. Appl. Phys. (2011).
17- W. Withayachumnankul, J. F. O'Hara, W. Cao, I. Al-Naib, and W. Zhang, Limitation in Thin-Film Sensing with Transmission-Mode Terahertz Time-Domain Spectroscopy, Vol. 22, No. 1 Optics Express (2014).
18- J. F. O Hara. W. Withayachumnankul, I. Al-Naib, A Review on Thin-film Sensing with Terahertz Waves, Springer Science (2012).
19- J. S. Melinger, S. Sree Harsha, N. Laman, and D. Grischkowsky, Guided-Wave Terahertz Spectroscopy of Molecular Solids [Invited], J. Opt. Soc. Am. B/Vol. 26, No. 9 (2009).

20- Z. Jiang, M. Li, and X.-C. Zhang, Dielectric Constant Measurement of Thin Films by Differential Time-Domain Spectroscopy, Appl. Phys. Lett. (2000).

21- W. Lai, H. Zhang, Y. Zhu, Q. Wen, A Novel Method to Measure Dielectric Properties of Materials in Terahertz Spectroscopy, Optik (2013).

22- Y-C Shen, Terahertz Pulsed Spectroscopy and Imaging for Pharmaceutical Applications: A review, International Journal of Pharmaceutics (2011).

23- G. Wang, J. Shen, and Y. Jia, Vibrational Spectra of Ketamine Hydrochloride and 3, 4-Methylenedioxymethamphetamine in Terahertz Range, J. Appl. Phys. (2007).

24- T. Lu, Z. Kun, Z. Qing-Li, S. Yu-Lei, Z. Cun-Lin, Quantitative Analysis for Monitoring Formulation of Lubricating Oil Using Terahertz Time-Domain Transmission Spectroscopy, Chin. Phys. Lett (2012).

25- M. Dragoman, D. Dragoman, Review Plasmonics: Applications to Nanoscale Terahertz and Optical Devices, Progress in Quantum Electronics 32 1–41(2008).

26- N. J. de Mol, and M. J. E. Fischer, Surface Plasmon Resonance: A General Introduction, Chapter 1 from Surface Plasmon Resonance: Methods and Protocols, Mol, Nico J. de, Fischer, and Marcel J. E, New York : Humana Press (2010).

27- W. Cao, C. Song, T. E. Lanier, R. Singh, J. F. O'Hara, W. M. Dennis, Y. Zhao and W. Zhang, Tailoring Terahertz Plasmons with Silver Nanorod Arrays, Scientific Reports DOI: 10.1038/srep01766 (2013).

28- J. Saxler, J. G. Rivas, C. Janke, H. P. M. Pellemans, P. H. Bolívar, and H. Kurz, Time-Domain Measurements of Surface Plasmon Polaritons in the Terahertz Frequency Range, Physical Review B 69, 155427 (2004).

29- N. C. J. van der Valk, and P.C. M. Planken, Effect of a Dielectric Coating on Terahertz Surface Plasmon Polaritons on Metal Wires, Appl. Phys. Lett. 87, 071106 (2005).

30- W. Zhang and Abul. K. Azad, Extraordinary Terahertz Transmission of Subwavelength Plasmonic Structures, from Terahertz Physics, Devices, and Systems, edited by M. Anwar, A. J. DeMaria, and M. S. Shur, Proc. of SPIE Vol. 6373, 63730P, (2006).

31- Y Tsuji, M Yanagisawa, H Yoshinaga, and K Hiratsuka, Study of Reactive Ion Etching for Reverse Tone Nanoimprint Process, Journal of Physics: Conference Series 191 (2009).

32- F. Yang, J. R. Sambles, and G. W. Bradberry, Long-Range Surface Modes Supported by Thin Films, Phys. Rev. B 44, 5855 (1991).

References for Tables:

1- X-C Zhang, and J. Xu, Terahertz Radiation Chapter 1 from Introduction to THz Wave Photonic, Springer Science and Business Media, LLC (2010).
2- Zomega Terahertz Corporation, The Terahertz Wave eBook, (2012).
3- J. El Haddad, B. Bousquet, L. Canioni, P.Mounaix, Review in Terahertz Spectral Analysis, Elsevier (2013).
4- J. F. O Hara. W. Withayachumnankul, I. Al-Naib, A Review on Thin-film Sensing with Terahertz Waves, Springer Science (2012).